RADIATION FROM RELATIVISTIC ELECTRON BEAMS IN PERIODIC STRUCTURES

by

Richard Earl Stoner

B.S., University of Washington
(1981)

Submitted to the
DEPARTMENT OF PHYSICS
in Partial Fulfillment of the Requirements
for the Degree of

DOCTOR OF PHILOSOPHY

at the

MASSACHUSETTS INSTITUTE OF TECHNOLOGY

June, 1994

Signature of author _____
Department of Physics
June 15, 1994

Certified by _____
Professor George Bekefi
Thesis Supervisor

Accepted by _____
Professor George F. Koster
Chairman, Departmental Graduate Committee

RADIATION FROM RELATIVISTIC ELECTRON BEAMS IN PERIODIC STRUCTURES

by

Richard Earl Stoner

Submitted to the Department of Physics
on June 10, 1994 in partial fulfillment of the
requirements for the Degree of Doctor of Philosophy in Physics

ABSTRACT

I present an experimental study of emission of radiation from relativistic electrons in novel periodic structures. The first structure is a short-period wiggler magnet for free-electron lasers (FELs). The device is a pulsed ferromagnetic-core electromagnet consisting of 70 periods of 8.8 mm, generating an on-axis peak magnetic field of 4.2 kG. Each field peak is independently tunable. I employed a novel tuning scheme to reduce the RMS spread in the peak amplitudes to 0.12%, the lowest ever attained in a sub-cm-period periodic magnetic field.

A high-brightness, 40 MeV pulsed electron beam produced by the LINAC at the Accelerator Test Facility at Brookhaven National Laboratory was injected into the short-period wiggler, and visible synchrotron emission was produced. Spectral density profiles were measured, and the measured peak wavelength was shown to vary appropriately with electron beam energy. It is shown that the principal spectral broadening mechanisms are longitudinal energy spread and off-axis emission.

The second class of structures consists of blazed conducting gratings, with periods ranging from 1-10 mm. Relativistic electrons at 2.8 MeV were passed over these gratings and produced millimeter and submillimeter emission via the Smith-Purcell effect. I have experimentally demonstrated a spectral peaking effect never before observed: peaks occur at wavelengths at which parallel-propagating grating modes are phase-velocity-matched to electron-produced evanescent waves of that wavelength (a so-called inverse Wood anomaly resonance). The peak wavelengths and linewidths of peak structures from 2-mm period and 4-mm-period gratings were measured, and found to be in very good agreement with theory. These measurements are the most precise test of any theory of Smith-Purcell emission to date, and strongly verify the theory of van den Berg. This spectral peaking effect could prove valuable to the development of a grating-based infrared FEL using relativistic electrons.

Thesis Supervisor: Dr. George Bekefi
Title: Professor of Physics

ACKNOWLEDGEMENTS

I must first acknowledge and thank my thesis advisor, Prof. George Bekefi, for his patient and unflagging support- material, financial, and intellectual- which made this work possible. Many others deserve my gratitude. Chief among them are my Dartmouth College colleagues, Prof. John Walsh and Mr. Ken Woods, both of whom provided great help and support. Just as crucial to the completion of my thesis was the help of CPT James Blastos, whose willingness to carry out difficult tasks under demanding circumstances was singular for the good cheer in which it was offered. David Sisson provided valuable help in the home stretch. Thanks also are due to Shien-chi Chen for his help in the early days of my involvement on the Microwiggler project.

My thanks go to my thesis committee members, Profs. Jonathan Wurtele and Leslie Rosenberg. I must express particular gratitude to Prof. Rosenberg, a formidable editor who contributed significantly to the quality of my thesis.

There are many people at the Accelerator Test Facility to whom I am very thankful. Drs. Rick Fernow and Harold Kirk worked hard all along to aid the the Smith-Purcell experiment. Dr. Xijie Wang was exceedingly helpful in trusting me with valuable equipment indispensable to the carrying out of my duties to both experiments. His enthusiasm for physics was contagious; as a recent Ph.D. recipient himself, he was always willing to lend a sympathetic ear to my various tales of joy and woe. His experimental suggestions were always useful. Dr. Ilan Ben-zvi was exceedingly generous in allocating runtime to my experiments and took an active interest in seeing to it that I could complete my thesis work. Dr. Alan Fisher capably performed the brutal task of tuning the accelerator during the spontaneous emission runs. Bob Malone and Irene Bottke were always willing to help with setting up the VAX control computer, and with any computer-related question. I must not forget to thank Drs. Joe Fisher and Triveni Rao for the extended use of the cryopump on the Smith-Purcell experiment. The technical staff of the ATF was invariably helpful with materials, advice, and the occasional extra pair of hands: thanks to Cyrus Biscardi, Bill Cahill, Rich Freudenberg, Bob Harrington, and Marc Montemagno. Fine fellows all.

Likewise, the members of the Bekefi group at MIT were all invariably friendly and helpful. Ivan Mastovsky provided very valuable assistance, so much so that I have almost forgiven him for being more clever than I in matters of mechanical design. Felicia Brady was a capable administrator, and always entertaining. Palma Catravas, my successor on the Microwiggler project, was impressive for being undaunted by the complexity of the Machine. Alex Matusis and John Doan contributed to the Microwiggler work as well. Thanks also for the comradeship and generously shared physical insight of Manoel Conde, Tony DiRienzo, Pavel Wolfbeyn, Gennady Shvets, Beth Chen, and Wen Hu.

My life would have been vastly poorer without the friendship of the VERSATOR group, members all of the Lost Generation (*i.e.*, the entering class of 1984): the "*J*" Team, *J*oel Villasenor, *J*eff Colborn, and *J*ared Squire. Both Joel and I in turn must express gratitude to the Deity in that neither of us was snuffed out in our ill-fated, jointly-owned ultralight airplane.

Thanks also to the personnel in the Physics graduate office. Prof. George Koster was quite helpful during my exceedingly difficult experience of changing research groups. Peggy Berkovitz was always a pleasure to deal with, and never once spanked me for my seeming inability to cope with registration deadlines.

I would be remiss in failing to mention and thank my fellow students from my Pritchard group days: Warren and Deb Moskowitz (for tolerating the Thing That *Really* Wouldn't Leave- *Ever*), Brian Stewart, Peter Magill, Bruce Oldaker, Michelle Stephens, Peter Martin, Scott Paine, George Welch, Mike Kash, Barbara Hughey-Beckwitt, Chris Ekstrom, David Keith, Ke-Xun Sun (who, like me, did not remain in the Pritchard group- for similar reasons), Bruce Oldaker, Kris Helmerson, Debra Lew, Genevieve Sparagna, Eric Cornell, Kevin Boyce, Vesant Natarajan, Bob Flanagan, Tom Scott, Robert Weisskoff, Vanderlei Bagnato, and Eric Raab. Mike Joffe and Wolfgang Ketterle deserve special mention for having recommended me for a post-doctoral position I ultimately accepted.

There are several other people who don't fit neatly into the above categories who must be mentioned. Steve Smith was remarkably helpful both in discussing physics and in loaning small but crucial pieces of hardware, as well as being a worthy weight-lifting protege. Wendy Calvin and Andrew Trupin have remained good friends since my brief time at University of Colorado, as has Steve Miller.

Finally, profound love and thanks to my family: mother Judy, sisters Sherry, Sandy, and Deedie, brothers Randy and Ron, nephews Damian, Zach, Kasey, Sam, and Seth, and niece Sabrina. I am particularly happy to inform my nephews and niece that their Uncle Ricky actually finished school before they did.

15 June 1994

Dedicated to my mother,

Julia E. Stoner

my family

and to the memories of my father

Merlyn D. Stoner

and my sister

Debra J. Stoner

TABLE OF CONTENTS

TABLE OF FIGURES

CHAPTER 1

INTRODUCTION AND BASIC THEORY

1.1 Introduction

Maxwell theorized in 1865 that electromagnetic radiation is produced by the acceleration of charged matter [Maxwell, 1865]. The relationship between electric currents and electromagnetic waves was first studied by Hertz [Hertz, 1889]. The concept and demonstration of electromagnetic radiation generation from "free" electrons (i.e. electrons not bound to an atomic or ionic nucleus) thus predates that of emission by quantum systems by three decades: it was the subsequent demonstration of the quantized nature of charge [Millikan, 1909] and the nuclear structure of atoms [Rutherford, 1911] that led to the formulation by Bohr of his theory of the hydrogen atom [Bohr, 1913] and its explanation for the quantized nature of light emitted by atoms.

Likewise, technology for coherent microwave radiation generation from free electrons, which surged during World War II with the need for such sources for use in radar applications, preceded the first coherent microwave radiation source based on a quantum transition (the molecular beam maser) [Gordon *et. al.*, 1954; Kleppner *et. al.*, 1962]. However, the development of coherent sub-mm, infrared, visible, and ultraviolet sources did not follow this (classical, quantum) historical order. The explosion of laser technology in the 1960's [Bertoletti] resulted in the overwhelming predominance (both practical and conceptual) of laser sources in generating coherent radiation in these bandwidths, whereas it is only relatively recently that coherent free electron sources in these wavelength ranges have been demonstrated. These sources are known as free electron lasers.

The term "free electron laser" was originally coined by Madey [Madey, 1971] to denote a class of continuously wavelength-tunable devices to generate coherent sub-mm, visible, ultraviolet, and even x-ray radiation from free electrons in a relativistic electron beam. Such a tunable source could provide coherent radiation at wavelengths for which continuously tunable laser sources are unavailable, e.g., the far infrared (FIR, 0.1-1 mm), and the UV and x-ray regimes. His original proposal was offered in terms of a quantum-mechanical scattering process in which virtual photons, from a periodic magnetic field static in the laboratory frame, are scattered from relativistic electrons and which in turn influence other such scattering events to occur in phase-coherence. It has subsequently been shown [Kroll and McMullin, 1978] that free electron lasers (FELs) can be described in terms of a classical mechanism in which the synchrotron emission from the electrons' oscillatory motion in a periodic magnetic field couples to the electrons' axial motion via the periodic field. The axial density profile of the electron beam is perturbed such that the electrons' emission starts to become phase-coherent, resulting in stronger emission, implying stronger density perturbations and thus stronger phase coherence and emission, etc.; a runaway positive feedback is the result. This kind of growth mechanism is the basis for numerous devices operating in the microwave regime, and it is only the transverse periodic magnetic field coupling that is specific to the FEL interaction. In fact, Motz proposed an interaction, described in classical terms, which employed an "undulator" device producing a transverse periodic magnetic field [Motz, 1951; Motz *et. al.*, 1953]. It has subsequently been shown that he was the first to propose a FEL. He asserted that his proposed device could be extended to visible and even x-ray wavelengths, and was able to produce incoherent visible emission with an electron beam. A microwave FEL was later demonstrated by Philips [Philips, 1960], which he termed the ubitron. Madey's proposal was therefore not entirely original, but it revived and energized the idea of generating coherent short-wavelength radiation with free electrons.

Within a few years of Madey's proposal, he demonstrated a free-electron laser oscillator operating at a wavelength of 3.4 μm [Deacon *et. al.* 1977]. The shortage of tunable sources in the FIR and UV has driven enormous subsequent research activity, both theoretical and experimental, far more than can be referred to here even tangentially. Devices operating at near-IR, visible and UV wavelengths have been demonstrated [Benson and Madey, 1989; Billardon *et. al.*, 1983; Couprie *et. al.*, 1993; Edighoffer *et. al.*, 1984; Hama *et. al.*, 1994; Slater *et. al.*, 1986], but they rely on the use of a large (several hundred MeV) LINAC or storage ring for electron beam production and a very large and expensive wiggler (or undulator) magnet to produce the transverse periodic magnetic field required for the FEL interaction. There is continuing research to reduce the size and expense of the facilities and equipment needed to operate FELs, to render them a cheaper and thus more practical radiation source [Batchelor *et. al.*, 1988; Nguyen *et. al.*, 1994; O'Shea *et. al.*, 1994; Zhang *et. al.*, 1994]. I have addressed this scale reduction problem via the design, construction, and operation of a short-period microwiggler magnet. It is shown in Section 1.2 that the wavelength produced by a FEL is directly proportional to the wiggler period and inversely proportional to the square of the electron beam energy. Thus, a microwiggler permits the production of a given wavelength using an electron beam of reduced energy. It is the reduction in beam energy and the corresponding size and cost reduction in the accelerator that leads to the majority of the savings, though some cost advantage is realized by the wiggler size reduction itself.

A critical figure of merit for wiggler performance is the wiggler parameter a_w, defined by

$$a_w = \frac{eB_w\lambda_w}{2\pi m_e c^2} \tag{1.1}$$

which will be shown in the next section to be the normalized electron wiggle velocity: B_w is the peak on-axis wiggler magnetic field magnitude, λ_w is the wiggler period, and m_e is the electron mass. The small-signal FEL gain and efficiency (see Sec. 1.2.5) are strongly increasing functions of a_w [Kroll and McMullin, 1978], so that as λ_w is reduced, B_w must be made as large as possible in order to preserve FEL performance (the dependence of FEL gain on a_w is discussed in Sec. 1.2.5). To do so while maintaining a large enough aperture to pass a useful electron beam is difficult; moreover, errors in both the field amplitude and periodicity must be kept to a minimum, so that the electron beam is not steered or displaced out of the radiation beam and so the relative phase of the electron wiggle motion and the radiation mode is not unduly disrupted. To that end, I have constructed a highly tunable microwiggler magnet producing the world's most precise periodic magnetic field with <10 mm period. Chapter 2 of this work describes the design of the MIT Microwiggler, and reviews current activity in short-period wiggler development. Chapter 3 presents the novel tuning and field measurement scheme leading to an RMS spread in the peak on-axis wiggler amplitudes of 0.12%, the best of which I am aware in a sub-cm period device.

Chapter 4 presents preliminary studies of incoherent emission from the MIT Microwiggler. Incoherent emission spectra can serve as a fast, non-destructive probe of electron beam parameters relevant to FEL performance, such as beam emittance, energy spread, momentum dispersion, etc. The incoherent emission spectrum diagnostic for the electron beam will ultimately be employed in developing a microwiggler-based UV FEL on the 50 MeV LINAC at the Accelerator Test Facility (ATF), Brookhaven National Laboratory [Batchelor et. al, 1988]. I demonstrate that the principal spectral broadening mechanisms acting in the incoherent emission spectra from the MIT Microwiggler are longitudinal energy spread and off-wiggler-axis electron emission. The emission spectra, acquired in collaboration with ATF personnel, also show that the measured mean

wavelength agrees with theoretical predictions. These studies also demonstrate that an electron beam can indeed propagate though the wiggler without undue beam steering or displacement. Chapter 4 also discusses further use of incoherent emission spectra as an electron beam diagnostic.

Periodic structures other than wiggler magnets can be employed as a basis for radiation generation from free electrons. In particular, electrons passing at grazing incidence above a conducting grating will induce emission via the Smith-Purcell effect [Smith and Purcell, 1952]. The emission results from oscillating surface currents induced in the grating by the passing electrons, and the radiation is dispersed by the grating such that a given wavelength is emitted at a specific set of angles in a fashion analogous to grating diffraction. The original experiment of Smith and Purcell was carried out at visible wavelengths using nonrelativistic electrons, as has been a considerable body of subsequent work [Bachheimer and Bret, 1968; Bachheimer, 1972; Burdette and Hughes, 1976; Gover and Livni, 1978; Gover *et. al.*, 1984; Shih *et. al.*, 1990]. In contrast, John Walsh of Dartmouth College and collaborators [Doucas *et. al.*, 1992] demonstrated that relativistic electrons (3.6 MeV) passed over mm-period gratings produce strong emission at FIR wavelengths. They showed that Smith-Purcell emission is a potential FIR source to compete with synchrotron sources.

I have extended the work of Doucas *et. al.* by performing a precision spectroscopy study of the Smith-Purcell effect. Investigating the physics of the Smith-Purcell effect was greatly facilitated, as compared to visible-wavelength experiments, by the use of relativistic electrons and mm-period gratings. First, the use of long period gratings permitted precise control over the grating geometry, to tolerances of a few percent of the grating period; these tolerances greatly exceeded those of the gratings used in previous work at visible wavelength, since those grating periods were of micron scale. Precise

knowledge of the grating geometry is required to test a detailed theory of the Smith-Purcell effect. Second, producing Smith-Purcell emission in the FIR and mm-wavelengths circumvented interference from competing visible-light emission processes (*e.g.*, electron impact excitation and transition radiation: Bachheimer, 1972) encountered by previous workers studying visible Smith-Purcell emission. Such spurious visible emission was (probably) also produced in this work, but it could not be sensed by the FIR detector. Finally, using relativistic electrons to produce FIR and mm-wavelength emission greatly extended the distance above the grating at which electrons can pass while still producing significant emission. The strength of emission produced by an electron decreases exponentially with distance above the grating. The ($1/e$) length of this exponential variation is proportional to the electron's energy and the emission wavelength (Appendix 1, eqn. A1.8). The high-brightness electron beam of the ATF can be focused and controlled with precision greater than the ($1/e$) length of our emission, in sharp contrast with that of visible-emission investigators, where the ($1/e$) coupling distance was much less than a micron. Thus, in my work I was able to specifically account for the electron beam geometry in comparing emission spectra to theory.

The combination of the above factors has enabled me to carry out the most precisely controlled investigation to date of the Smith-Purcell effect. In collaboration with Walsh and other Dartmouth personnel, and ATF personnel, I have observed and precisely characterized a spectral peaking effect first predicted by Hessel [Hessel, 1964]. This effect has never before been observed. The peaks result from what can be termed an "inverse Wood anomaly" [Wood, 1935]. A Wood anomaly is a diffraction grating effect wherein light incident upon a grating is diffracted into a bound surface mode, *i.e.*, a mode propagating parallel to the grating surface. This process is time-reversible, so that if the bound grating mode were excited, strong emission from the grating would result. The Smith-Purcell effect can be described as grating diffraction of evanescent waves produced

by the moving electron [Toraldo di Francia, 1960]; certain of such waves can excite a bound grating mode to produce a time-reversed Wood anomaly. These peak wavelengths are good candidates for operating points of a FEL based on the Smith-Purcell effect.

Chapter 5 presents a brief survey of earlier experiments on the Smith-Purcell effect, and description of the experimental apparatus and measurement techniques. The spectral peak results are given in Chapter 6. Chapter 6 also discusses recommended future work. Finally, Chapter 7 presents concluding remarks.

1.2 Basic Theory

In this section I present the physical concepts needed to understand the experiments in this work, with an eye towards illustrating the fundamental similarities between grating and wiggler-based emission. I begin with a derivation of the emission wavelength, as a function of electron beam energy and emission angle, for electrons traversing a periodic structure. I then derive the general form for a periodic magnetic field, and then relate that form to a planar wiggler geometry; the radiative coupling of electrons to a conducting grating will then be shown to be fundamentally similar to the wiggler field structure. An approximate analysis of electron motion in a planar wiggler field is then presented. I then derive a relation giving the total power and the spectral density of emission from an electron traversing a periodic magnetic field, and then offer a simple scaling law for Smith-Purcell emission power. A review of the theory of Smith-Purcell emission wavelength spectral distributions [van den Berg, 1973] is presented in Appendix 1. Finally, I present a brief summary of FEL theory as it relates to small-signal gain in various parameter regimes, in order to better connect this work with the ultimate goal of the MIT Microwiggler project: a visible-wavelength FEL oscillator.

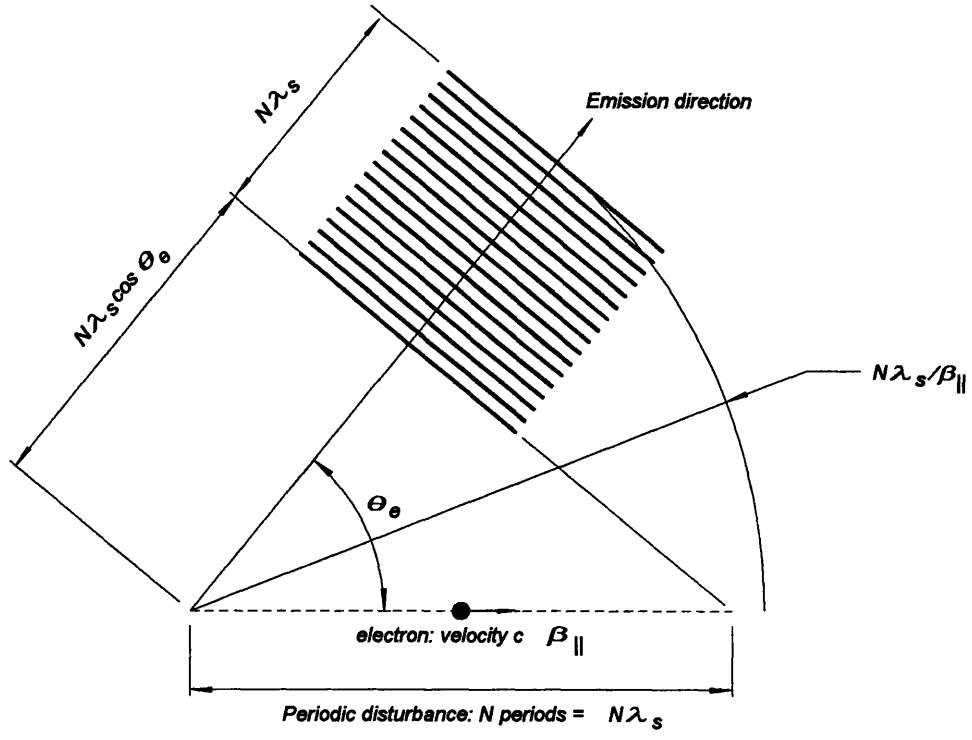

Periodic disturbance:

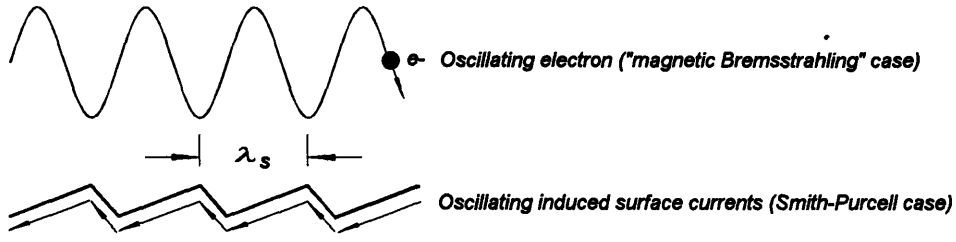

FIGURE 1-1. Wavelength of emission from an electron in a periodic structure.

1.2.1 Wavelength of emission from an electron in a periodic structure

I now derive the expression for the fundamental wavelength of emission of radiation from electrons in a periodic structure. This expression is derived in any number of references on free electron sources of radiation [Marshall, p.23; Brau, p. 11].

Figure 1-1 illustrates an electron inducing a periodic electromagnetic disturbance with period λ_s in the laboratory frame. In the case of a grating structure, the disturbance is an oscillating induced current on the grating surface; in the wiggler case, it is an oscillating current due to the electron's transverse wiggle motion*. In both cases, the oscillation is in the vertical plane: such oscillatory motion leads to vertically polarized radiation. There are N periods assumed to be in the structure, and thus there are N periods in the emitted radiation pulse. The total length of the emitted pulse varies with direction, however, since Doppler wavefront compression occurs in varying degrees: in the forward direction, the electron very nearly keeps up with the radiation wavefront, whereas in the direction perpendicular to the electron's velocity the electron moves parallel to the radiation wavefront. The total pulse length L is just the total distance d_{rad} travelled by the leading edge of the radiation pulse during the interaction, minus the distance d_e normal to the wavefront traversed by the electron:

$$L = d_{rad} - d_e = \frac{N\lambda_s}{\beta_\parallel} - N\lambda_s \cos(\theta_e) \tag{1.2}$$

where $\beta_\parallel c$ is the longitudinal component of the electron velocity, and θ_e is the angle of the emission axis from the axis of the electron beam propagation. The emission wavelength $\lambda(\theta_e)$ is just L divided by the number of periods N: then

$$\lambda(\theta_e) = \lambda_s(\frac{1}{\beta_\parallel} - \cos\theta_e). \tag{1.3}$$

It should be immediately noted that this argument does not account for shorter-wavelength harmonics beyond the fundamental wavelength of (1.3). Such harmonics are

* The radiation resulting from the magnetically-induced wiggling is sometimes called "magnetic Bremsstrahling". Non-experts in beam radiation physics should be aware, however, that this term is by no means universally accepted. Its use is convenient here.

present in both grating- and wiggler-induced emission, due to the presence of harmonics in the current density beyond the fundamental. In the discussion below, however, I will make explicit note of these harmonics only in the grating emission case, since the experiments of this work entail observations of higher-harmonic grating emission, but not of wiggler emission. I emphasize that higher-harmonic wiggler emission plays an important role in other experimental settings, so that omission of its further mention shouldn't be taken as dismissive of its importance.

In the case of Smith-Purcell radiation, two comments should be made. First, there is essentially no perpendicular electron velocity induced by the interaction, it is the oscillating induced surface currents in the grating that radiate (of course, the electron has to give up some kinetic energy for radiation to be emitted, but the fractional energy loss is small): thus, $\beta_{\parallel} = \beta$. Second, the grating disperses significant emission over all angles. A specific wavelength-angle relation for the Smith-Purcell effect, including harmonics beyond the fundamental, can thus be stated as

$$\lambda_{S-P}(\theta_e) = \frac{\lambda_G}{n}\left(\frac{1}{\beta} - \cos\theta_e\right) \tag{1.4}$$

where λ_G is the grating period, $n = 1,2,...$ is the emission order number, and $\beta \cdot c$ is the electron velocity. Significant emission over all emission angles was indeed observed at the energy/wavelength regime in which my experimental work was conducted (2.8 MeV, 0.6-7 mm), though at very high energies the emission is predicted to be peaked in the forward direction [Walsh *et. al.*, 1994].

Equation (1.3) can be expressed in terms of the electron relativistic factor $\gamma = (1-\beta^2)^{-1/2}$ in simple form when $\gamma >> 1$, as is the case with the electron/wiggler emission presented in this work. In so doing attention must be given to the fact that $\beta \neq \beta_{\parallel}$

for electron motion in a wiggler magnetic field: it will be shown later in this section that they are related by

$$\beta_{\|}^2 = \beta^2 - \frac{a_w^{\,2}}{\gamma^2}, \tag{1.5}$$

from which it follows that

$$\lambda_{M-B} = \lambda_w \frac{1}{2\gamma^2}\left(1 + \frac{a_w^{\,2}}{2} + \gamma^2\theta^2\right) \tag{1.6}$$

where λ_w is the wiggler period; we have also used a small-angle approximation for the cosine term of (1.3) (the "M-B" subscript denotes "magnetic Bremsstrahling", a term for wiggler-induced radiation coined by Gover [Friedman *et. al.*, 1988]). The small-angle approximation is applicable over the range of angles into which significant emission occurs: it is well-known that, when $\gamma >> 1$, Bremsstrahlung emission from relativistic particles is strongly peaked in a forward cone whose half-angle is of order $1/\gamma$ [Jackson, p. 665]. It has already been mentioned that, as in the Smith-Purcell emission, there are higher harmonics emitted from the electron-wiggler interaction. Wiggler emission harmonics arise from two contributions: electron coupling to higher spatial-frequency wiggler field harmonics, and additional electron axial "jiggle" motion due to electron wiggle motion coupling to the wiggler field. Insofar as the measurements presented in Chapter 4 (and indeed, any of our foreseeable future measurements) include only the fundamental emission component, further discussion of harmonic structure is superfluous here.

1.2.2 Structure of a wiggler magnetic field and its relation to electron-grating coupling

A wiggler magnetic field is periodic with field lines perpendicular to the axis of periodicity, as illustrated in Fig. 1-2. An "ideal" field would be described mathematically by the relation (according to the coordinate system of Fig. 1-2: note that $k_w \equiv \frac{2\pi}{\lambda_w}$)

$$\vec{B}_w(z) = B_o \hat{e}_2 \cos(k_w z); \tag{1.7}$$

such a field would be free of undesireable transverse y-plane focussing and x-plane steering and deflection. Regrettably, such a field is forbidden in principle by Maxwell's equations as well as in practice by unavoidable mechanical imperfections in the device to produce it. An expression for a physically realizable field can be obtained by solving the Maxwell equations for a static magnetic field in free space, which lead immediately to a Laplace equation

$$\nabla^2 \vec{B} = 0. \tag{1.8}$$

It can be easily shown that this equation is solved by a field of the form

$$\vec{B} = \hat{e}_2 \sum_{n=1}^{\infty} B_n \cos(nk_w z)\cosh(nk_w y) - \hat{e}_3 \sum_{n=1}^{\infty} B_n \sin(nk_w z)\sinh(nk_w y) \tag{1.9}$$

where mathematically allowed field contributions like a focussing field or an axial guide field have not been included; also, we are considering a volume of symmetric finite extent in the y-direction but infinite in x and z. This is a completely general relation; however, computing the coefficients B_n can be non-trivial when magnetically permeable materials are present in the wiggler. We note that the field due to one side of the wiggler structure (the lower half, say, for definiteness) is given by

$$\vec{B} = \hat{e}_2 \sum_{n=1}^{\infty} \tfrac{1}{2} B_n e^{-nk_w y} \cos(nk_w z) + \hat{e}_3 \sum_{n=1}^{\infty} \tfrac{1}{2} B_n \sin(nk_w z) e^{-nk_w y}; \qquad (1.10)$$

the field strength is seen to fall off exponentially as one moves away from the structure half, just as do the periodic components of the electric field due to a charged rectangular grid [Feynman, v. II, p. 7-10]. An electron interacting with the n^{th} harmonic of the field due to the structure half thus experiences accelerations scaling with height (y) above the structure as $e^{-nk_w y}$; thus, the radiated power from the electron scales with y as $e^{-2nk_w y}$. This result parallels the exponential scaling of Smith-Purcell emission remarked upon earlier.

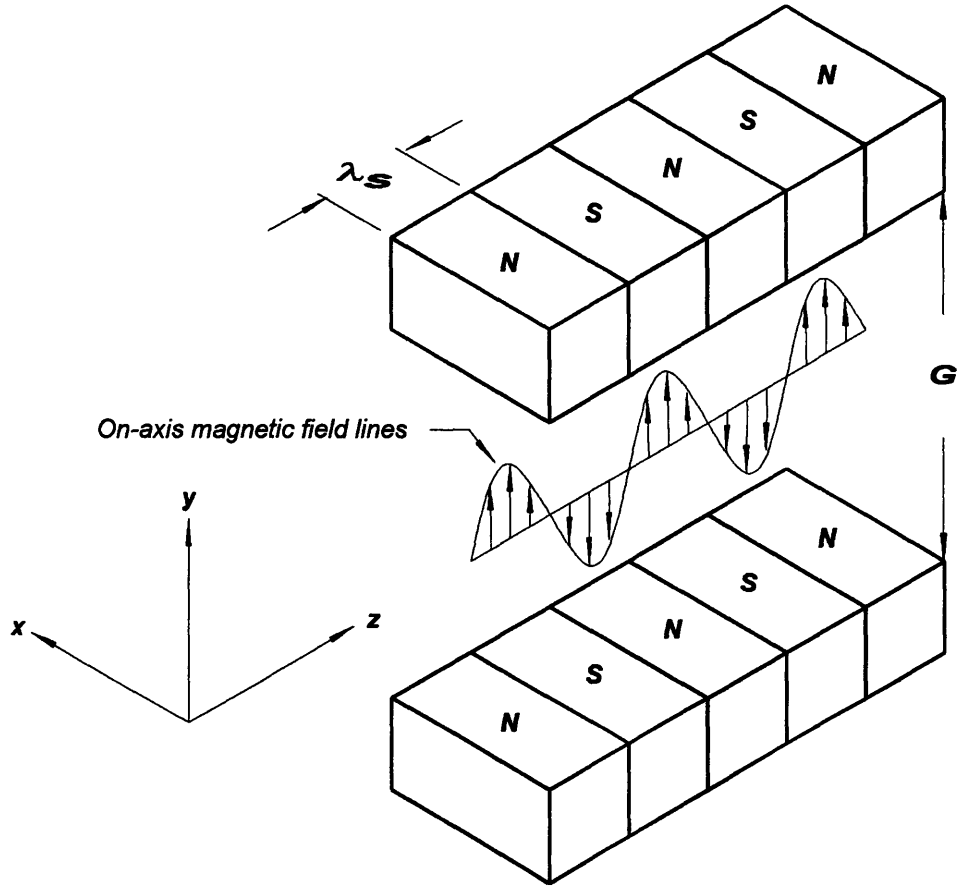

FIGURE 1-2. Wiggler field in relation to its generating structure. The gap-to-period ratio depicted is much larger than in an actual wiggler.

1.2.3 Electron motion in a wiggler magnetic field

This section presents a simple description of electron motion in a wiggler magnetic field, including the identification of a_w (Eqn. (1.1)) as the normalized electron wiggle velocity. I consider only the fundamental wiggler field harmonic (*c.f.*, Eqn. (1.9)), and I consider transverse (y) field variations only to first order in $k_w y$. It is also assumed that the electron motion is predominantly translational motion in the z direction at a speed nearly that of light. A more formal derivation is performed by Brau [Brau p. 66].

In the absence of an electric field, the Lorentz force law in the laboratory frame is given by

$$\vec{F} = \frac{(-e)}{c}\vec{v} \times \vec{B} \tag{1.11}$$

for an electron of charge $(-e)$ and velocity $\vec{v}$. Let $\vec{B}$ be the $(n = 1)$ harmonic of the field given in Eqn. (1.9). The equations of motion are obtained via the application of $\vec{F} = d\vec{p}/dt$, and the fact that a magnetic field can perform no work on the electron (of course, the electron can give up energy to the radiation field). They are

$$\begin{aligned}
\vec{B} &\cong \hat{e}_2 B_w \cos(k_w z) - \hat{e}_3 B_w \sin(k_w z) \cdot (k_w y) \\
\dot{v}_1 &= \frac{e}{\gamma m_e c}\left(v_3 B_2 - v_2 B_3\right) \\
\dot{v}_2 &= \frac{e}{\gamma m_e c} v_1 B_3 \\
\dot{v}_3 &= -\frac{e}{\gamma m_e c} v_1 B_2
\end{aligned} \tag{1.12}$$

where (1, 2, 3) subscripts denote (x, y, z) components, respectively, and $\gamma = (1-\beta^2)^{-1/2}$ is the electron relativistic factor. These equations have no analytic solution valid to all orders

of (a_w / γ) and $k_w y$, and must be numerically integrated to obtain exact solutions. For an approximate solution, first take

$$\dot{v}_1 \cong \frac{eB_w}{\gamma mc} v_\parallel \cos(k_w v_\parallel t) \tag{1.13}$$

in which we initially assume that $z(t) \cong v_\parallel t$, and drop terms of second order in $k_w y$. We have also defined the amplitude of the first field harmonic $B_1 \equiv B_w$. This equation can be easily integrated if we assume that the time variation of y is negligible in comparison to that of the cosine term, yielding

$$v_1(t) \cong \frac{a_w c}{\gamma} \sin(k_w v_\parallel t) + v_{1,0}, \tag{1.14}$$

where a_w is the wiggler parameter defined by Eqn (1.1). The electron executes a "wiggle" motion in the plane perpendicular to the transverse (y-) field component, as well as a possible uniform motion in that plane. The x-position can be obtained through a simple integration. The relation for $\dot{v}_2$ in Eqn. (1.12) can be written in terms of (1.14) as

$$\begin{aligned} \dot{v}_2 \cong \frac{ea_w}{\gamma^2 m_e c^2} \sin(k_w v_\parallel t) \cdot B_1 &= \frac{ea_w}{\gamma^2 m_e c^2} \sin(k_w v_\parallel t) \cdot \left(-B_w \sin(k_w v_1 t) \cdot (k_w y)\right) \\ &= -\left(\frac{a_w k_w c}{\gamma}\right)^2 \sin^2(k_w v_\parallel t)(k_w y) \\ &= -\left(\frac{a_w k_w c}{\gamma}\right)^2 \left(\frac{1+\cos(2k_w v_1 t)}{2}\right)(k_w y) \end{aligned} \tag{1.15}$$

If we neglect the rapidly varying cosine factor, we can write a harmonic oscillator equation for the transverse electron motion which describes the average y-position of the electron:

$$\ddot{y} = -\left(\frac{a_w k_w c}{\sqrt{2}\gamma}\right)^2 y \equiv -\omega_\beta{}^2 y \tag{1.16}$$

This describes what is referred to as betatron motion, and ω_β is called the betatron frequency. The wiggle motion couples to the axial field component to produce a transverse focussing force. The betatron velocity is of first order in (a_w/γ), so that for large γ the assumption that $v_3 B_2 >> v_2 B_3$ (made in solving for v_1) is valid, since v_3 contains a term of order zero in (a_w/γ), and B_2 and B_3 are of similar magnitude.

Finally, the relation (1.12) for v_3 can be integrated to yield

$$\begin{aligned} \dot{v}_3 &= -\frac{e}{\gamma m_e c} v_1 B_2 \cong -\left(\frac{a_w c}{\gamma}\right)^2 k_w \cos(k_w v_\parallel t) \\ \Rightarrow \quad v_3 &= v_\parallel - \left(\frac{a_w c}{\gamma}\right)^2 \frac{\sin(k_w v_\parallel t)}{v_\parallel} \end{aligned} \tag{1.17}$$

from which we see that $z(t) \cong v_\parallel t$ is also a good assumption, insofar as the additional term of (1.17) is second order in (a_w/γ), and $v_\parallel$ is very close to c. The solutions obtained are thus consistent with the initial assumptions.

Finally, neglecting the small oscillating part of v_3, we relate the total electron speed v to $v_\parallel$ by insisting that the RMS wiggle velocity and the axial speed add in quadrature to yield

$$v^2 = v_\parallel{}^2 + \frac{a_w{}^2 c^2}{2\gamma^2} \tag{1.18}$$

which is the equivalent of eqn. (1.5).

1.2.4 Emission scaling laws for a single electron in a periodic structure

In this section, I derive scaling laws for emission power of an electron in a periodic structure, with a minimum of formalism. In the case of wiggler-induced emission, it is also easy to formulate the spectral power distribution. Jackson presents a general integral relationship which gives the energy emitted per unit solid angle per unit frequency interval by a charged particle undergoing an acceleration [Jackson, p. 671]:

$$\frac{d^2I}{d\omega\, d\Omega} = \frac{e^2\omega^2}{4\pi^2 c}\left|\int_{-\infty}^{\infty} dt\ \vec{n}\times(\vec{n}\times\vec{v})e^{i(\omega t-(\frac{\omega}{c})\vec{n}\cdot\vec{r})}\right|^2, \qquad (1.19)$$

where $\vec{n}$ defines the emission direction, $\vec{r}(t)$ is the particle's position, and $\vec{v}(t)$ is the particle's velocity. An approximate spectral power density expression (having correct scaling with electron energy, wiggler period, and wiggler field strength) for emission of an electron traversing a wiggler magnetic field can be obtained from this integral expression, by substituting for $\vec{v}$ and $\vec{r}$ the results from the previous section, and expressing the integral in terms of dimensionless quantities. Defining

$$\tau \equiv \frac{t}{\left(\frac{N_w\lambda_w}{\beta c}\right)}, \qquad \vec{u} \equiv \frac{\vec{v}}{\left(\frac{a_w c}{\gamma}\right)}, \qquad \vec{\rho} \equiv \frac{\vec{r}}{N_w\lambda_w} \qquad (1.20)$$

in terms of which the intensity distribution function becomes

$$\frac{d^2I}{d\omega\, d\Omega} = \frac{e^2\omega^2}{4\pi^2 c}\left(\frac{N_w\lambda_w a_w}{\gamma}\right)^2\left|\int_0^1 d\tau\ \vec{n}\times(\vec{n}\times\vec{u})\exp(i\omega\frac{N_w\lambda_w}{c}(\frac{\tau}{\beta}-\vec{n}\cdot\vec{\rho}))\right|^2, \qquad (1.21)$$

where the integration is performed over the range in which the particle's acceleration is non-zero. There are two observations to be made regarding (1.21). First, the vector direction of the integral is oriented in the polarization direction of the emission: since the wiggle velocity is in the x-direction, $(\vec{n}\times(\vec{n}\times\vec{u}))$ (and therefore the polarization) is oriented parallel to the x-axis for forward emission. Second, the extraction of dimensional quantities from the integral illustrates the dependence of the intensity on wiggler and electron parameters.

Let us analyze further the simple case of forward-direction emission $\vec{n}=\hat{e}_3$. We neglect the oscillating term in the z-component of the velocity $\vec{v}\cong\hat{e}_3\cdot\beta_\parallel ct+\hat{e}_1\cdot(a_w c/\gamma)\cos(k_w\beta_\parallel ct)$*. The intensity distribution function in the forward direction is thus

$$\left.\frac{d^2I}{d\omega\,d\Omega}\right]_{forward}\cong\frac{e^2\omega^2}{4\pi^2c}\left(\frac{N_w\lambda_w a_w}{\gamma}\right)^2\left|\int_0^1 d\tau\ \cos(2\pi N_w\tau)\exp\left(i\omega\frac{N_w\lambda_w}{c}\tau\left(\frac{1}{\beta}-1\right)\right)\right|^2 \qquad (1.22)$$

By expressing the $\cos(2\pi N_w\tau)$ term in the integrand as a sum of complex exponentials, neglecting the resulting $\exp(+2\pi i N_w\tau)$-proportional term, and defining $\omega_{M-B}\equiv 2\pi c/\lambda_{M-B}$ (see eqn. (1.6)), the integral can be rewritten to yield

$$\begin{aligned}\left.\frac{d^2I}{d\omega\,d\Omega}\right]_{forward}&\cong\frac{e^2\omega^2}{4\pi^2c}\left(\frac{N_w\lambda_w a_w}{\gamma}\right)^2\left|\int_0^1 d\tau\ \frac{1}{2}\exp\left(\frac{2\pi i N_w}{\omega_{M-B}}(\omega-\omega_{M-B})\tau\right)\right|^2\\&=\frac{e^2\omega^2}{16\pi^2c}\left(\frac{N_w\lambda_w a_w}{\gamma}\right)^2\left(\frac{\sin\left(\frac{\pi N_w}{\omega_{M-B}}(\omega-\omega_{M-B})\right)}{\frac{\pi N_w}{\omega_{M-B}}(\omega-\omega_{M-B})}\right)^2\end{aligned} \qquad (1.23)$$

* Keeping the axial oscillation term results in emission harmonics beyond the fundamental.

This relationship captures the scaling with system parameters of the forward emission, as well as the form of the frequency distribution. This result agrees with a more rigorous calculation [Brau, p.72]. The distribution is peaked at the frequency calculated earlier from geometric considerations in Sec. 1.2.1. Observe that the (sin x / x) frequency distribution is identical to that obtained as the squared magnitude of the Fourier transform of the electric field given by

$$E(t) = E_o \sin(\omega_{M-B} t), \quad 0 \le t \le \frac{N\lambda_{M-B}}{c} \qquad (1.24)$$
$$= 0 \quad \text{otherwise.}$$

This is just a pulse of radiation of length $N_w \lambda_{M-B}$. Thus, the frequency distribution can be viewed as due to Fourier transform broadening associated with a pulse of finite duration.

It will be useful in analyzing the data of Chapter 4 to estimate from (1.23) the total emission power over all frequencies and solid angles of a beam of electrons of current I. The single-particle expression can be used for this purpose by assuming that the emissions from the various electrons are randomly phased, so that the total power is obtained by summing the emission power of the individual electrons. Thus, the single-electron expression is integrated over all frequencies, and (since most of the energy is emitted into a cone of angle $(1/\gamma)$) multiplied by a solid angle factor of (π/γ^2), and multiplied by the number of electrons per second contained in the beam: the resulting emission power is

$$P_{M-B} = \frac{a_w{}^2 N_w \gamma^2 I}{\lambda_w} \cdot (1.81 \times 10^{-6} \frac{cm \cdot W}{ampere}) \qquad (1.25)$$

A simple qualitative argument can be made in the case of Smith-Purcell emission to see how emission power scales with grating period for geometrically similar gratings of different periods, given that the electron height above the grating is a fixed number of

grating periods, and that the electron energy is fixed. The argument presented here is more a mnemonic device than a derivation; a rigorous argument is presented in Appendix 1. Assume that the emission power has the same scaling as that of a non-relativistic dipole in which the dipole moment $\vec{p}$ is proportional to the groove depth: since the groove depth is assumed proportional to the grating period, we say that $|\vec{p}|^2 \propto \lambda_G{}^2$. Also, we already know from eqn. (1.4) that the emission frequency ω is inversely proportional to λ_G; then, by substituting into the expression for the emission power of a non-relativistic dipole oscillating at frequency ω [Jackson, p.396], we obtain

$$P_{S-P} \propto |\vec{p}|^2 \omega^4 \propto 1/\lambda_g{}^2. \tag{1.26}$$

This scaling law for geometrically similar gratings can be derived rigorously from the van den Berg theory (see Sec. A2.2).

1.2.5 Small-signal FEL gain: the critical importance of a_w

For readers acquainted with FEL physics, it is clear that studies of incoherent emission are not a sufficient inducement for constructing a wiggler of the type described in this work. The effort associated with the design and construction was immense; incoherent emission studies, even with the laudable goal of electron beam diagnostic development, cannot offer sufficient scientific payoff in exchange for that effort. However, my goal at the outset of the Microwiggler project was that it provide a basis for a visible (and ultimately a UV) FEL oscillator: no such oscillator based on a short-period wiggler currently exists, and the operation of one would comprise a huge advance. That remains the goal of the project and my successors. Something must be said here, therefore, about the FEL interaction, even though FEL physics is beyond the scope of the experiments presented in this work.

There are many reviews of FEL theory: I follow those of [Roberson and Sprangle, 1989], and [Bonifacio *et. al.*, 1990]. As earlier mentioned, the FEL interaction in the small-signal regime is a runaway positive-feedback mechanism in which electron beam density perturbations lead to enhanced coherence in the emission of the component electrons. The enhanced coherence results in increased emission. The radiation is co-propagating with the electron beam, and the electric field of the radiation acts to perturb the electron beam density...leading to increased density perturbations and increased emission, etc. Thus, gain is a collective phenomenon wherein electrons "communicate" via the electromagnetic radiation field*. Figure 1-3 illustrates this self-consistent scheme. As remarked, both the dynamics of the electron motion and of the radiation field are included, as well as the couplings between them.

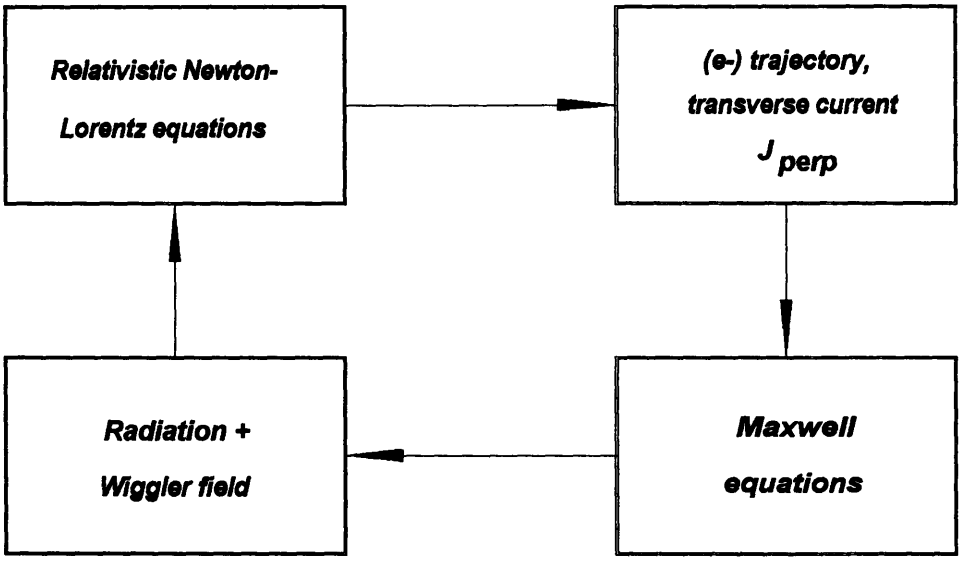

FIGURE 1-3. Classical FEL theory: the self-consistent scheme (from [Bonifacio *et. al.*, 1990].

* When the beam density is very high, the coulombic mutual repulsion of the electrons (space-charge forces) also plays a role.

Applying the analysis scheme to a one-dimensional system comprised of a perfect wiggler field of amplitude B_w and period λ_w (oriented according to the coordinate system of Fig. 1-2), a monoenergetic electron beam of relativistic factor γ and laboratory charge density $(-en_o)$, propagating in the z-direction, and a monochromatic electromagnetic wave of angular frequency ω, also propagating in the z-direction, one obtains equations of motion for the radiation field and the electrons and formulates their coupling. These equations can be linearized to obtain a small-signal dispersion relation for the radiation field [Roberson and Sprangle, 1989]. The dispersion relation is valid when the gain derived from it is large enough that transient terms associated with initial values of the beam density perturbation and the radiation field can be neglected.

The dispersion relation yields an exponential growth factor Γ, in terms of which the radiation field's *amplitude* as a function of z is given by $\exp(\Gamma z)$. There are two high-gain regimes described by the dispersion relation: the high-gain Compton regime, in which forces on the beam due to the combined wiggler/EM wave fields dominate the forces due to space-charge; and the Raman regime, in which beam space-charge waves play a significant role in the interaction. It is here that the critical importance of a_w is manifest; the value of a_w determines which regime into which a given FEL lies. Moreover, the exponential growth factor in each regime depends very strongly on a_w.

Define the critical normalized velocity parameter

$$\beta_{crit} \equiv F^{-1/2}\left(\frac{2\omega_b c^2}{\beta_\parallel^3 \gamma^{1/2} \gamma_\parallel^3 k_w}\right)^{1/2}. \tag{1.26}$$

F is a so-called fill factor, introduced to account for possibly incomplete overlap of the electron beam and the radiation mode, and is defined as the ratio of the beam cross-sectional area to the radiation mode cross-sectional area. ω_b is the beam plasma

frequency, defined as $\left(4\pi n_o e^2/m_e\right)^{1/2}$; and $\gamma_{\|} \equiv \left(1-\beta_{\|}^2\right)^{-1/2}$. The critical normalized velocity parameter discriminates between the two high-gain regimes:

$$\frac{a_w}{\gamma} >> \beta_{crit} \Rightarrow \text{High - gain Compton regime}$$

$$\frac{a_w}{\gamma} << \beta_{crit} \Rightarrow \text{Raman regime}$$

The exponential growth factors associated with the two regimes are given by

$$\Gamma_{Compton} = \frac{\sqrt{3}}{2\gamma} F^{1/3} \left(\frac{a_w^{\,2}}{4} \frac{\omega_b^{\,2} k_w}{c^2} \right)^{1/3}$$

$$\Gamma_{Raman} = F^{1/2} \frac{a_w}{\gamma} \left(\frac{1}{4} \frac{\omega_b \gamma_z k_w}{4c\sqrt{\gamma}} \right)^{1/2} \qquad (1.27)$$

A free electron laser based on the Microwiggler and the ATF LINAC can easily be shown to be a Compton-regime device (see Ch. 4, Sec. 4.2). The dependence of the exponential growth factor is thus $\Gamma_{Compton} \propto a_w^{\,2/3}$. Thus, a_w is indeed a critical parameter in a Microwiggler-based FEL at the ATF (or indeed any high-gain FEL- the dependence on a_w of a Raman regime device is even stronger than the Compton dependence).

CHAPTER 2

A DESIGN FOR PLANAR ELECTROMAGNET MICROWIGGLERS FOR FREE ELECTRON LASERS

2.1 Introduction

Size and cost reduction of visible and UV wavelength FEL systems is necessary if they are to become practical radiation sources. The use of a short-period (1-10 mm) microwiggler magnet permits higher frequency radiation to be generated with a device which is more compact than one employing wigglers of usual length (typically 3-10 cm). This chapter presents a novel design for a pulsed, planar electromagnet microwiggler for free electron lasers. The analytical and computational basis of the design is presented, as well as some experimental results from a four-period prototype. I show that microwigglers generating fields of large magnitude and high precision can be constructed at very modest cost. The design described in this chapter is the basis for a 70-period microwiggler generating the world's most precise periodic magnetic field of sub-cm period.

Microwiggler design and construction pose very serious engineering challenges. Mechanical tolerances of a given value become increasingly large in the fractional sense as the size scale is reduced, leading to correspondingly increased fractional field errors. Also, Eqn. (1.10) shows that the wiggler field strength falls off exponentially as the ratio of the separation between wiggler halves to the wiggler period. Therefore, maintaining a gap adequate to pass an electron beam (a few mm) while reducing the wiggler period results in significant field magnitude attenuation unless corrective measures are taken. In spite of these difficulties, numerous groups have investigated short-period wigglers. A variety of techniques have been proposed and studied- samarium-cobalt permanent magnet grooved slabs [Kimel and Elias, 1990; Ramian *et. al.*, 1986], ferromagnetic core stacks with interleaved copper sheets [Booske *et. al.*, 1988; Destler *et. al.*, 1986], high current pulsed-wire designs [Warren *et. al.*, 1990], electromagnet helical microwigglers [Ohigashi *et. al.*,

1994; Vetrovec, 1990], staggered ferromagnetic core arrays immersed in a solenoidal field [Huang *et. al.*, 1994], superconducting ferromagnetic core designs [Ben-zvi *et. al.*, 1990], hybrid samarium cobalt and iron microwigglers [Tecimer and Elias, 1994], among others (see Table 3-1 for a comparative summary of recent work). A common characteristic of most of these approaches is to control and minimize field errors by means of precise fabrication while dealing with steering errors (imparting of net transverse momentum to an electron beam) and deflection (imparting a net transverse displacement to an electron beam) with internal or external trim coils (note: Tecimer and Elias used poleface shim tuning). These measures, while sucessfully employed in full-sized wigglers, have met with varying degrees of success in most of the above mentioned designs, yielding errors of order several percent RMS spread in the amplitudes of the wiggler field peaks, as well as significant uncompensated end effects (notable exceptions being Ben-zvi *et. al.*, having attained field errors of order 0.28%, and Tecimer and Elias having achieved 0.2%).

In contrast, my design employs extensive tuning to accomplish field error reduction. Each half-period is independently adjustable, permitting exertion of great control over the amplitude profile. Also, I have developed a coil/ferrocore geometry* permitting pulsed operation at very high peak field amplitudes (>4 kG) at experimentally useful repetition rates (>1/2 Hz). I have employed the tunability of our design to reduce random field errors in a 4-period prototype by an order of magnitude, from 4% to 0.4%, and to produce a 70-period microwiggler with 0.12% RMS spread in the peak amplitudes (as will be described in Ch. 3).

* Ben-zvi *et. al.* independently devised a geometry somewhat similar to ours.

2.2 Design goals and discussion

The goal of the design was to produce a device with a period λ_w of order 1 cm with gap-to-period ratio $G/\lambda_w = 0.5$, capable of producing a wiggler field in excess of 4 kG. A wiggler with parameters of this order can be used in a visible-wavelength FEL oscillator- the ultimate goal of the effort. As explained in Sec. 1.2.6, the parameter a_w plays a crucial role in the FEL interaction; its value must be maximized, while at the same time minimizing nonuniformities in the wiggler field profile. For the parameter values employed in the 70 period Microwiggler, the wiggle parameter a_w has value 0.34, and the growth per pass of a visible-wavelength oscillator based on this wiggler and the optimized ATF electron beam can be estimated to be (Sec. 1.2.6) of order 66%, using the one-dimensional linear FEL theory. A careful investigation with the three-dimensional nonlinear code TDA [Tran and Wurtele, 1990; Jha and Wurtele, 1993] yields a somewhat more modest but nervertheless useful 50% per-pass gain. Thus, a 4 kG wiggler field is entirely adequate for a visible-wavelength FEL oscillator.

This section presents a description of the geometry used to attain the design goal, and results of the analytic and computational studies upon which the design is based. I also discuss scaling laws to estimate the minimum length scales attainable with our design.

2.2.1 A simple analytic model

I began the design process by first examining a class of simple 2-dimensional designs without ferromagnetic cores, for which a simple analytic expression for the wiggler field can be derived. My ultimate design is composed of such a conductor-only geometry into which is placed ferromagnetic cores; however, the ferrocore design retains certain characteristics of the simple conductor-only case. Figure 2-1 illustrates a two-dimensional planar wiggler structure without ferromagnetic cores. It consists of an array

of parallel rectangular conductors carrying currents of identical magnitude in a configuration producing an on-axis transverse periodic magnetic field. Expressing the current density in terms of a Fourier series, and applying the Biot-Savart law, it is easy to show that the magnetic field is given by

$$\vec{B} = \hat{e}_2 \frac{8j\lambda_w}{\pi c} \sum_{n>0,n\,\text{odd}} \frac{1}{n^2} \sin\left(\frac{n\pi}{2}\right) \sin\left(\frac{n\pi W}{\lambda_w}\right) \cdot \left(1 - e^{-2n\pi T/\lambda_w}\right) e^{-n\pi G/\lambda_w} \cos\left(\frac{2\pi nz}{\lambda_w}\right) \cosh\left(\frac{2\pi ny}{\lambda_w}\right)$$
$$- \hat{e}_3 \frac{8j\lambda_w}{\pi c} \sum_{n>0,n\,\text{odd}} \frac{1}{n^2} \sin\left(\frac{n\pi}{2}\right) \sin\left(\frac{n\pi W}{\lambda_w}\right) \cdot \left(1 - e^{-2n\pi T/\lambda_w}\right) e^{-n\pi G/\lambda_w} \sin\left(\frac{2\pi nz}{\lambda_w}\right) \sinh\left(\frac{2\pi ny}{\lambda_w}\right) \tag{2.1}$$

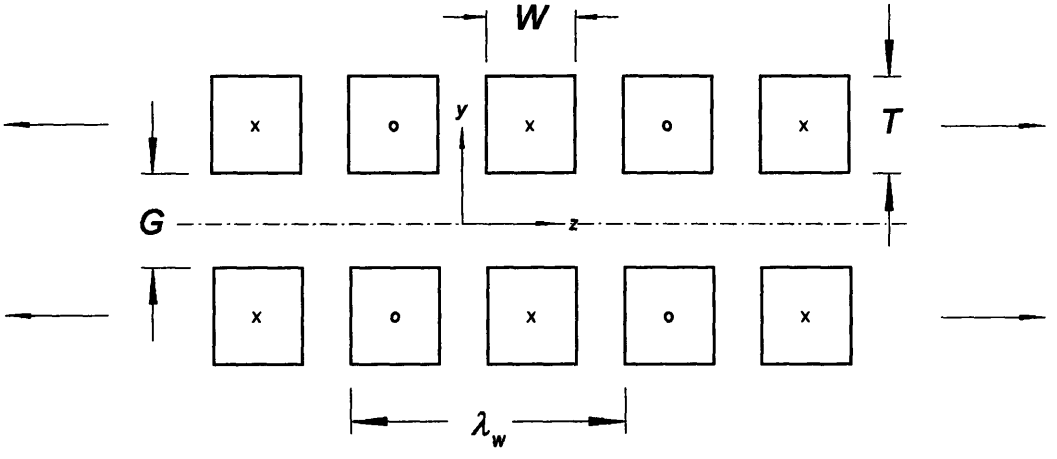

FIGURE 2-1. A two-dimensional planar conductor-only wiggler geometry. The coordinate axes and parameter definitions are shown. The structure is taken to be infinite in extent in the x-direction (into the page), and infinite and periodic in the z-direction. The conductors carry uniform currents of identical magnitude in the directions indicated: (x) - into page, (o) - out of the page.

where c is the speed of light, j is the current density in the windings, G is the gap spacing, λ_w is the wiggler period, T is the winding depth in the y-direction, and W is the winding width in the z direction. This result illustrates well-known properties of planar wigglers- exponential rolloff of field magnitudes in G/λ_w (as earlier shown in Eqn. 1.10) and the absence of even harmonics. In this specific case we observe that the current density's Fourier transform is that of a step function, which has no even harmonics. It is also interesting to note that Eqn. (2.1) has precisely the same form as the expression for the magnetic field due to a samarium cobalt magnet array in the Halbach configuration [Halbach, 1981], to an overall multiplicative constant (with the samarium cobalt magnetization being analogous to electric current), except that the samarium cobalt magnetic field harmonics fall off as $1/n$ instead of $1/n^2$. This follows from the fact that the samarium cobalt's effective current density is composed of delta-function surface current sheets, the Fourier transform of which has increased higher harmonic content as compared to that of a step function. This fact is noteworthy because harmonic content beyond the fundamental must be minimized for wigglers used in visible and UV FELs: incoherent emission from higher harmonics degrades resonator cavity optics downstream from the wiggler.

A computer simulation which explicitly sums the contributions of individual conductors shows that the analytic model (2.1) is useful for describing structures with a finite number of periods. A finite structure having a current distribution symmetric in z and having half-width conductors at the ends produces a field profile closely modelled by Eqn. (2.1) at points more than a couple of periods from the ends of the structure. The computer calculations also show that a structure finite in the x direction (Fig. 2-1) is also well-modelled by (2.1) as long as the device extends in x more than a couple of wiggler periods.

Another important observation regarding Eqn. (2.1) is the dependence of the field strength on the winding depth T and the winding width W (see Fig. 2-1). The dependence of the fundamental harmonic's magnetic field strength on T/λ_w is as $\left(1-e^{-2\pi T/\lambda_w}\right)$, which asymptotes to unity for large T/λ_w. Given that a real device's electrical resistance will scale as T and the inductance scales as T^2, it is clear that extending T without bound is unwise. Also, the fundamental harmonic scales with W/λ_w as $\sin(2\pi W/\lambda_w)$, so even though maximal field strength is obtained for $W=\lambda_w/2$ (no space between conductors), the loss of amplitude as W is decreased from $\lambda_w/2$ to $\lambda_w/4$ (leaving room between conductors equal to their width) is only about 30%. Interstitial placement of ferrocores is therefore possible without serious degradation of the field from the conductors, which drives magnetic field production by the ferrocores.

Finally, it is observed that a conductor-only design with $\lambda_w = 1.0$ cm, $G = 0.5$ cm, $W = 0.211$ cm, and $T = 0.211$ cm (corresponding to 81 turns of 32 AWG wire per coil) will produce 68 G of wiggler magnetic field on axis per ampere of current. This is only about a factor of 2 below that needed for a useful device; thus, the expedient of adding ferrocores should suffice to produce a practical design capable of producing >4 kG at a useful repetition rate. The analytical model and computer integration of the Biot-Savart law permit the conclusion that a simple, effectively two-dimensional conductor-only design can be used to produce reasonably large on-axis fields in a short-period wiggler configuration: it only remains to show that ferromagnetic cores can adequately augment the field strength.

2.2.2 Numerical studies of a ferrocore-based design

The motivation for using ferromagnetic cores extends beyond enhanced wiggler field strength. The ferrocores can be embedded in an external matrix formed with very

high precision, thus precisely fixing the core positions. Inasmuch as $\approx 2/3$ of the field is produced by the ferrocores' induced magnetization, there is great advantage to be gained in field precision by exactness in their location. Moreover, the ferrocores can be embedded in a matrix possessing good thermal conduction, which permits reasonably efficient cooling of the coils during operation. This approach is in contrast to designs in which the

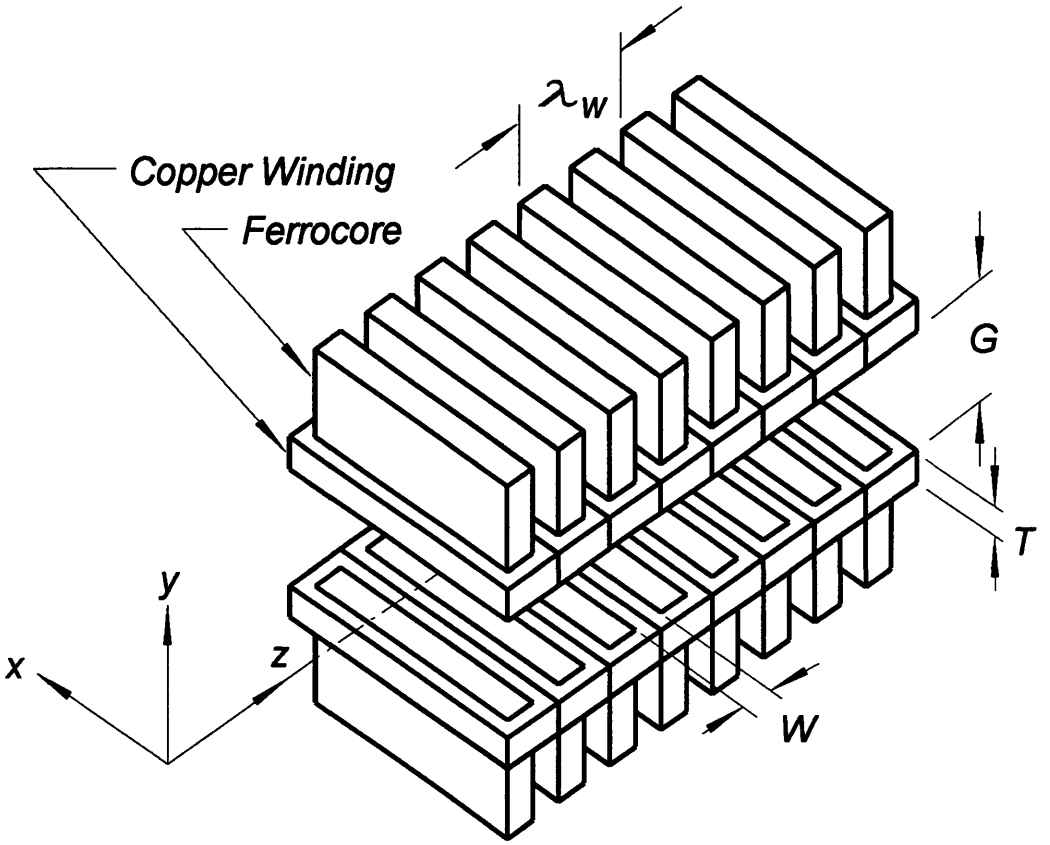

Figure 2-2 A wiggler geometry incorporating ferromagnetic cores. Coordinate axes and design parameter definitions are shown. Current flow in adjacent coils have opposite handedness, while current flow in cross-gap pairs have the same handedness. Note that the gap shown is larger than in the actual design.

wiggler is formed from a stack of alternating conducting and ferromagnetic laminates [Booske *et. al.*, 1988]: such a stacking arrangement allows for cumulative field periodicity errors. The use of individual cores also enables construction of individual coils, permitting

separate electrical connection of each coil and the independent adjustment of current fed to each coil.

The design process was continued by studying the effect of placing ferromagnetic cores into the interstices of the copper-only design of Fig. 2-1. Figure 2-2 illustrates the geometry arrived at, in the form of a 4-period wiggler: the T,W,G,λ_w dimensions shown correspond to those in Fig. 2-1. The POISSON code was used to determine appropriate values for the conductors' size and placement (POISSON is a 2-dimensional Laplace/Poisson equation solver which has features permitting computation of magnetic fields in the presence of ferromagnetic materials). Eqn. (2.1) suggests that the ferrocore depth (in analogy to the conductor depth T), when increased to beyond a wiggler period or two, will stop playing a role in the field strength and shape; this was indeed found to be the case in the POISSON simulations. Thus, the design effort focussed on finding appropriate values for $T/\lambda_w, W/\lambda_w$ with G/λ_w set at 0.5, a value adequate to ensure passage of an electron beam with $\lambda_w \approx 1$ cm.

Ferromagnetic core saturation becomes an issue when high wiggler field values are desired. The wiggler field strength as a function of coil current will be linear until some portion of the core material starts to saturate. This concern was actually the main determining factor in choosing T/λ_w, in that the field strength increases very slowly with additional current once saturation has started to occur, thus making attainment of large fields impossible. It was observed in the POISSON simulations that increasing T for fixed wire diameter and and ferrocore widths increased B/I efficiency in the linear regime, but lowered the field at which saturation occurred. The B/I efficiency varied roughly linearly with T, and the product of the B/I efficiency and the saturation field was roughly constant. I settled on a design which produced 150 Gauss per ampere into 32 AWG wire in its linear regime; the onset of saturation occurred at around 3.2 kG (computed

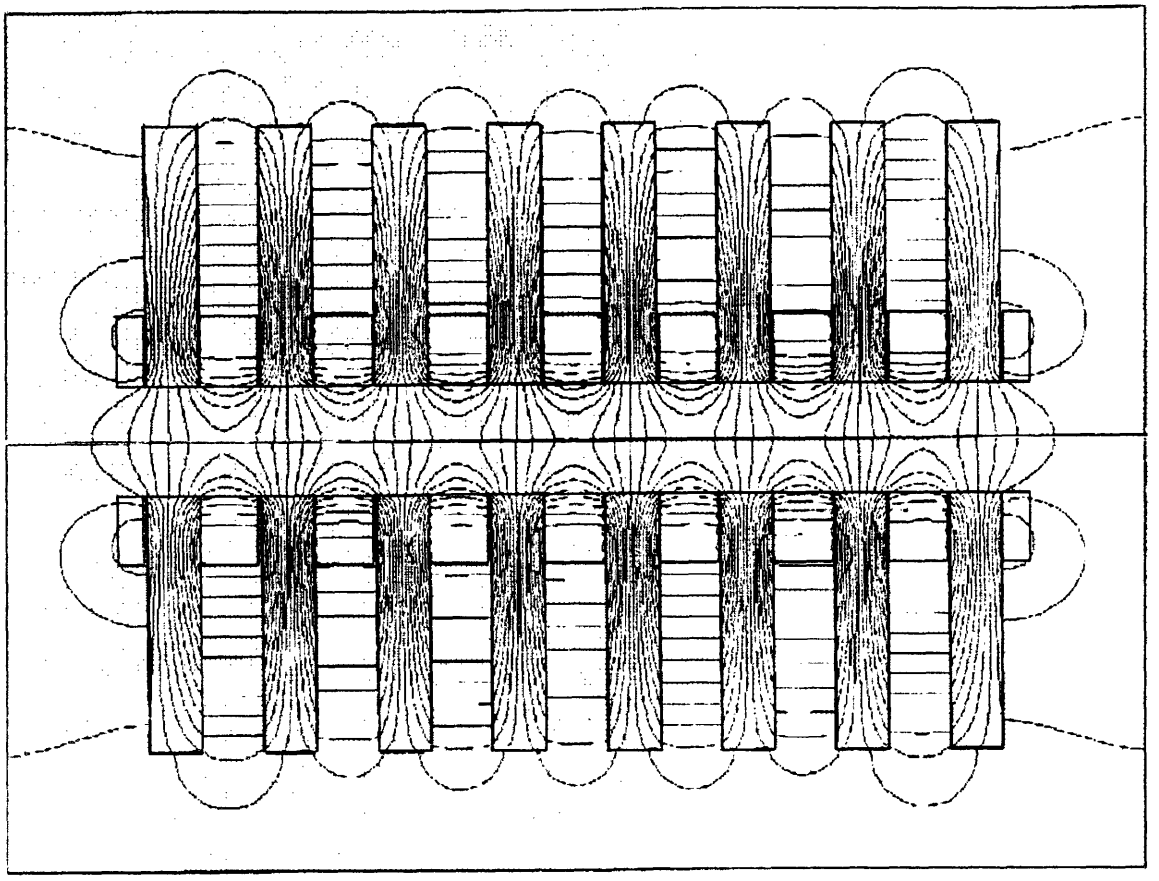

FIGURE 2-3. POISSON-generated equipotential map for the 4-period prototype.

saturation profiles are compared to measured values in Sec. 2.3 below). A POISSON-computed field equipotential map of the final design is shown in Fig. 2-3. The design parameter values are $W/\lambda_w = 0.25$, $T/\lambda_w = 0.25$, with a ferrocore width of $0.25\lambda_w$ and a depth of $1.25\lambda_w$.

The POISSON analysis proved the feasibility of adding ferromagnetic cores to augment the simple "copper-only" design and boost the attainable field amplitudes to levels usable in a microwiggler FEL. It remained necessary to develop a specific electromechanical implementation of the design, and to characterize the performance of a prototype based on it.

2.2.3 A physical limitation of a two-dimensional design

There is a very important limitation placed on a two-dimensional planar wiggler design, by the requirement that $\nabla \cdot \vec{B} = 0$. The net magnetic flux through the wiggler's midplane (*i.e.*, the *x-z* plane of Fig.2-1) must be zero. This is a desirable fact from the point of view of electron propagation through the wiggler, since for $\gamma >> 1$ an electron injected on axis with no *x*-component of momentum will not be steered (*i.e.*, acquire momentum in the *x* direction) as a result of its interaction with the wiggler field. However, the electron will inevitably emerge with some *x displacement,* since the wiggler field contains amplitude and periodicity imperfections and imperfect compensation for end effects. Tuning the profile so that the integral of the magnetic field internal to the wiggler (*i.e.*, excluding the end peaks) is zero will ensure that global return flux doesn't result in exaggerated flux integrals for the end peaks, which would lead to a serious displacement problem.

2.3 Experimental results on a 4-period wiggler prototype

I constructed a 4-period prototype microwiggler to verify the ability of our design to produce large magnetic fields, and to show that the extensive tunability afforded by the use of individual coils could be exploited to reduce random field errors and end effects. The prototype had a period $\lambda_w = 10.2$ mm and a gap $G = 5.1$ mm, and consisted of 16 copper wire coil electromagnets held in place by an aluminum matrix. Each coil consisted of 50 turns of 32 AWG copper wire (0.0202 cm dia.) and had a resistance of 2.4 Ω. The ferromagnetic cores each consisted of seven Microsil* laminations of dimensions 1.27 x 3.81 x 0.0356 cm. Figure 2-2 illustrates the geometry *sans* aluminum matrix. The aluminum matrix consisted of two pieces, one for the coils on each side of the gap, into which slots had been cut. The cores were then inserted into the slots, and held in place by

* A cheap aluminum-iron-silicon alloy with reasonably high saturation fields and low hysteresis and remnant fields; commonly used in transformer coils.

friction; the two halves were then attached to one another to yield the configuration of Fig. 2-2. Figure 2-4 illustrates the electrical connections of the electromagnet coils. Electrical connection was implemented with each pair of coils facing one another across the gap hooked up in parallel, in such a fashion that they induced the same-sign magnetic field at gap center; adjacent half-periods were oriented so as to induce oppositely-directed magnetic fields at gap center, resulting in a wiggler field configuration. The eight half-periods were each wired in series with precision potentiometers, so that the current delivered to each half-period was independently adjustable.

The wiggler was energized by a simple pulser circuit composed of an air-core inductor ($L = 1.3$ mH) and a bank of six 1500 μF electrolytic capacitors connected in parallel. The resulting waveform was an underdamped sine wave. The pulser fired by an SCR which commutates off at the first zero-crossing of the current, so that the wiggler was energized by a single positive current pulse. The full period of the underdamped waveform was about 22 msec. This pulse is very long in comparison to the L/R risetime of the coils (≈ 70 μsec). The pulse was made long enough to permit use of the Hall probe gaussmeter, which had a bandwidth of order 60 Hz: in contrast, the duration of the pulse in the 70-period microwiggler was made much shorter to reduce thermal loading in high-repetition-rate operation.

The wiggler field amplitude as a function of the input current density was measured and is plotted in Fig. 2-5, along with the results of a POISSON simulation. The POISSON simulation matches the data very well- this is partly fortuitous insofar as we made no effort to model the permeability of our particular material, and used the default POISSON permeability model* . The probe was located at a peak near the central part of

*The POISSON code uses a magnetic permeability model based on the properties of iron. It also permits the use of a model based on the properties of a different permeable material, if desired.

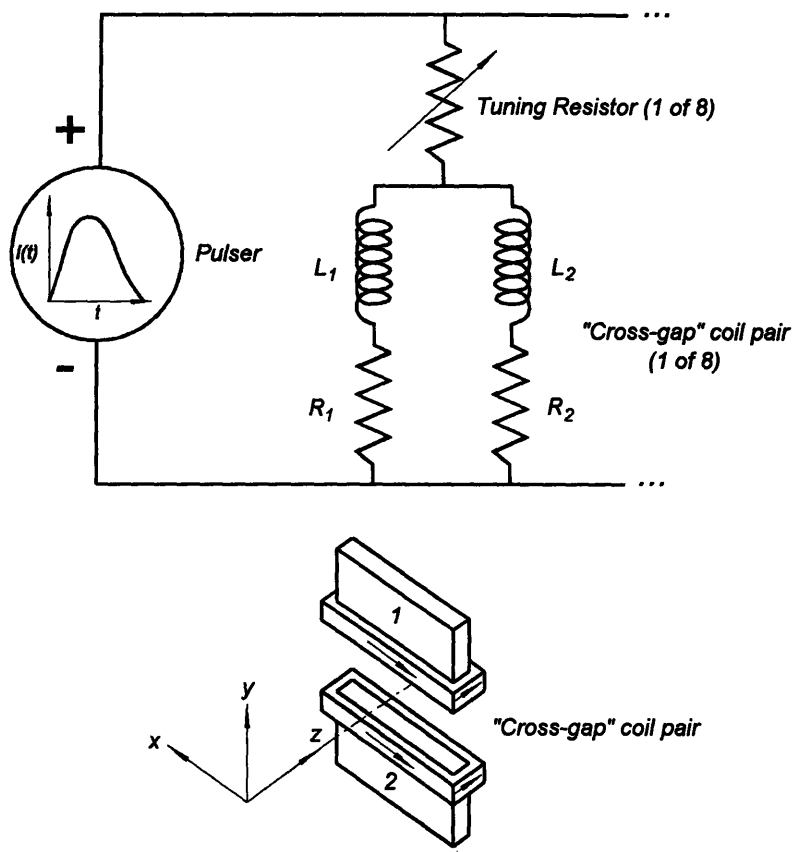

FIGURE 2-4. Wiggler electrical connections. A cross-gap coil pair is shown along with the electrical schematic equivalent. The direction of current flow in the conductors is indicated by arrows.

the wiggler; the input current was measured using a Rogowski coil and the field was measured by means of a Hall probe gaussmeter. The gaussmeter probe employed a specially-designed miniature probing tip. The current values shown in Fig. 2-5 are those borne by the 32 AWG wire: a current of 20 A corresponds to a current density of 6.2×10^4 A/cm^2 . As earlier noted, B as a function of I is linear to about 3.2 kG. This linear field regime extends further than several ferrocore designs reported previously [Booske *et. al.*, 1988]. Referring to the flux map of Fig. 2-3, it is seen that the regions of highest flux density occur inside the windings. The closer to the polefaces the higher will

be the fields at the polefaces (and on the wiggler axis) when the poles saturate. Thus, a major benefit of keeping the winding thickness T small, as opposed to extending them to the full length of the ferrocores, is to postpone the onset of saturation to relatively high field levels by displacing the highest-flux density regions towards the polefaces.

Having attained high fields, I then used the extensive tunability (via adjustment of

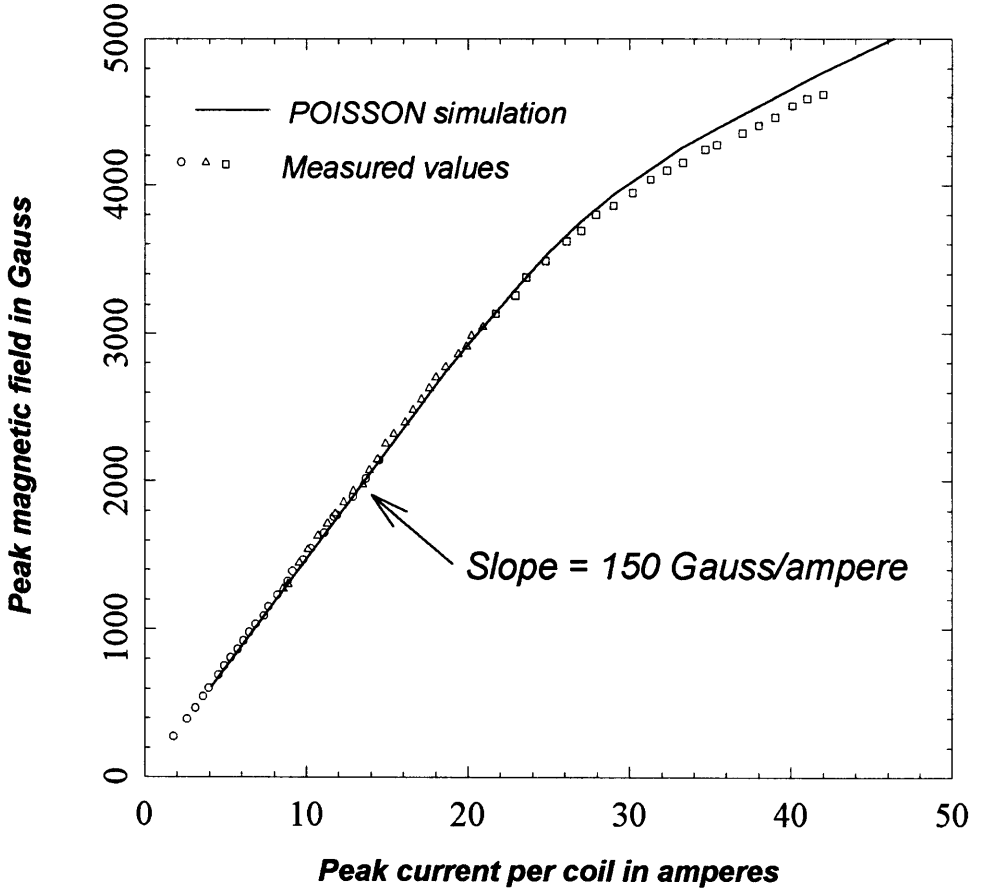

FIGURE 2-5. Saturation characteristics of the magnetic field generated in the Microwiggler prototype. A Hall probe gaussmeter was used for the measurements, so that the absolute magnetic field calibration is reliable to about ±3%.

the tuning resistors shown in Fig. 2-4) of the system to dramatically reduce random field errors and systematic (undesired) finite-wiggler end effects. Figure 2-6 shows two tuned field profiles, developed in low-current (0.5 A/coil) DC operation. The first is a uniform-field-amplitude profile in which the RMS spread in the peak amplitudes is 0.4%, a reduction of an order of magnitude from the untuned profile. The second profile shows a profile in which the peak amplitudes increase linearly inward from the ends; this profile demonstrates the capability of installing an adiabatic up-taper for wiggler/electron-beam matching. The field's variation in the cross-gap y-direction was also measured, and is shown in Fig. 2-7. The data are again well-matched by the POISSON code, and by a hyperbolic cosine curve, as one would expect from eqn. (1.9). The measurements extended only over the range (y = -1 mm to y = 1 mm) because of Hall probe impingement on the polefaces. The field is very symmetric about the wiggler center.

Heat dissipation is a major concern in any electromagnet with normal (as opposed to superconducting) conductors. In fact, it is the principal factor limiting the rate at which a magnet of this design can be pulsed. Figure 2-8 shows measurements of coil temperature as a function of input current, acquired by embedding a K-type thermocouple between two adjacent coils in the prototype. The prototype was cooled by passing chilled water through a channel in the aluminum coil holders. The temperature is clearly a quadratic function of the input current: since the thermal loading varies as I^2, the temperature must be a linear function of the thermal load. This justifies the assumption of conductive cooling in the scaling law discussion of Sec. 2.3. We can also calculate the maximum attainable pulse repetition rate permitted by thermal constraints: assuming that the "sink" temperature of the aluminum holders can be maintained at 5° C, the coils will be 95° above the sink temperature when operated at 100° C. This is a high, but reasonably safe, operating temperature. With 0.4 msec pulses of 45 amperes per coil (which produces wiggler fields in excess of 4 kG), the repetition rate corresponding to the 95° temperature difference is

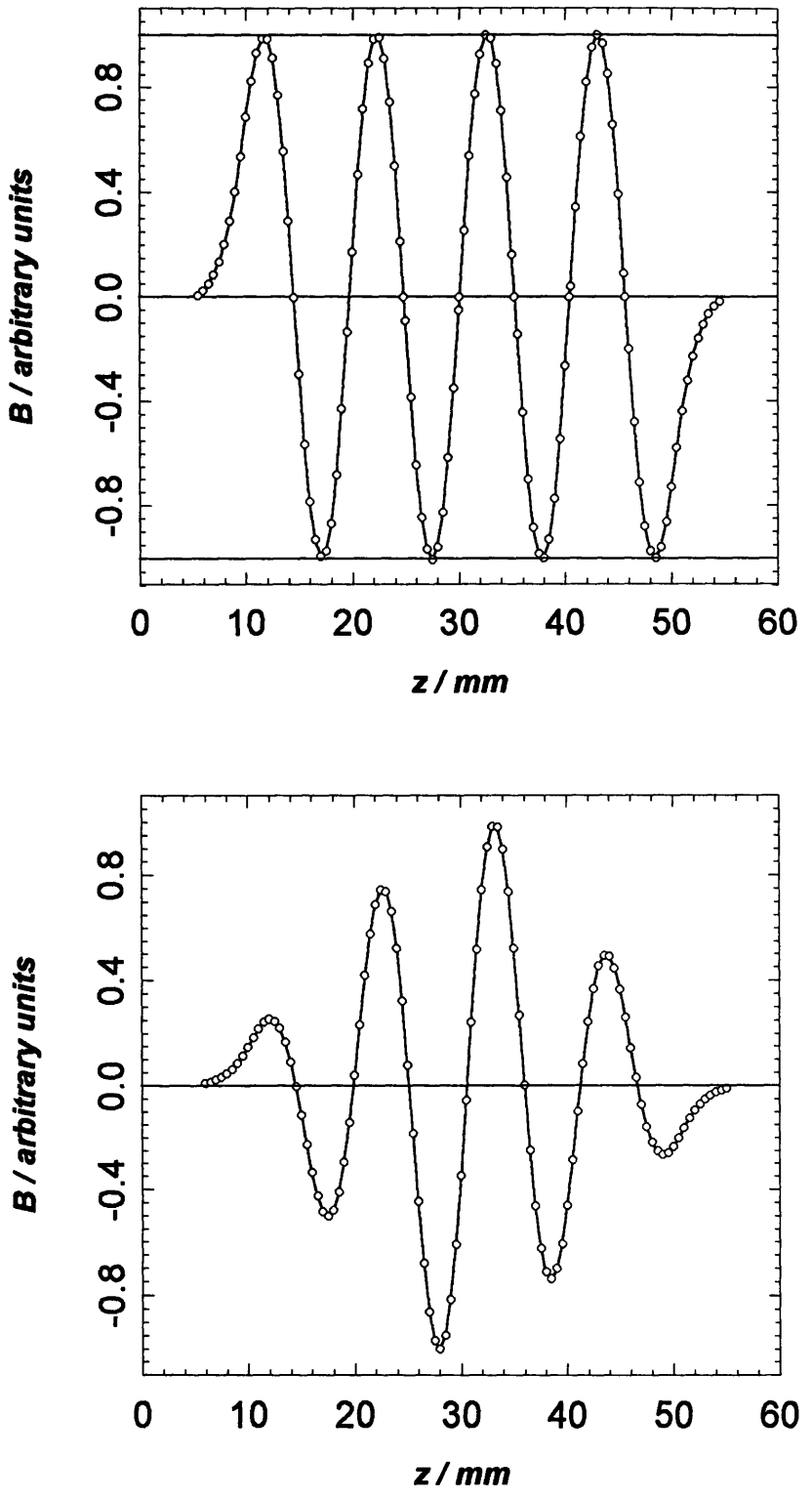

FIGURE 2-6. Tuned axial field profiles in the Microwiggler prototype. The flat profile at top has a 0.4% RMS spread in the peak amplitudes. The ramped profile at bottom is a demonstration of the tapered profile capability of this design.

about 1.7 pulses/second. This is a useful repetition rate, at a useful operating field magnitude; thus, thermal limits do not forbid operation of a magnet of this design. It should also be mentioned that immersing the coils in a refrigerated oil bath would provide much more efficient cooling and permit a greatly increased repetition rate.

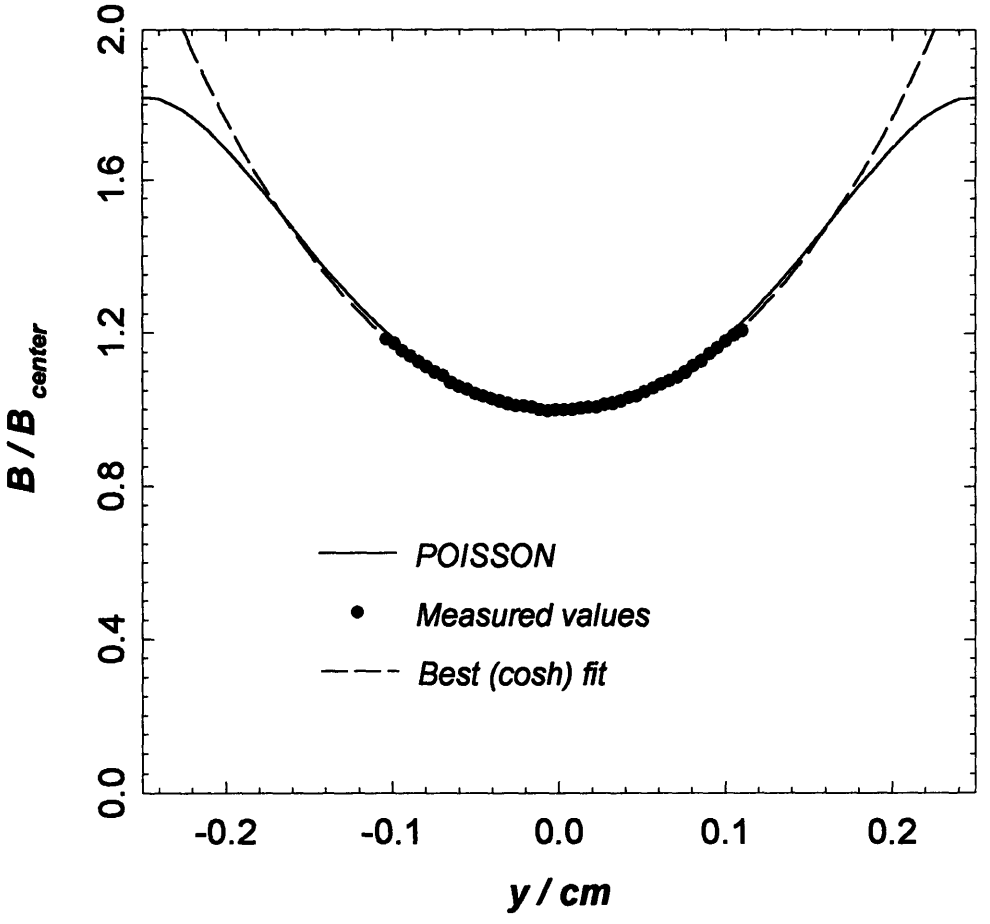

FIGURE 2-7. The prototype Microwiggler field vs. *y* (cross-gap variation). The range of the measurements was restricted by impingement of the Hall probe on the polefaces.

2.3 Scaling Laws

In a design effort with the goal of length scale reduction, it is imperative to derive relationships describing the performance of a given design geometry with length scale.

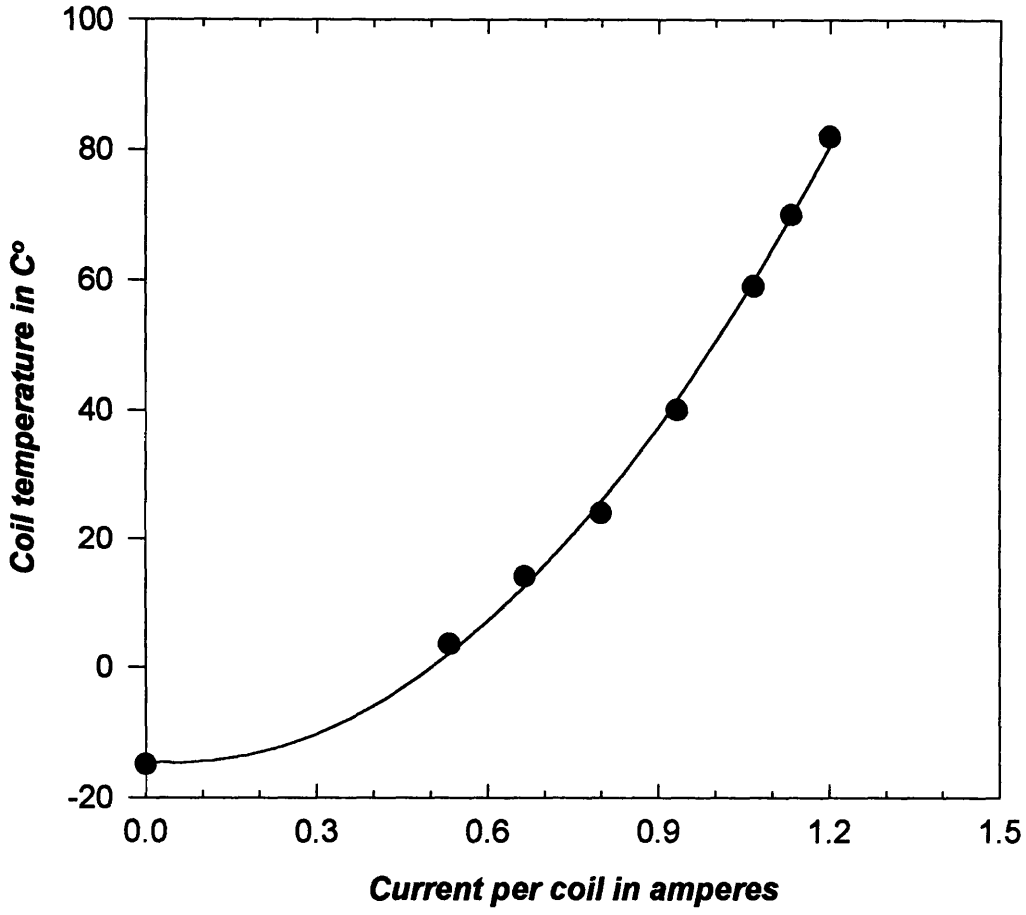

FIGURE 2-8. Coil temperature as a function of coil current. The quadratic variation is indicative of conductive cooling. The indicated temperatures are relative to room temperature of about 20° C.

Brau presents scaling relations for wiggler field amplitudes in comparing the performance of superconducting vs. permanent magnet wigglers in the limit of small wiggler period [Brau, pp. 272-273]. This is adequate for a discussion of non-pulsed magnets*, but in the

* It is worth noting that recent technology developments are at variance with the conclusions of Brau's discussion. He states that permanent magnet wigglers perform better as $\lambda_w \rightarrow 0$. Ben-zvi et. al., have built a prototype superconducting microwiggler section ($\lambda_w = 8.8$ mm, $G/\lambda_w = 0.5$) which produces very high fields (>5 kG) with small field errors (1/4% RMS spread in the peak amplitudes). I know of no similar performance being attained in a permanent magnet with anything approaching that small a period and large gap-to-period ratio.

case of a pulsed device, the length scaling of parameters such as resistance, inductance, and thermal cooling times must also be considered [Stoner *et. al.*, 1990].

Let us now consider the effects of scaling a ~1 cm period design to 5 mm period (the smallest length scale at which our fabrication techniques would be effective). We see from Eqn. (2.1) that the amplitude of the magnetic field scales as

$$|\vec{B}| = j \cdot \lambda_w \cdot f(G/\lambda_w, T/\lambda_w, W/\lambda_w). \tag{2.2}$$

where $f(G/\lambda_w, T/\lambda_w, W/\lambda_w)$ is a function independent of length scale. It can be easily shown that a ferrocore system in its linear B/H regime has the same kind of scaling, i.e., the field magnitude scales like ($j \cdot \lambda_w \cdot$function invariant under length scale). The 5 mm-period design then requires twice the current density to attain a given field level, compared to the 1 cm-period design. To maintain a given field amplitude and given temperature increase per shot, field pulse durations must be reduced by a factor of 4 in the 5 mm-period design.

The saturation field of the 5 mm-period design is the same as that of the 1 cm-period design (since the saturation field is a bulk property of the ferromagnetic material), and the L/R risetime of the 5 mm-period structure is one-fourth that of the 1 cm-period system. One can also easily show that the characteristic conduction cooling time of the 5 mm structure is one-fourth that of the 1 cm-period design.

This factor-of-four reduction in the cooling time resulting from the length scale reduction permits the 5 mm-period device to operate at four times the pulse repetition frequency of the 1 cm-period design, assuming a fixed temperature increase per pulse. This more rapid pulse rate is possible because the L/R risetime is four times smaller in the

smaller structure, and the timescale of the current waveform can thus be compressed without increased applied voltage. Reducing the duration of each pulse by a factor of four permits the doubling of the current density with no change in the temperature increase per pulse, so that the same $|\vec{B}|$ can be attained during the shorter pulse in the smaller structure. This implies that the smaller structure can produce magnetic fields of a given magnitude having one-fourth the pulse duration at four times the rate- so that the time-averaged $|\vec{B}|$ attainable by the 10-mm-period design can also be generated by a 5 mm-period wiggler.

Alternatively, one could keep the pulse repetition rate fixed, and double the input current into the 5 mm-period device, thus doubling the field magnitude in the 5 mm-period device, while preserving the same average operating temperature. This would imply that the value of the wiggle parameter a_w is preserved in the scale length reduction when the repetition rate is held fixed. This is of very great interest and importance, because the FEL gain per unit length would also be maintained under the length scale reduction.

The fixed-repetition-rate analysis makes the important assumption that the ferromagnetic cores are operating in their linear regime. This is not the case at the operating point of the 70-period microwiggler of Ch. 3. Both analyses (the fixed-rep-rate analysis and the fixed-time-averaged-field analysis) assume that the ferrocores' permeability is not a function of the temporal frequency of the applied currents. This assumption would not hold up under a factor-of-four reduction in the pulse duration. What operational mode *could* be attained in a factor-of-two scale length reduction in a practical design? The ferromagnetic cores can operate with a factor-of-two reduction in the pulse duration (as opposed to a factor-of-four as in the above scenarios). Thus, one could operate a 5 mm-period device at twice the repetition rate and the same peak field as a 1 cm-period device. Alternatively, one could fix the repetition rate and increase the excitation current by a factor of $\sqrt{2}$ (which will keep the operating temperature fixed),

which would result in an increase in the peak magnetic field amplitude of roughly 18%. Thus, the wiggle parameter a_w would decrease in the 5 mm-period device to ~60% of that of the 1 cm-period device, rather than being maintained at the same value in the length scale reduction as was the unsaturated, infinite-bandwidth ferrocore case.

2.4 Conclusions

We began with a simple conductor-only design for a short-period wiggler, and extended that design's capability with the judicious use of ferromagnetic cores as informed by the POISSON code. The prototype based on our design effort behaved in close conformity with theoretical predictions, producing wiggler fields in excess of 4.6 kG. We were also able to exploit the extensive tunability of the device to produce a uniform field profile with RMS variance in the peak amplitudes of 0.4%, a very respectable value. The design and prototype efforts therefore strongly indicated the feasibility of constructing a full-scale (tens of periods) microwiggler capable of producing large field amplitudes with small random field errors and minimal end effects. The next chapter describes the considerable effort of building a full-scale, operational 70-period microwiggler which has exceeded the promise of the prototype.

CHAPTER 3

A 70-PERIOD HIGH-PRECISION MICROWIGGLER FOR FREE ELECTRON LASERS

3.1 Introduction

This chapter describes the construction, tuning and performance of a high-precision 70-period planar electromagnet microwiggler based on the design described in the preceding chapter. The extension of the 4-period prototype to a full-sized experimental apparatus was a major effort; there were several major issues to be addressed in order to do so. In the prototype, I demonstrated adequate tuning while energizing the wiggler with small DC currents. The same or better results had to be obtained in pulsed mode at high fields. Also, I tuned the prototype field using a trial-and-error approach. Increasing the number of periods by a factor of 17.5 (to 70 periods) represented an enormous increase in complexity. I needed to establish effective, systematic control over the 140 available adjustments in a 70-period device, to achieve a highly uniform field with minimal end-effects*. In the prototype effort, I operated an 800-ampere pulser to energize the microwiggler prototype, which was fired at a rate of about one shot per minute. A pulser for a full 70-period microwiggler must produce 12 kA pulses, at high repetition rates (>30 shots/min), with great stability- a huge performance advancement over the prototype pulser. Such a device had also to be constructed at modest cost.

This chapter documents how these problems were solved. Section 3.2 describes the construction of the Microwiggler and the pulsed power supply used to energize it; Section 3.3 presents the measured performance of the Microwiggler. Section 3.4 discusses the novel method for tuning the Microwiggler, and the computer control for wiggler current stabilization and magnetic field measurement. Section 3.5 describes a simple means

* That this was possible was by no means obvious at the outset. A reviewer of [Stoner *et. al.*, 1990] commented that in his opinion our tunability scheme was not applicable to a full-scale device.

of converting the measurement system from measuring peak amplitudes to measuring field integrals. I conclude with a discussion of the factors which define the ultimate limits of this technology's field precision, and an attempt to extrapolate the characteristics of the existing device to estimate the technology's best attainable field precision.

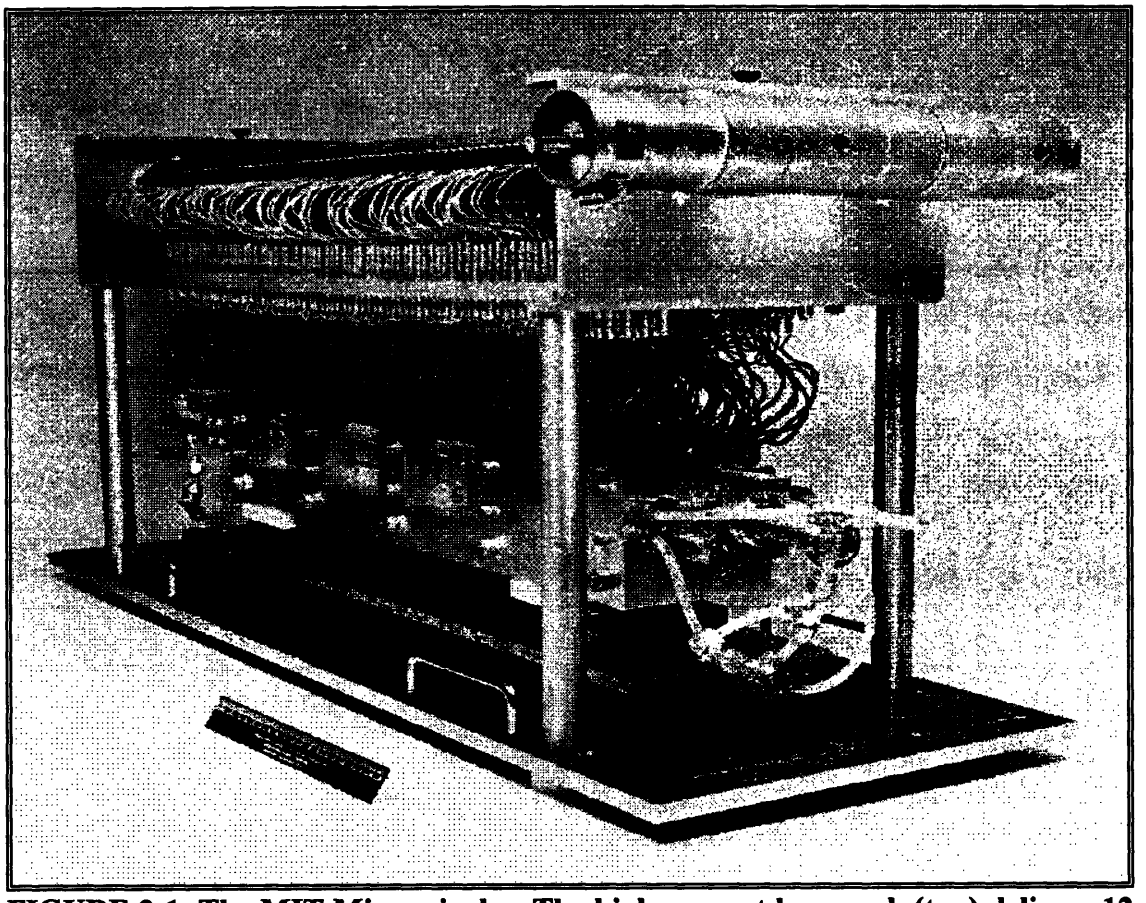

FIGURE 3-1. The MIT Microwiggler. The high-current busswork (top) delivers 12 kA in 0.5 msec pulses, which is distributed by the current distribution network. Current is delivered to each of the 280 coils by way of a 22 AWG twisted pair.

3.2 Construction of the microwiggler and pulsed power supply

The Microwiggler is a 70-period device with an 8.8 mm period and a 4.2 mm gap, consisting of 280 electromagnets held by a precisely formed aluminum matrix. Figure 3-1 is a photograph of the Microwiggler (refer to Fig. 2-2 for an illustration of the geometry). Each electromagnet is formed from wire wound on a core consisting of six Microsil

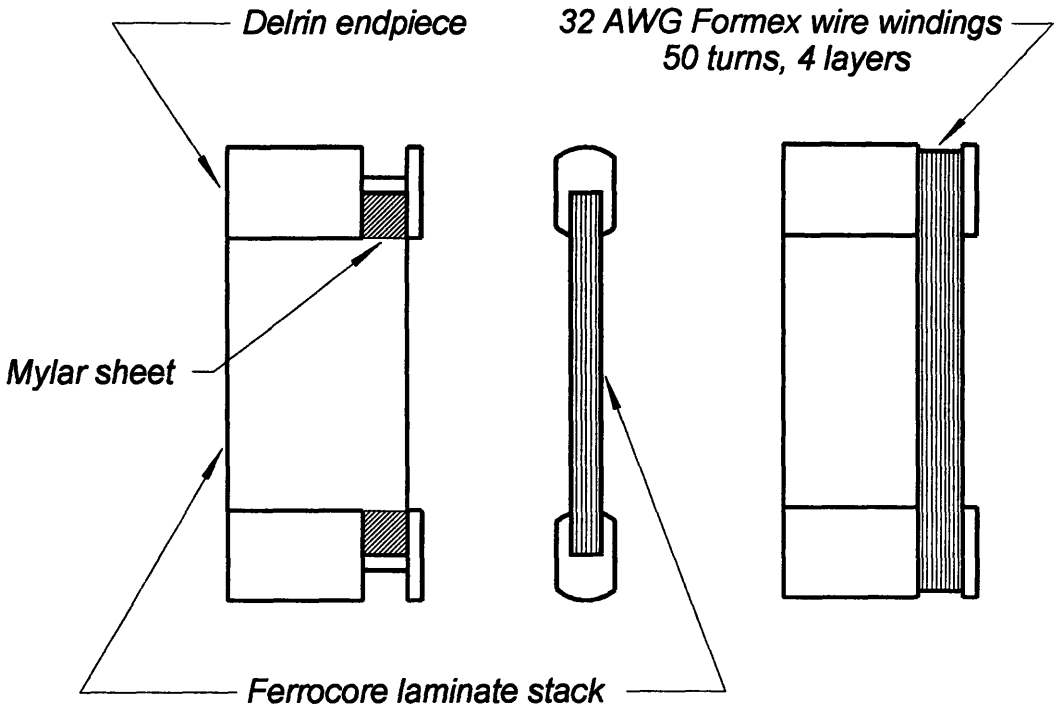

FIGURE 3-2. An individual electromagnet. The side view on the left shows a core without windings, to better illustrate the structure of the core/endpiece assembly. The mylar sheet is indispensible: in tests, fully half of coils made without it were electrically shorted to the core, a catastrophic failure rate.

laminations of dimension 1.27 x 2.54 x 0.035 cm (29 gauge). Microsil was chosen in favor of more exotic materials (like vanadium permendur) because of its extremely low cost and ready availability, and its very small hysteresis and remnant fields. A very high degree of uniformity was achieved in the thickness of the laminated cores: the thicknesses of all 280 cores lay within a range between 2.101-2.106 mm, a spread much smaller than that of the individual laminates, the thicknesses of which varied over a range 0.345-0.371 mm. The uniformity of the magnet cores was attained by organizing 2000 pieces of the individual laminates into a distribution with bin size .00254 mm by means of micrometer measurement of each piece, and then selecting sets of six laminates with the appropriate total thickness. Figure 3-2 shows an individual electromagnet. In each electromagnet, 50 turns of 32 AWG Formex wire were laid down in four layers; the position of the windings

was secured by Delrin* end-pieces, which also served to hold together the laminate stack comprising the ferrocore. Each of the electromagnets was hand-wound. To prevent electrical shorting, .05-mm thick Mylar was placed over the ends of the core stacks, under the endpieces; this eliminated electrical contact between the sharp laminate ends and the windings. After assembly, the windings of each electromagnet were painted with unthinned Glyptol varnish to secure their position; the electromagnets were then baked overnight at 80° C to cure the varnish. After baking, excess varnish was removed from the ferrocore with a razor blade.

The coil holder matrix consists of two aluminum holder pieces, lying on each side of the wiggler gap, which are aligned across the gap by a pin-and-socket arrangement at each end of the holders. Each holder consists of a bar fashioned from aluminum jig-plate stock with 140 slots cut perpendicular to the longitudinal axis of the bar, each of which accomodates an individual electromagnet.

The coil holders were manufactured with considerable precision. Neither the width nor the cumulative (axial) positional error of any of the 140 coil holder slots in each holder exceeds 0.01 mm. The high precision of both the slots' widths and the ferrocores' thicknesses obviated the need for the use of shimming when the ferrocores were installed into the holders. The principal force securing the electromagnets is the ferrocores' fit in the holder slots; this is augmented by sandwiching a piece of 1/4" foam rubber sheet between the polefaces above and below the vacuum drift tube. A 0.025-mm Mylar sheet insulates the pole faces from the drift tube. Note that neither the drift tube nor the foam rubber play any role in establishing the cross-gap separation of the wiggler halves; that separation is determined by the aluminum holders. Figure 3-3 is a section drawing showing the assembly of the wiggler halves, drift tube, etc. The electron drift tube consists of a 75 cm

* Delrin is the trade name for a strong, easily-machined plastic that is somewhat harder than nylon.

length of 0.25 mm-wall-thickness stainless steel K_a band waveguide, with stainless mini-CONFLAT flanges braised onto each end. Longitudinal slots cut into each end of the magnet holders secure the drift tube position. The transverse position of the drift tube is also very well-fixed by the polefaces; this is crucial because the pickup coil probe for magnetic field measurements takes its position via a slip fit inside the drift tube. Measurement of the relative height of each of the 280 polefaces shows that the highest polefaces are randomly distributed through the wiggler, and that they fix the transverse (y) position of the drift tube to less than 20 microns. Drift tube wall thickness variations thus yield as much (or more) drift tube position error as poleface height variations.

Having assembled the individual electromagnets into the magnet holders, and then assembling the two holders with the drift tube and wiring harnesses, it remained to provide connection of the electromagnets to a current source. As in the prototype, electromagnets facing across-gap from one another comprise a half-period, and are connected in parallel to ground and to the current source through a tuning resistor (see Fig. 2-4). Thus, the wiggler circuit consists of 140 such half-period pairs, in turn connected in parallel to the current source. The tuning resistors consist of 22 AWG manganin wires, the lengths of which are varied to adjust their resistances. Tuning of the magnet therefore consists of adjusting the value of 140 resistors in a resistive current divider network.

The pulsed power supply must energize the wiggler such that the resistances of the coils dominate over their inductances in determining the distribution of current among them. This will be the case as long as the current pulse duration is much greater than the mean (L/R) time of the various half-periods. The (L/R) time of the wiggler (at below-saturation fields) is about 60 μsec. From Fig. 3-4 we see that the current pulse is an underdamped half-sine wave with time from pulse onset to zero-cross of about 880 μsec.

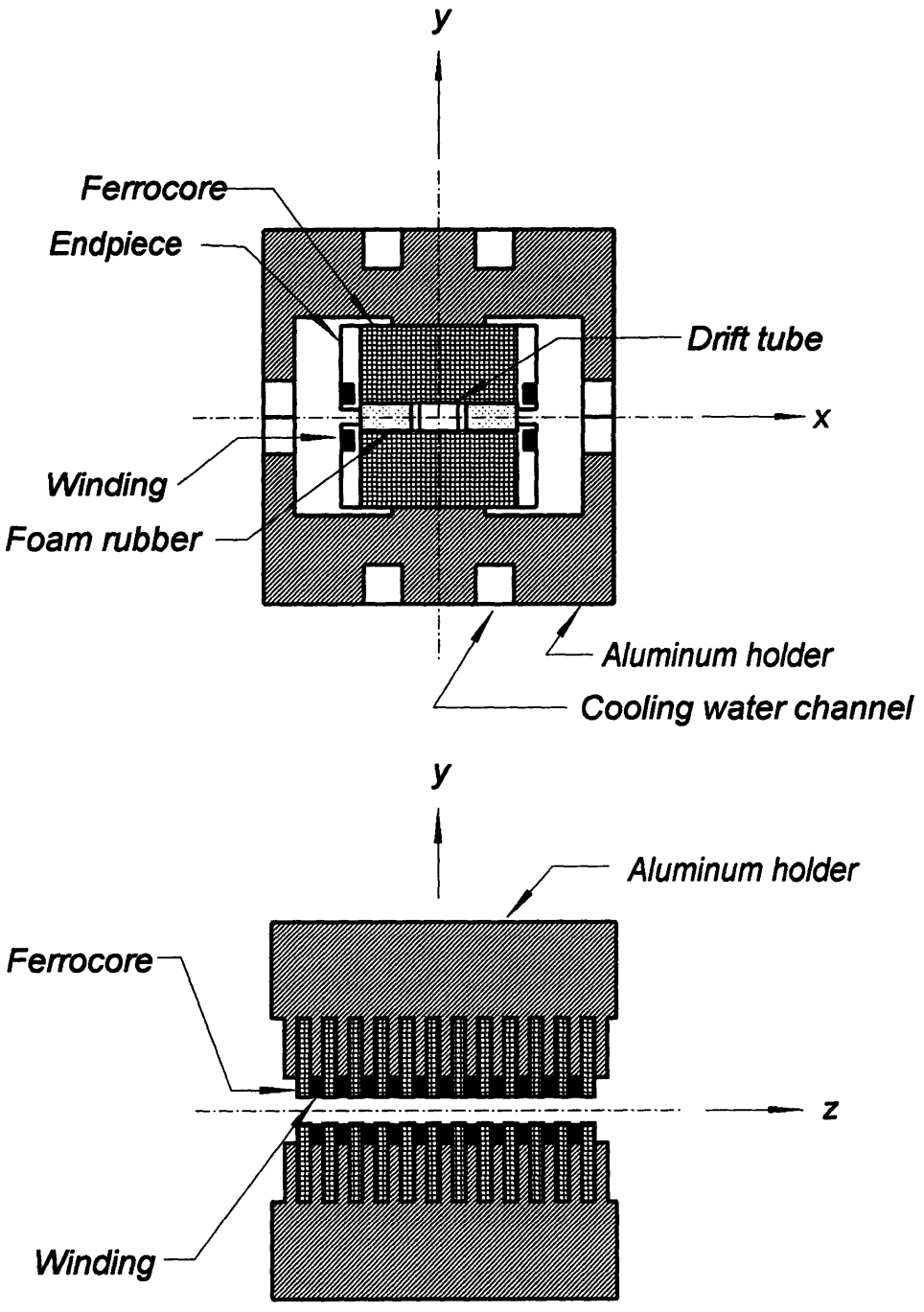

FIGURE 3-3. Wiggler assembly section drawings. The top view shows how the holders, coils, and drift tube are assembled. The bottom view illustrates the installation of the coils into the aluminum holders.

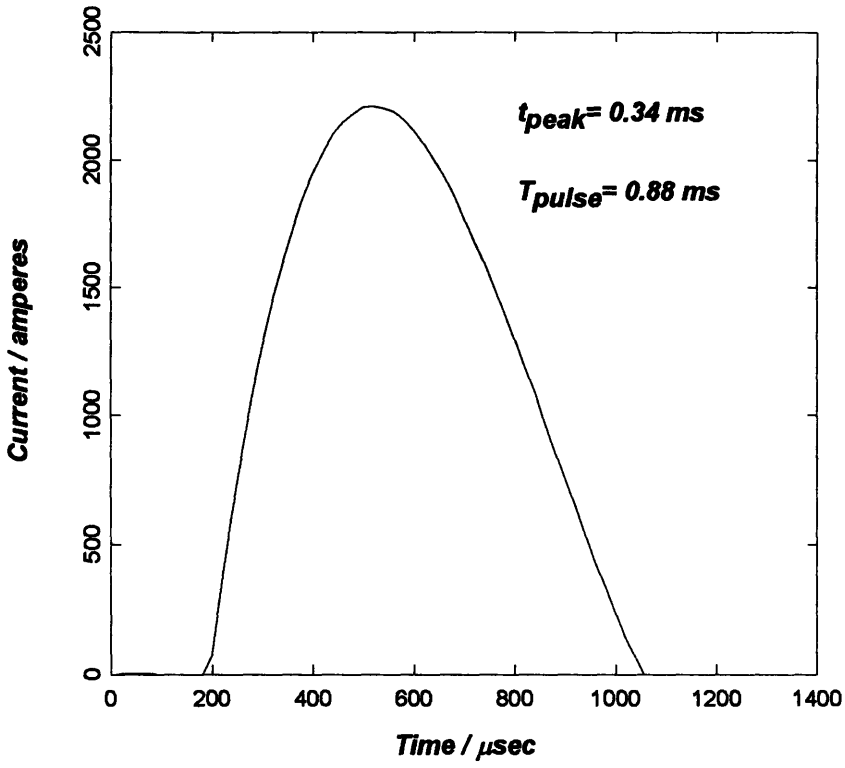

FIGURE 3-4. The current pulse produced by the Microwiggler pulsed power supply. This is a low-power shot (bank voltage of 100 V): peak current in typical operation is 12.5 kA. The time from current turn-on to peak is about 0.34 msec, and from turn-on to zero-cross is about 0.88 msec.

This long pulse results from the use of an LCR circuit with appropriate component values: L = 7.2 μH, C = 10,000 μF. The resistance R is comprised of the wiggler resistance (1.50 Ω + (approx. 10% for tuning resistor))/280 ≅ 5.9 mΩ, and the resistance of the inductor and busswork. The inductance of the wiggler is small, of order 0.3 μH.

Another restriction placing a lower limit on the current pulse duration is the frequency response of the permeability of the ferromagnetic cores. I observed a rolloff in the peak magnetic field produced per unit input peak current as the pulse duration was decreased (by reducing the bank capacitance). In terms of time-to-peak of an

underdamped half-sine waveform, the rolloff started just below 300 μsec, the value chosen for our operational waveform.

The pulser schematic is shown in Fig. 3-5. The pulser is triggered by an SCR. Note that the SCR and the diode act as a half-wave rectifier so that the wiggler is energized only by the half-sine pulse. The diode also serves to leave the capacitor bank (consisting of aluminum electrolytic capacitors) in a positive charge state after the shot, extending capacitor life and reducing the amount of charge that must be provided by the charging power supply to restore the bank voltage. The capacitor bank is charged to around 550 V during normal operation, by a Cynosure HVD-2000A capacitor-charging power supply capable of 600 V output. The resulting current pulses have a peak value of 12.5 kA and are generated at a rates of 1/2 Hz. Charging voltage stability is enhanced by the use of a 10 Ω resistance in the charging circuit.

3.3 Field measurements

This section describes the results of an extensive set of field measurements made during the process of tuning the Microwiggler. I have claimed that the MIT Microwiggler produces the world's most uniform periodic magnetic field with period less than 10 mm. The criterion of uniformity I employ is the RMS spread in the pole integrals* of the axial field profile [Bobbs *et. al.*, 1990]. Presenting a measurement of the peak amplitudes alone is inadequate to establish the uniformity of the pole integral profile. I must also demonstrate that the field periodicity errors are of the same order as the amplitude errors. Ideally, this would have been accomplished by making a densely-sampled measurement of the entire on-axis field profile, and computing from it the pole-integrals. Our measurement system, however, was capable of precisely measuring only the peak amplitude, and the

* The pole integral of a half-period is the area under its field profile curve. This can easily be shown to be proportional to the momentum imparted to an electron by it.

peak position, of each half-period. Therefore, the amplitude and position measurements are presented in lieu of direct pole integral measurements. There are additional precision issues to be resolved. The Microwiggler produces a pulsed magnetic field. The coils are connected in parallel (see Fig. 3-5), so that there is in principle the possibility that the fields generated by the various coils are not temporally synchronous, since their inductances may vary. Accordingly, I measured the magnetic field's time dependence as a function of axial position *z*.

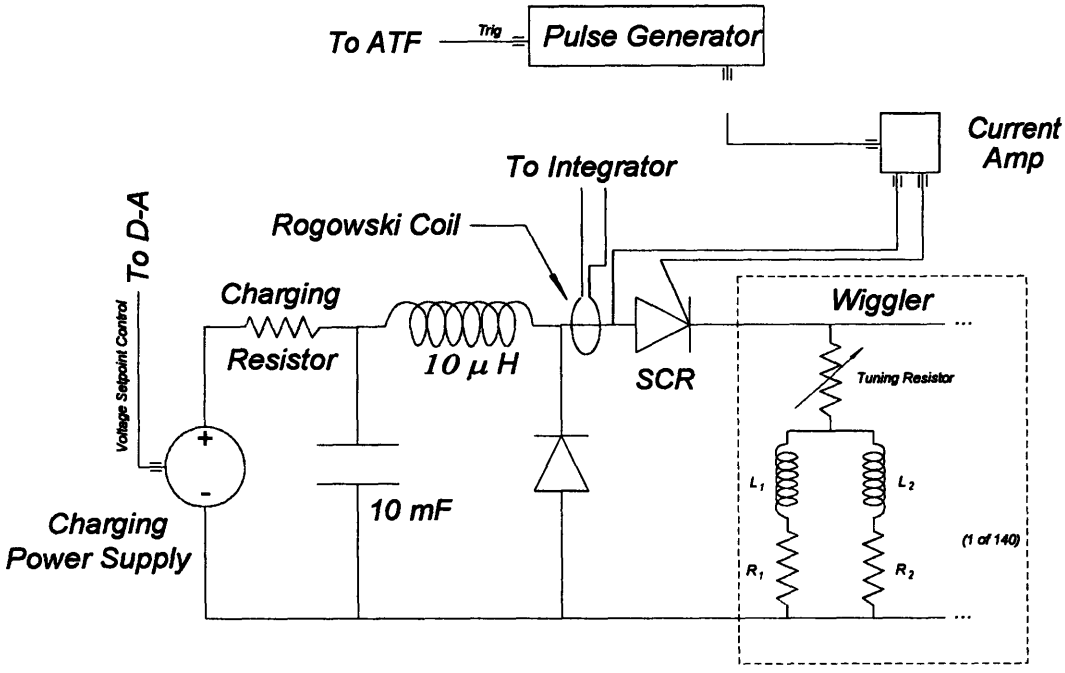

FIGURE 3-5. Schematic of the pulsed power supply for the MIT Microwiggler.

I remarked that I lacked the means to make a precise, densely-samped measurement of the entire field profile suitable for determining the pole integrals. However, I was able to make such a measurement with adequate precision to determine the field's harmonic content. The remaining precision question relates to the cross-gap symmetry of the field. Eqn. (1.9) shows that the ideal wiggler field varies as $\cosh(k_w y)$. The cross-gap minimum in the field amplitude of the ideal wiggler thus occurs at $y = 0$, for

all z. I performed position measurements of the cross-gap field minimum as a function of z, to ensure that the variations in the real wiggler field's cross-gap minimum position were of an acceptable magnitude.

The strength of the wiggler field must also be verified. Accordingly, I performed saturation measurements of the Microwiggler identical to those carried out on the prototype magnet of Ch. 2. (see Sec. 2.3).

The peak amplitude data are presented in Sec. 3.3.1. Sec. 3.3.2 describes the time dependence of the field profile. The spatial harmonic content of the profile is given in Sec. 3.3.3, and the saturation characteristic of the field is presented in Sec. 3.3.4. The cross-gap minimum measurements appear in Sec. 3.3.5, and the periodicity measurements are given in Sec. 3.3.6.

3.3.1 The peak amplitudes

Using the tunability of the Microwiggler, I have established a uniform-amplitude field profile in which the RMS spread of the peak amplitudes is 0.12%, the best of any sub-cm-period wiggler of which I am aware. Figure 3-6 shows the amplitude of each peak as a function of peak number, for both the tuned and untuned profile. The same vertical scale and range is used for comparison in both plots. In the tuned profile, all peaks lie within a range of ±0.3%. This is in sharp contrast to the untuned profile, in which the RMS spread in peak amplitudes is 4%. Tuning has thus reduced the field errors by a factor of 30.

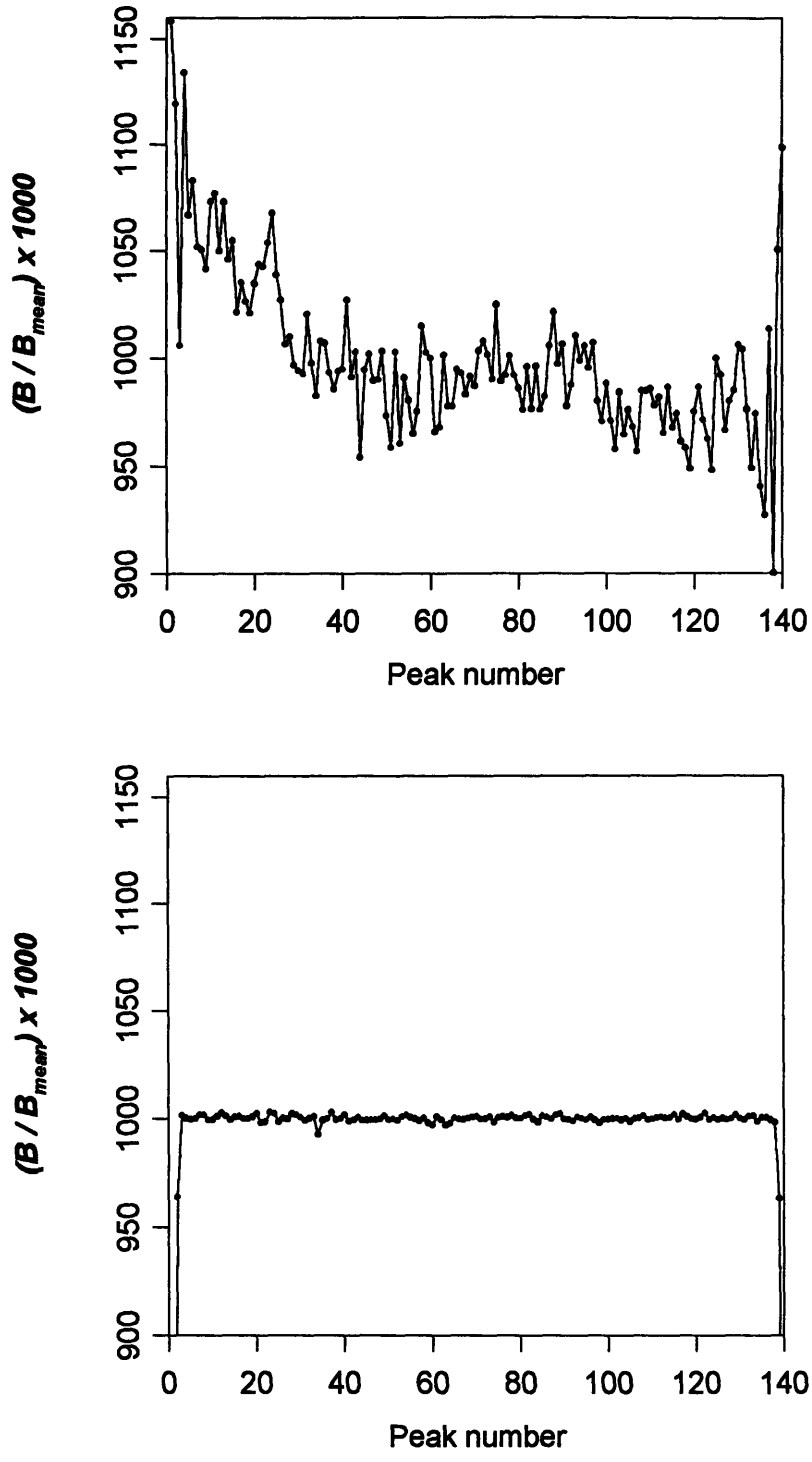

FIGURE 3-6. Untuned (upper plot) and tuned (lower plot) peak amplitude profiles of the Microwiggler. The ranges and scales of the two plots are identical; very clearly, tuning has greatly reduced peak amplitude variations. The tuned profile also shows the tapering of the end peaks. The largest amplitude error, -0.7%, occurs at peak #34; it is clearly discernable.

A 0.12% RMS spread in the peak amplitudes is very good. Nevertheless, it should be noted that an even smaller error was produced when operating the wiggler at a lower pulse repetition rate. The tuned profile of Fig. 3-6 was produced at a pulse repetition rate of 1/2 Hz. At 1/4 Hz, I was able to produce a flat-tuned (*i.e.*, no end-tapering) profile with an RMS spread in the peak amplitudes of 0.08%, at the same field amplitude. The increase in the field error with repetition rate results from the coils' increased resistance with temperature: though the ratios of the various coils' resistances remain the same, the absolute differences among them increase. The tuning resistances adjust out the absolute differences among the various coils' resistances, and of course only a finite range of adjustment is available. At 1/2 Hz repetition rate, I ran out of adjustment range on peak #34. Figure 3-6 shows it to have the largest difference from the mean value. If time had permitted, the coils of this half-period could have been replaced and lower RMS spreads in the peak amplitudes could have been produced even at the higher repetition rate. Section 3.4 discusses how a more comprehensive approach to reducing the underlying field errors in the untuned profile could result in a tuned, tapered, 1/2 Hz profile with an RMS spread of perhaps 0.05%.

3.3.2 Time dependence of the field profile

In measuring the field's peak amplitudes, it was assumed that the value of the field at a given axial position was given by the maximum value of the time-dependent field pulse. Insofar as the wiggler magnet half-periods producing the field peaks are connected in parallel, temporal "phase slip" will occur between the fields produced by different cross-gap coil pairs, *i.e.*, the temporal field peaks will occur at different times in different half-periods. This is because the inductances and resistances of the various half-periods are not identical. The field at a given instant of time is therefore less uniform than would be indicated by simply considering the maximum values of the time-dependent pulse. It has

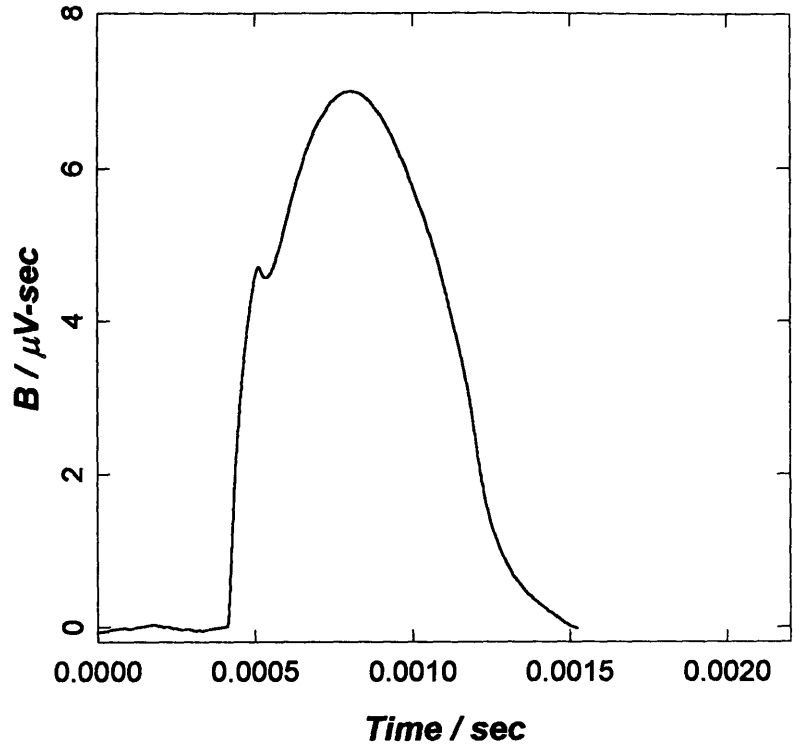

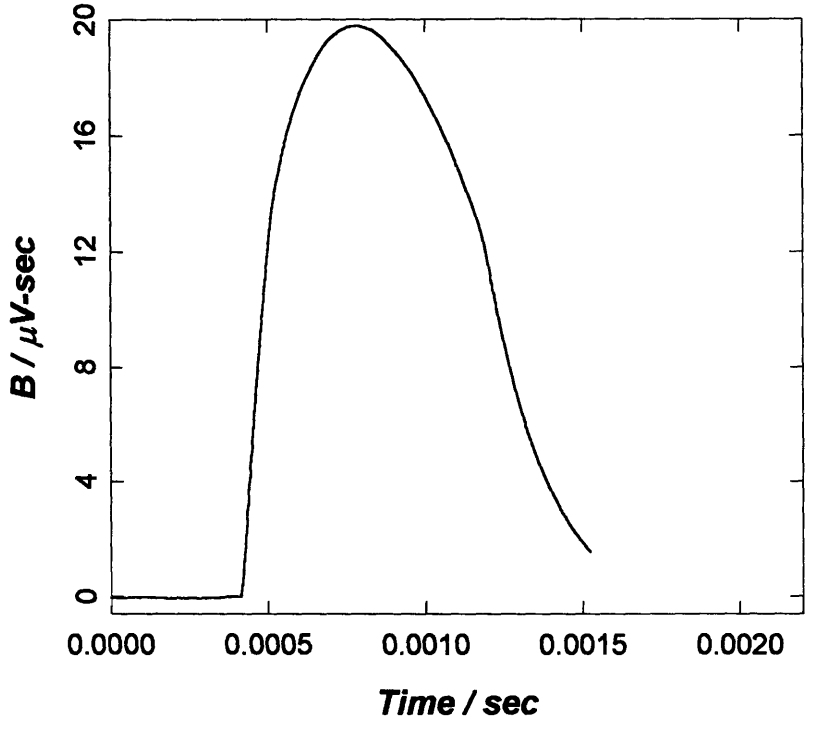

FIGURE 3-7. The magnetic field as a function of time measured at the end peak (top), and at a peak in the body in the wiggler (bottom). Note the "glitch" in the leading edge of the end peak's pulse; this is due to the onset of saturation in the magnet body (see text).

been determined, however, that phase slip between the various peaks adds negligibly to the overall field error. Figure 3-7 shows typical magnetic field pulses, measured at the end of the magnet, and in the body of the magnet. The variation near the peak value of the "magnet body" field pulse is

$$\left|\frac{B - B_{\max}}{B_{\max}}\right| = \alpha \cdot (t - t_{\max})^2 \qquad (3.1)$$

where $\alpha = 3.07 \times 10^6$ sec^{-2}. Figure 3-8 plots relative time-of-occurrence of field peaks as a function of peak number for samples of peaks near each end of the magnet. The data were obtained by measuring the relative times at which the magnetic field time derivative curves crossed through zero. Error bars are estimated from the standard deviation of the mean of a set of measurements applied to a representative peak. The estimated fractional error due to the phase slip in the central peaks of the wiggler (*i.e.*, excluding the end peaks) can therefore be estimated to be

$$\alpha \cdot (\Delta t_{rms})^2 \approx 5 \times 10^{-5}$$

which is nearly an order of magnitude less than the uncertainty in the measurements of the field peaks, and is thus negligible.

An additional concern is the time dependence of the wiggler field at the ends of the magnet. The field is tuned so that the pole integral of the end peaks is 1/2 that of the central peaks; this means that the end peaks' tuning resistors are much larger than those of the central peaks' tuning resistors. The total inductance of the end peaks is less than that of the magnet body since the end peaks have only one nearest neighbor, and so have less

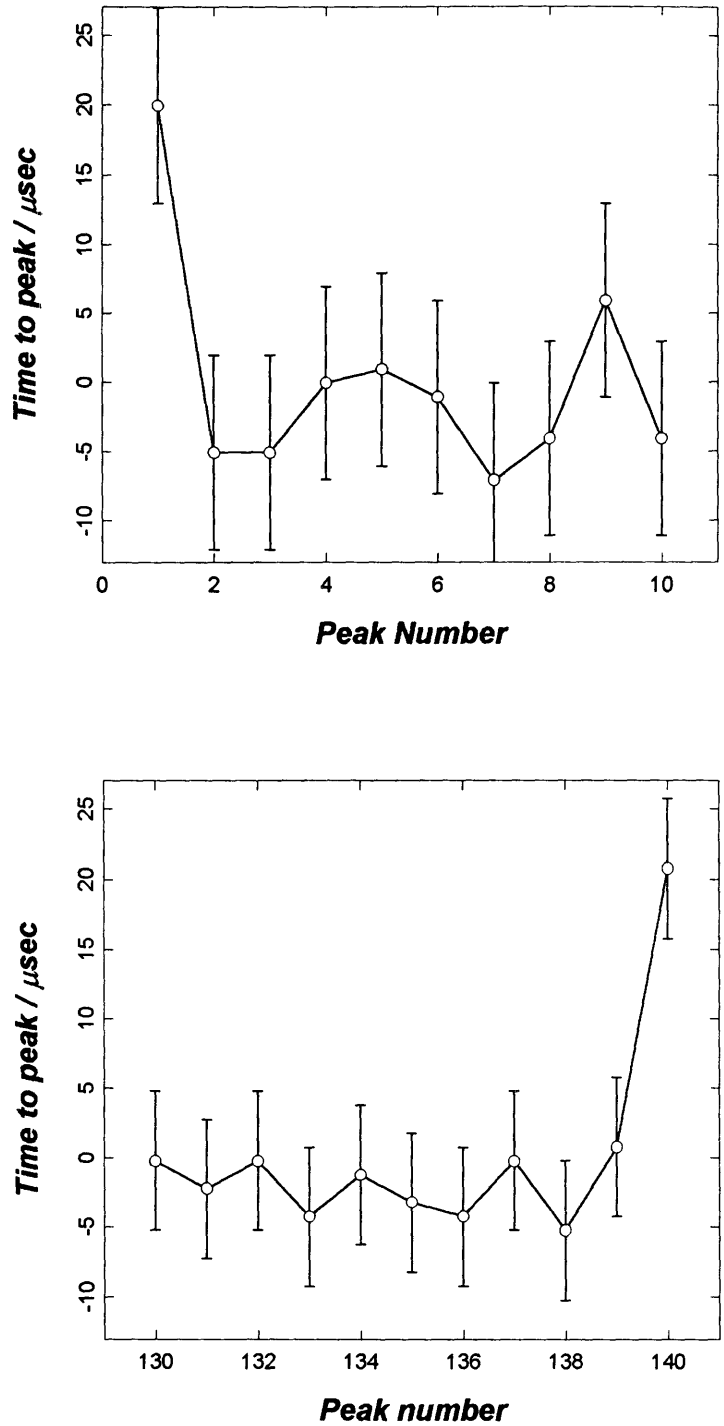

FIGURE 3-8. Time to peak of the magnetic field at half-periods at each end of the Microwiggler. The field at the end half-periods reaches a peak about 20 μsec later than the field at peaks in the magnet body. In both plots the measurements are connected by lines, to guide the eye.

mutual inductance than the central peaks. Therefore, the end peaks' *L/R* risetime is significantly reduced in comparison to that of the central peaks. Examination of Figures 3-7 and 3-8 indicates, however, that the time of occurrence of the end peaks is *later* than that of the central peaks, not earlier. In comparing the end peak magnetic field pulse to the magnet body pulse of Fig. 3-7, it is seen that the leading edge of the end peak's pulse is steeper than that of the central peak pulse, but that the end peak pulse briefly collapses prior to resuming its increase to the maximum. I believe that there is a simple explanation for this phenomenon: when the coils of the central peaks saturate, there is a sudden decrease in their inductive impedance which results in a suddenly increased current draw. Since the total impedance is mainly resistive, this inductance change does not cause a big swing in the total impedance, but it is enough to draw current away from the end peaks' coils to produce the "glitch" and the concomitant delay in their reaching their peak.*

3.3.3 The spatial harmonic content of the field profile

Figure 3-9 shows a typical portion of the measured on-axis profile of the Microwiggler, along with a Fourier transform power spectrum of the central 66 periods. The second and fourth harmonics are below the noise level; the third harmonic is down from the fundamental by a factor of about 2.3×10^{-5}. This is a very small value, which is advantageous for use in a short-wavelength FEL oscillator because, as previously mentioned, higher field harmonics cause very short-wavelength incoherent emission which can damage optical coatings of the resonator mirrors. The measured fifth harmonic is just above the noise level, at around 6×10^{-6}, which is also small. Note that this is a minimal-steering profile with tapered ends, implemented at a 1/2 Hz repetition rate for experimental operation.

---

* This hypothesis could be easily checked in a minute's operation of the Microwiggler. Unfortunately, I did not have access to the device at the time of this writing.

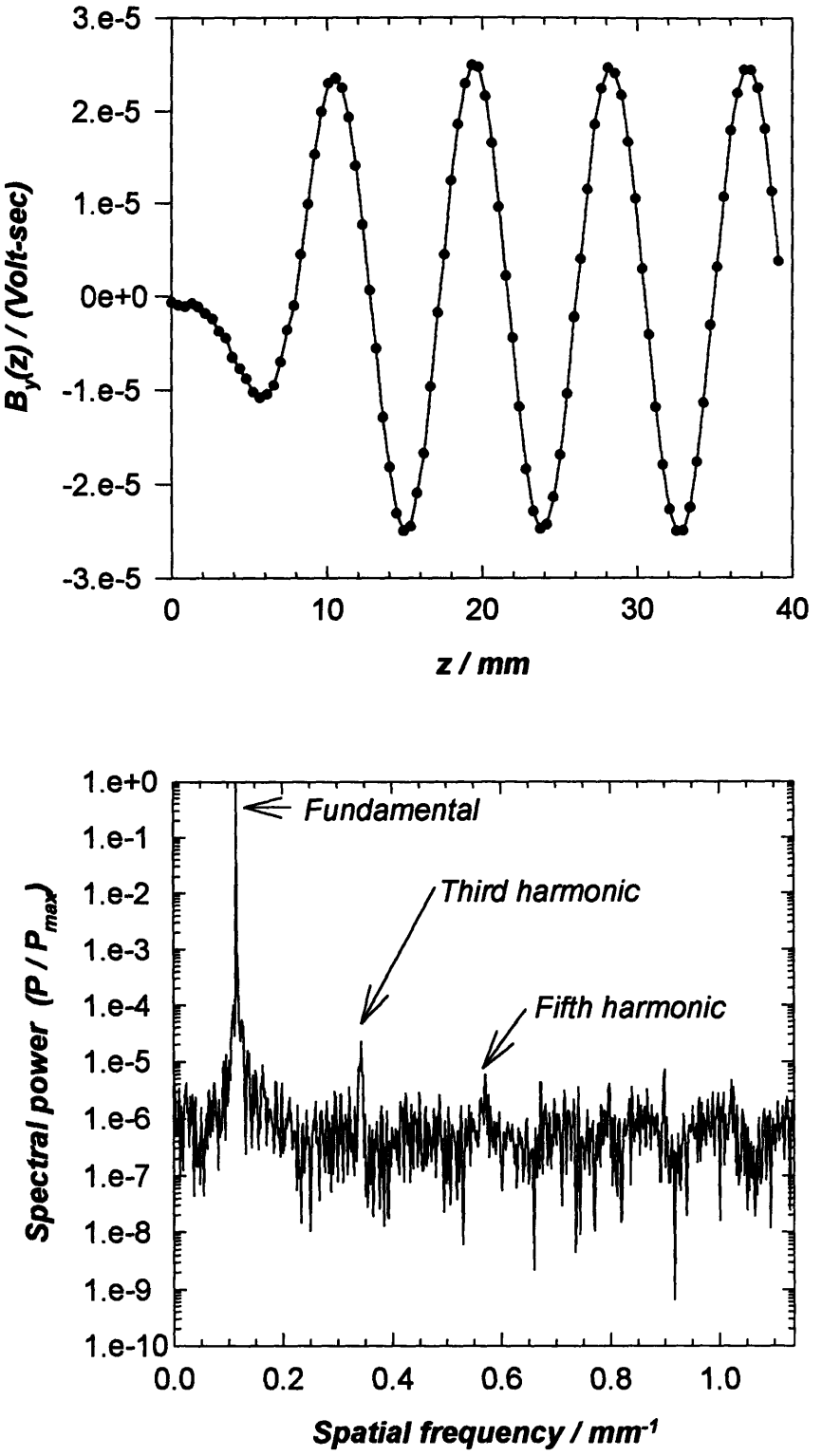

FIGURE 3-9. Detailed measurement of the axial field profile, and its Fourier transform power spectrum. The top plot is a portion of the profile measurements near the end of the magnet. The bottom plot is the power spectrum of the central 66 periods. The first, third, and fifth harmonics are indicated: harmonics beyond the fifth are obscured by noise.

The data were acquired in a fashion different from that of the peak amplitude measurements, in that the magnetic field signal traces were acquired directly from the pickup coil by a Tektronix 2731L oscilloscope, and then transferred to the control computer for storage. The computer moved the probe and saved scope traces, but would not do so until the operator indicated that the data on the scope was acceptable. In addition to accepting the data, the operator also was required to instruct the computer to reverse the polarity of the pickup coil connection as required to keep the pickup coil signal positive: this eliminates the introduction of a spurious constant offset into the measured field profile that would result from asymmetric response in the bipolar amplifiers, etc., of the oscilloscope.

Scope-to-computer data transfer rates, along with the required operator perusal and acceptance of each trace, resulted in several shots being taken at each position in the profile to acquire the measurement at that position. The magnetic field pickup probe is displaced significantly by the mechanical shock produced by firing the wiggler. Thus, measurement error was introduced by probe position variations during the acquisition of each datum. Noise generated by the firing pulser was also picked up. Measurement errors in these measurements are much larger than in those of the peak amplitude measurements; due to time constraints imposed by the ATF run schedule and extensive operator time required for these measurements, multiple data sets could not be acquired. Sisson (an undergraduate collaborator) has calculated the mean value and RMS spread in the pole integrals (*i.e.*, the area under the profile curve of each half-period) [Sisson, 1994]. I believe that the very large RMS spread in the measured values of the pole integrals, 2.5%, is thus due primarily to measurement errors, since the periodicity (Sec. 3.3.6) and amplitude measurements (Sec. 3.3.1) are not consistent with such a large spread in the pole integrals.

3.3.4 *B vs. I* and absolute calibration of the field strength

The measured magnetic field vs. current profile of the Microwiggler is depicted in Fig. 3-10. This curve was used to select the value of the operating peak field (>4.0 kG). These measurements were made with long (16 msec) current pulses injected into a 20-period subsection, which permitted the use of a Hall probe gaussmeter. The wiggler gap was 4.4 mm when these measurements were made. It subsequently became possible to reduce the gap to 4.2 mm, to boost the wiggler field. As shown in Ch. 1, the fundamental component of the wiggler field depends on the wiggler gap G as

$$B \propto e^{-\frac{\pi}{\lambda_w} G}$$

when G is a substantial fraction of the wiggler period λ_w. I estimate that the fields for a given current are about 4-6% larger with the present smaller gap than the measurements of Fig. 3-10.

I believe the operating peak on-axis wiggler field amplitude is >4.0 kG. We have directly measured the total current delivered to the wiggler by measuring the voltage drop across a segment of the buss bar current feed and found it to be (12.5 ± 0.6) kA. This is about 44 A per coil; the saturation curve of Fig. 3-11 then yields the conservative estimate of 4 kG. We can also estimate the peak field via the integrated ($\dot{B}$) pickup coil signal, which was constructed to permit such use. When the *y*-direction (cosh) variation of the field is considered, an axial peak in *z* of the wiggler field is actually a saddle point in the *y*-*z* plane. Our probe is of square cross-section in the *y*-*z* plane and measures the average field over the cross-section: at an on-axis peak, the increase in the field away from gap center is compensated by the decrease in the field in the axial direction. The pickup coil voltage then corresponds with good accuracy to the peak wiggler field at gap center. The

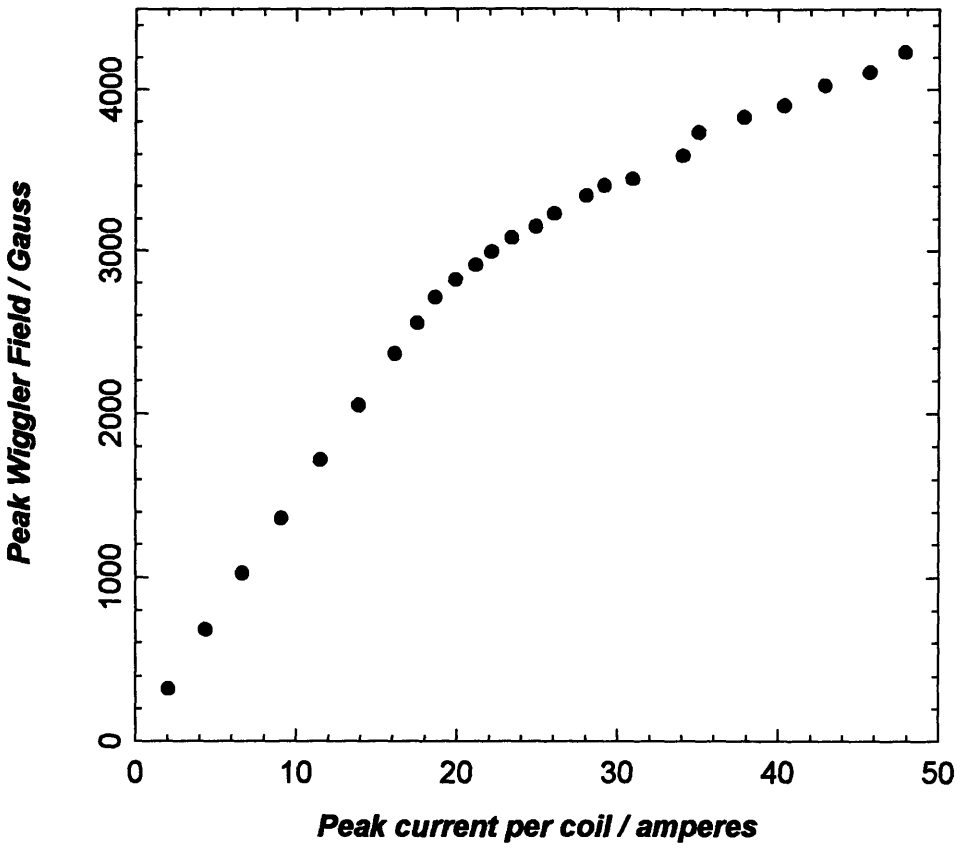

FIGURE 3-10. Microwiggler field as a function of input current. These measurements were obtained with a Hall probe gaussmeter with the wiggler gap G = 4.4 mm. The gap was subsequently reduced to 4.2 mm to increase the field strength: the field at the operating current of 45 amperes per coil is now about 4.3 kG.

result is (4.5 ± 0.3) kG, again > 4 kG.

3.3.5 Magnetic center measurements

As earlier mentioned, in order to justify my claim of high field precision it must be shown that, in addition to producing a measured profile with very small amplitude errors, there are no significant irregularities in the cross-gap field dependence. It was impossible to perform *y*-direction (cross-gap) field profile measurements as performed on the prototype (see Fig. 2-7), because the ($\dot{B}$) pickup coil probe holder was fitted snugly into the drift tube bore and thus could not be moved across the gap. In lieu of such

measurements, I devised a technique for measuring the y-position of the center (cross-gap minimum) of the magnetic field as a function of axial position, by use of an axial probe. The axial probe's pickup coil was oriented to sense fields parallel to the z-axis; thus, in an ideal magnet with this coil perfectly centered on the z-axis, no signal would ever be detected. In the real magnet, however, the magnetic field center and the pickup coil center do not exactly coincide, so that the axial field component of the wiggler field will be sensed by the pickup coil. The signal will be directly proportional to the separation between the pickup coil center and the magnetic center. To obtain maximum signal, the probe was positioned near nulls of the B_y magnetic field component; according to Eqn. (1.9), the axial component B_z is a maximum at those points. Measurements were taken at each of the 139 transverse field component nulls. I present in Fig. 3-11 the results of an analysis of the data carried out by Sisson [Sisson, 1994]: the figure shows plots of the analyzed data and its Fourier transform. Fourier components at spatial frequencies of zero and $1/\lambda_w$ were removed from this data, since they are due to either a constant offset of the coil from the mean magnetic center, or a spurious pickup due to the coil being slightly tilted and thus sensing some magnetic field component B_y. The mean noise level in the data is not known since time permitted the acquisition of only one datum at each point, but it is significant, and is estimated to be between one and several tens of percent of the RMS signal value. There is an interesting correlation indicating the validity of the axial probe measurements; the magnetic center displacement curve of Fig. 3-11 shows the largest displacement at peak #34, the same peak having the largest field amplitude error (see Fig. 3-6).

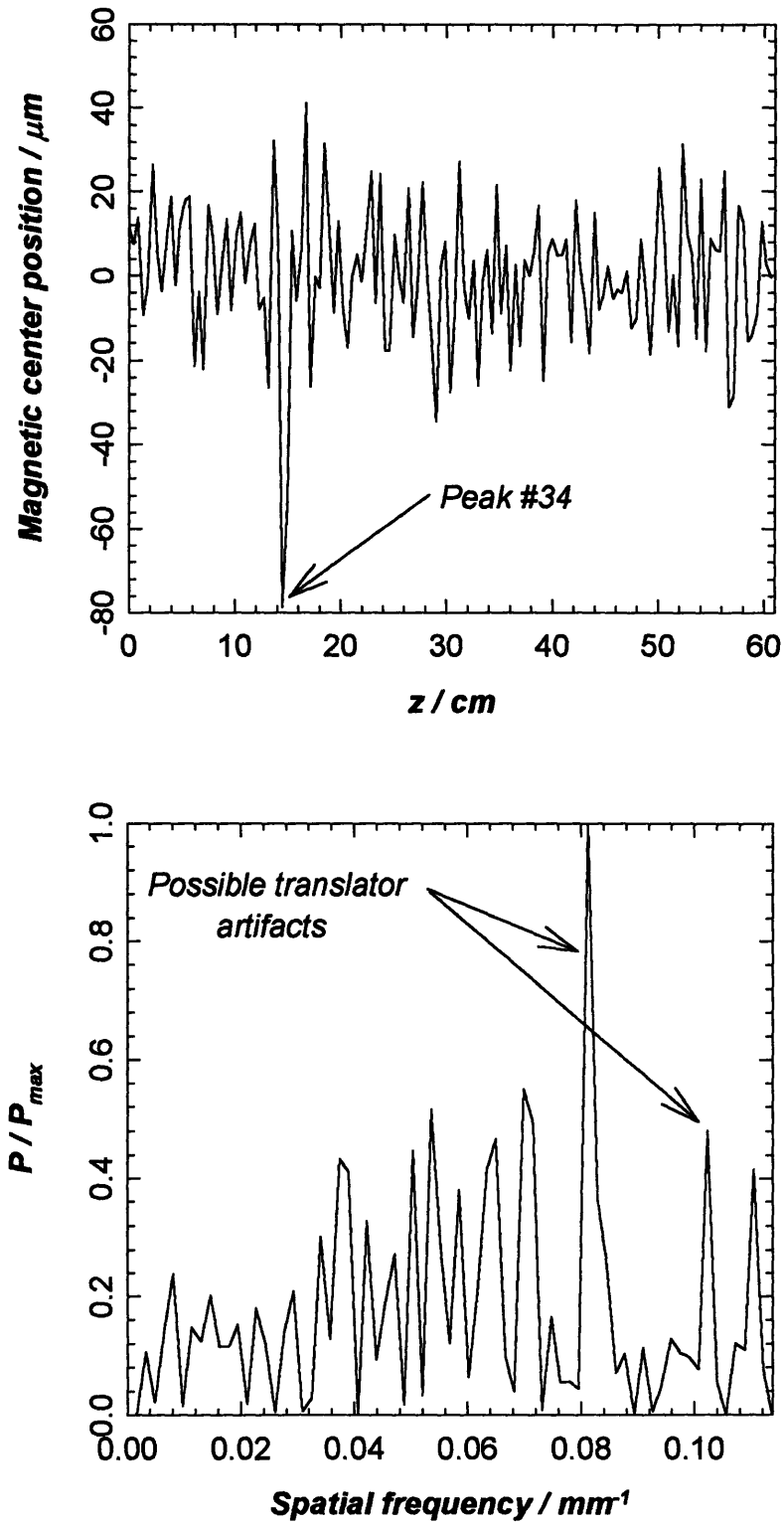

FIGURE 3-11. The position of the wiggler magnetic field *y*-minimum (magnetic center) as a function of axial position *z* (top plot), and the Fourier power spectrum of the magnetic center position profile. I suspect two peaks in the power spectrum to be due to translator error, they are indicated in the bottom plot.

The signal data of Fig. 3-11 are expressed as relative displacements of the pickup coil center from the magnetic center, in microns. The conversion from laboratory units was made according to

$$\delta y(z) = \frac{B_z(z)/B_w}{k_w}. \tag{3.2}$$

This relation follows directly from Eqn. (1.9), in the limit of $y << \lambda_w$, where I write the amplitude factor of the fundamental component as B_w. We know the value of B_w in laboratory units from the measurements of the transverse field component. We have

$$\delta y(z) = \frac{1}{k_w} \cdot \left(\frac{(V_{\text{axial}}(z)/A_{\text{axial}})}{(V_{\text{max,transverse}}/A_{\text{transverse}})} \right), \tag{3.2}$$

where V denotes voltages acquired by the axial probe or the transverse probe, and A denotes probe coil areas. That is, the maximum pickup coil voltage sensed during measurements of the *transverse* field component was used as normalization for the *axial* field component probe voltages (with a correction for the fact that the two pickup coils had slightly different cross-sectional areas).

The axial probe measurements show an RMS deviation of the magnetic field center from the pickup coil center of less than 17 microns. This value is conservative, in that it includes contributions of Fourier peaks which are possibly due to translator error (see the Fourier transform plot of Fig. 3-11). The field amplitude RMS variation due to this magnetic center position variation, along the pickup coil center's axis of travel, is of order

$$\delta B_{y,\text{RMS}} \approx B_w \cdot \left(\frac{1}{2} (k_w \delta y_{\text{RMS}})^2 \right) < 1 \times 10^{-4} \cdot B_w \tag{3.3}$$

which is a negligibly small amount in comparison to the measured RMS spread in the peak amplitudes of 0.12%. Thus, the magnetic center position variation need not be considered in the tuning of the transverse field amplitude. It should be emphasized that what was measured are the differences in position between the magnetic center and the axis of the magnet bore. There is no way to know from these data whether the bore axis is straight or not, though the use of strong, precisely-machined 1 1/2"-thick aluminum stiffener elements to enforce straightness of the magnet holders offers reassurance that the holders are straight to a precision of tens of microns or better. Moreover, the distances of each of the 280 polefaces from a reference plane (the flat backs of the holders) were measured to a precision of ±3 μm. These measurements determined the area into which the drift tube is confined. Its position is fixed to within about 10 μm in the *y*-direction. Thus, enforcing straightness of the magnet holders assures a straight drift tube bore: the data of Fig. 3-11 then show that there is no systematic bend in the line of the magnetic center. There are no cross-gap field irregularities of note.

3.3.6 Field profile periodicity measurements

Of very great importance is the extent to which the magnetic field is accurately periodic. As earlier remarked, there is no benefit in having very uniform peak amplitudes if there are larger-scale errors in the periodicity, because the amplitude and the period are equally important in determining the momentum kick imparted to a passing electron in a given half-period (which is proportional to the pole-integral). In principle, the spatial harmonic content of the field profile (see Sec. 3.3.3) contains the necessary periodicity information. However, the high noise content of my spatial harmonic data makes them an unreliable measure of the field periodicity. Correspondingly, an additional measurement of the periodicity was made: the locations, as well as the amplitudes, of the peaks were also obtained while taking the field amplitude profile measurements of Fig. 3-6. Fig. 3-12

shows a plot of the position of each peak, as a function of the peak number. The linear part of the position dependence is subtracted out. Thus, what is shown are the differences in position of the peaks from their ideal, precisely equidistant, positions. Figure 3-12 also shows the Fourier transform of these peak position differences. It is interesting to note that the slope determined from the least squares linear fit of the position data is just the average half-period of the magnet, and thus the magnet's period is found to be 8.78583 ± 0.00005 mm. In light of the alarmingly small RMS variance in the slope, I hasten to add that the accuracy of this value depends on the accuracy of the drive screw rotation-to-distance calibration, which is only good to about a part in 1000. We can check the accuracy of the period measurement by comparing it to that determined from the positions of the slots in the holders. The manufacturers provided such data, and the period obtained from that data is 8.7916 ± 0.0004 mm. The results do indeed agree within acceptable bounds; the latter result derives from a system with better absolute calibration, and is therefore more reliable, in spite of the fact that the former result is obtained from a direct measurement of the field.

I now compute the mean periodicity error from the position data. Some of the measured position error is due to small but discernable translator drive nonlinearities. Figure 3-12 indicates three peaks in the position spectrum that correspond to the first, third, and fifth harmonics of the translator drive screw rotation frequency of 0.7871 mm^{-1}. They appear in reverse order, and at the indicated low spatial frequency, because they have been aliased due to undersampling. The shaft rotation of the translator drive screw inevitably introduces some nonuniformity in translation; in any case, the translator artifacts can be subtracted out of the position error spectrum since they do not result from properties of the magnetic field. Upon subtracting out the contribution of the translator

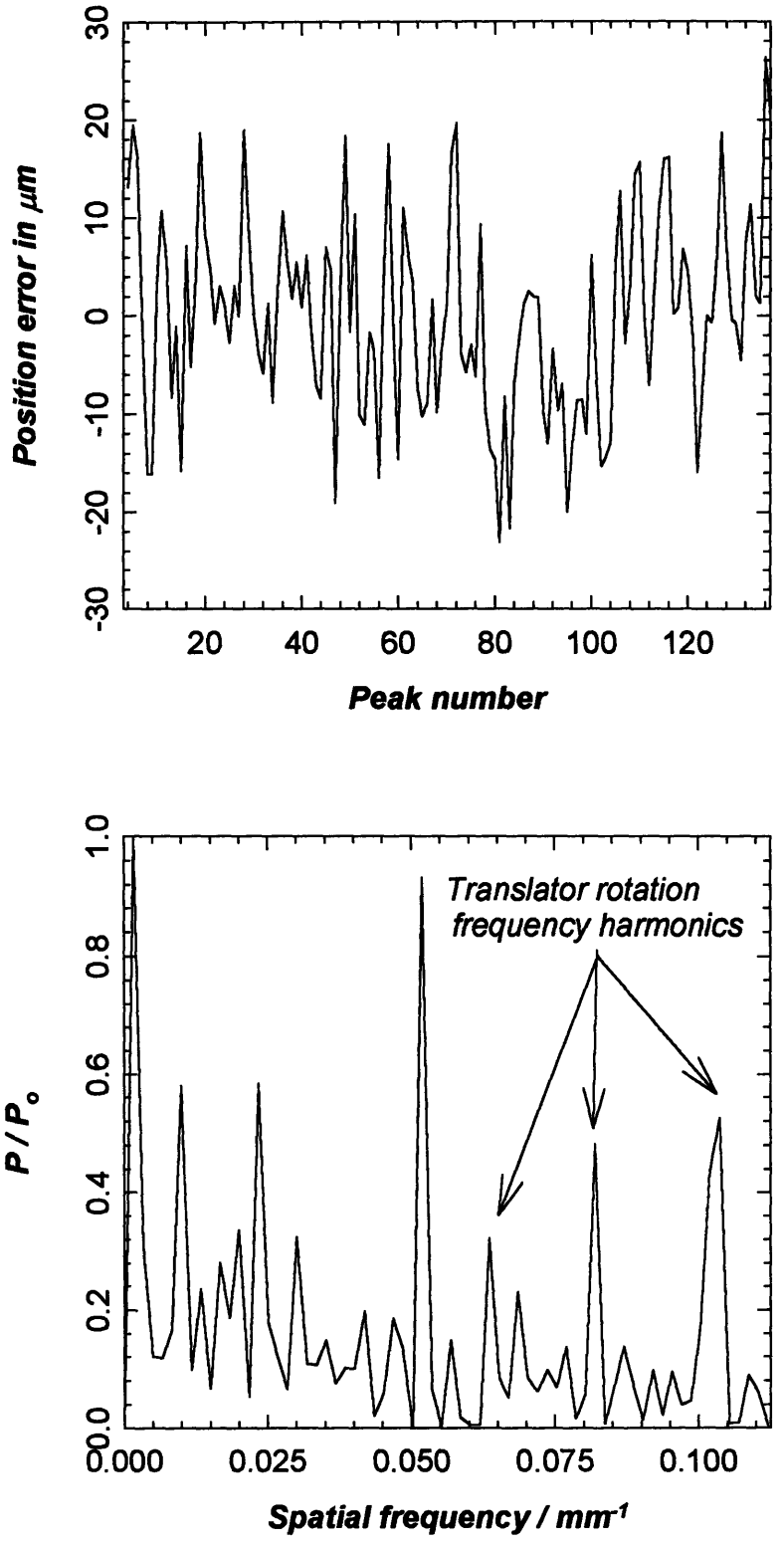

FIGURE 3-12. The measured positions of the peaks, with respect to their ideal, equidistant separations. The Fourier transform power spectral peaks indicated in the bottom plot are peaks due to translator error.

drive errors and the measurement uncertainty, I report an RMS deviation of the peak positions from their ideal positions of 9 μm. This is about 0.1% of the wiggler period, and is therefore of a comparable magnitude to the RMS spread in the peak amplitudes of 0.12%. Thus, the spread in the pole-integral values, though not yet measured directly, must be of the same order as the spread in the peak amplitudes.

3.4 Measurement, control, and tuning

To attain a precision of 0.12% in the RMS spread of the field peak amplitudes, a very large number of measurements must be made to reduce measurement error. A systematic approach to adjusting the 140 tuning resistors must be applied. The current energizing the wiggler must be constantly monitored and adjusted. Manual control by a human operator is impractical; consequently, I have developed a computer-based system for performing field measurements, monitoring and regulating the Microwiggler's operation, and computing resistor adjustments based on field measurement results. Figure 3-13 shows a schematic of the measurement and control system. ($\dot{B}$) pickup coils sense the wiggler magnetic field as well as that surrounding the high current buss. The magnetic field pickup coil is of extent 1mm x 1mm x 5mm in the axial (z), cross-gap (y) and transverse (x) directions, respectively, and consists of 8 turns of 32 AWG Formex copper wire wound in two layers on a rectangular G-10 core. The current pickup coil is in the Rogowski configuration. The signals are integrated using analog electronics and the integrated signals are digitized by a PC-based A/D board (with the exception of the harmonic content and magnetic center measurements, as noted in Sec. 3.3 above). The analog integrator circuits must be well-isolated from interference produced by the pulser. I chose this approach in favor of a Hall probe since the available Hall probe system lacked the bandwith to accurately capture the magnetic field pulse; also, use of a DC measurement scheme in an attempt to overcome the bandwidth problem was impractical

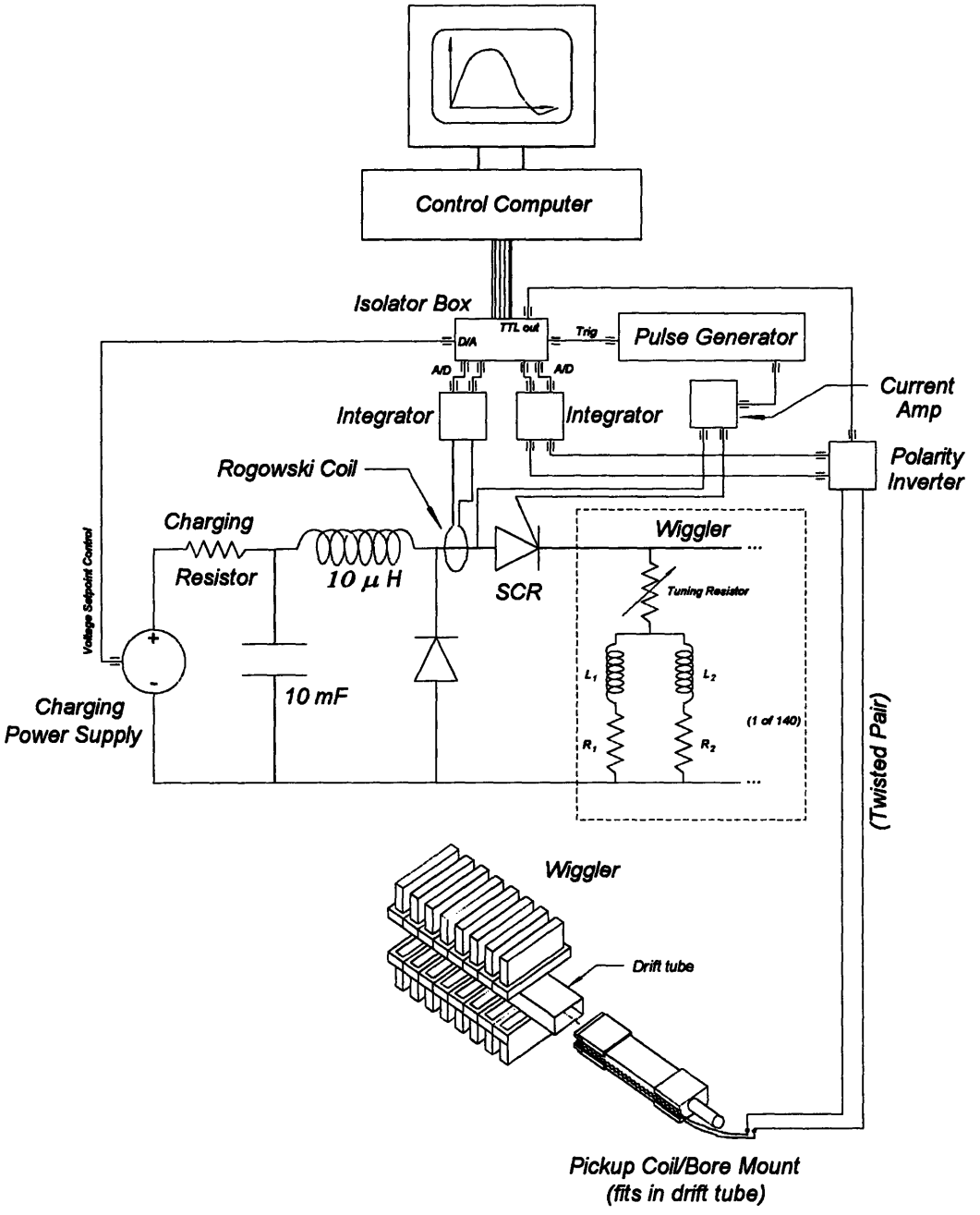

FIGURE 3-13. Microwiggler control system schematic. The control computer regulates the voltage of the charging power supply based on current measurements extracted from the Rogowski coil via the integrator and A-D converter. The computer controls the motion of the probe during field measurements, and saves to disk measurements of the magnetic field profile and peak current.

since the magnet operates in the saturated regime of the ferromagnetic cores (requiring very high current to reach). The computer then extracts the peak values of the integrated wiggler field and current pulses and records them in memory, periodically writing accumulated sets of shot data to disk.

The current regulation is based on a simple feedback algorithm. The computer averages the peak value of an operator-specified number of current shots and compares the result to a setpoint value. If a correction is required, the charging power supply's voltage is adjusted according to the following algorithm:

$$\Delta V = G \cdot (I_{set} - I_{measured}) \tag{3.4}$$

where ΔV is the voltage adjustment to be applied, G is the gain, I_{set} is the desired setpoint current, and $I_{measured}$ is the measured average current. The gain must not be set too high or oscillation will result.

It should be emphasized that current stabilization is absolutely necessary for attaining a steady magnetic field amplitude. In the absence of active control, capacitor conditioning effects lead to current amplitude drifts of several percent over the course of a day's run; a drift of such magnitude is intolerable. The computer-controlled current stabilization eliminates the long-term drift, and results in an RMS spread in the current peaks over a day's run ($>2 \times 10^4$ shots) of less than 0.1%. Since the magnet operates in the saturated regime, this means that the shot-to-shot jitter and the long-term drift in the magnetic field amplitude combine to less than 0.03%, an acceptable value. The resulting jitter/drift in the center frequency of the radiation wavelength is then (*c.f.*, Eqn. 1-6) of order 0.003%.

The tuning regimen views the magnetic field profile as a 140-component vector, the components of which are the amplitudes of the 140 field peaks. A stepper-motor-driven translator pulls the ($\dot{B}$) pickup coil through the wiggler drift tube; a Delrin holder fitted to the drift tube supports the pickup coil, and attaches to the translator via a length of stainless steel tubing. The pickup coil leads are brought out of the wiggler through the stainless steel tubing in twisted pair configuration. Grounded-shielded twisted-pair cable brings the signal to the analog integrator.

The magnetic field peaks are measured in sequence, with no changes in the probe's direction of motion (a single direction of motion must be maintained in order to avoid flexing of the probe shaft). The probe moves in steps of 0.25 mm; 5-7 data points are taken in the vicinity of each peak, rather than stepping through the entire field profile. Upon sensing a change in the spatial derivative of the field (as a function of axial position), the computer recognizes that a peak has been found. It moves the probe one more step, takes one more datum and moves the probe several millimeters to the vicinity just before the next peak: the polarity of the ($\dot{B}$) pickup coil probe connections are then reversed (via a relay network) so that the sign of the electronic pulse presented to the analog integrator remains unchanged as the polarity of the field changes. The polarity reversal also ensures that the two channels of the A-D converter (acquiring the current and magnetic field signals) are presented with signals of a limited range of magnitudes: this is necessary because there is crosstalk of order 1% between the channels.

After getting data for a peak, the program performs a least-squares fit to a parabola to extract the peak value (a parabola is used because it is an adequate model to which the data can be rapidly fit); the result is recorded in memory. Note that only one shot can be taken at a given probe position since the probe is jarred by the firing of the magnet and moves slightly, enough to add sufficient error to the subsequent shot

measurements that nothing is gained from averaging. Of course, some averaging is provided by the parabolic fit, but not enough to provide sufficient measurement precision for our purposes. I therefore repeat the sequence of 140 peak measurements- typically 5-6 times- and average the results. Since each sequence of 140 measurements provides an independent measurement of each peak, I also compute the standard deviation in the mean of the measurements to obtain an estimate of the statistical uncertainty in the measurement of each peak. The typical uncertainty is 0.035%. Each measurement session to produce average values and uncertainties for the 140 peaks requires the simultaneous measurement of field and current during ~5000 shots, and the accurate recording and analysis of the resulting data-- a fact that underscores the need for an automated system, and justifies the effort required to write 10^4 lines of Pascal code to implement it.

Systematic errors must also be controlled. Extreme care was taken in the construction of the pickup coil probes in order to avoid spurious pickup by the leads coming out of the magnet bore. The pickup coil and the leads were formed of a single piece of 32 AWG Formex wire. This was necessary because the use of solder junctions to attach the pickup coil to the output leads resulted in an inadvertent extra pickup loop which acquired significant spurious signal. The output leads were brought out in a twisted-pair configuration of 1200 turns placed on the 60-cm leads; longer pitches in the twist were found to result in undesired pickup from the leads. Moreover, the twisted pair ($\dot{B}$) signal cable (from wiggler to integration electronics/computer) had to be carefully routed away from the pulser to eliminate a false indicated dipole field component. Care was also taken to avoid creating an inadvertent pickup loop at the signal cable-pickup probe leads junction, which when made too large could sense the stray fields from the pulsed power supply.

The fitting of the pickup coil holder into the bore also had to be carefully done. The final dimensions were reached by hand application of fine emery cloth to the Delrin holders. Changes of 2 μm in the height/thickness (as measured by micrometer calipers) of the holders produced discernable changes in the holder's fit into the bore. A slight resistance fit was ultimately obtained, which was quite uniform over the range of travel of the probe.

Having precisely measured the field profile, it remains to apply corrections to reduce the errors. This requires advance determination of a reasonable "target" field profile, and careful characterization of the effects of making adjustments to the tuning resistors. Determining an experimentally useful target profile is not trivial: since the field peaks change shape at the ends of the wiggler, one must relate the measured peak amplitude to the total integral of the field in the end peaks. In doing so, it is necessary to account for the fact that the ($\dot{B}$) pickup probe has both axial and transverse extent, and so the measured field at a given point is really the value averaged over the extent of the probe. I took the approach of tuning a "virtual wiggler" in the POISSON codes, using a target profile in which the integrals of the first and last half-periods (taken on axis) of the wiggler were taken to be 1/2 that of half-periods in the body of the magnet (the techniques used in the virtual wiggler tuning were identical to those outlined below for the actual magnet). This profile produces zero net steering of an on-axis electron beam. I then calculated what profile our pickup probe would measure from the virtual wiggler's field by computing averages over the pickup coil extent for a dense sample of coil positions. This profile was then analyzed to compute the amplitudes of the peaks that would be measured from a zero-steering wiggler field. I found that the first two peaks' measured amplitudes must be reduced in comparison to those of the body of the wiggler, in the ratio 0.37 : 0.88: 1.00 (with uncertainties of at least several percent).

Having found a target tuning profile, the effects of tuning resistor adjustment must be systematically probed. The known set of necessary field amplitude changes must be translated into a set of resistor adjustments via a matrix whose components are defined by

$$(\frac{\partial B_i}{\partial R_j}) = \{\text{change in } i^{th} \text{ peak amplitude due to change in } j^{th} \text{resistor}\} \qquad (3.5)$$

This is a (140 x 140)-component matrix; all of its components are measurable in principle, but in practice a judiciously chosen subset is selected. I measured a (11 x 11) matrix using the first eleven peaks of the wiggler, in order to capture the ends' behavior while proceeding far enough into the wiggler bulk to accurately characterize it. The measured matrix is then extended to full dimension by assuming symmetry about wiggler center and neglecting effects of resistor adjustments more than 3 peaks away from a given resistor. A change in the field profile vector ($\Delta\vec{B}$) is then produced by a resistance adjustment vector ($\Delta\vec{R}$) according to the matrix equation

$$\Delta\vec{B} = \frac{\partial\vec{B}}{\partial\vec{R}} \cdot \Delta\vec{R} \qquad (3.6)$$

where the desired ($\Delta\vec{R}$) can be computed from the measured ($\Delta\vec{B}$) field differences from the target profile and the measured ($\partial\vec{B} / \partial\vec{R}$) response matrix. This procedure amounts to a Taylor expansion to linear order of the magnetic field amplitude profile vector as a function of the tuning resistor values, about the initial value of the field amplitude profile vector (typical tuning resistances are roughly 5-10% of the coil resistances). Of course, our use of ferrocore electromagnets in the saturated regime ensures that, for sufficiently large changes in the tuning resistors, nonlinear variations in the field will be produced. Nevertheless, iterative application of the procedure converged to the measurement precision limit for the profiles we have tuned (constant-amplitude and reduced-steering end-tapered).

While several iterations of the tuning process were required, convergence to the measurement precision limit is rapid. Only 3 iterations were required in the flat profile case to reduce the RMS spread in the peak amplitudes from the untuned value of 4% to a value of 0.12%.

3.5 A proposal for directly measuring the field's first spatial integral

It was mentioned previously that measuring and adjusting the pole-integral profile would be preferable to the present approach of measuring and adjusting the peak amplitude profile (Sec. 3.3.6). When the periodicity errors are small in comparison to the wiggler period as with the present device, the peak amplitude profile is an acceptable measure of field purity. However, possible future microwigglers might be constructed with shorter periods than the present device. Periodicity errors would inevitably become fractionally larger with reduced period, to the point that they would be larger than attainable field amplitude errors.

Measurement of the first spatial integral of the field profile could be simply done using a special pickup coil probe. The pickup coil would have the same extent in the x and y directions (see Sec. 3.4) as the existing magnetic field-sensing pickup coil, but would have greatly increased extent in the z-direction- longer than the length of the entire wiggler field. This coil would then sense the total first integral of the field, as a function of position:

$$V_{coil}(z) = \int_0^z dz' B(z'). \tag{3.7}$$

This first integral profile would consist of sinusoidal wiggles, just as the non-integrated profile; the field measurement system could be easily programmed to measure the peak

amplitude profile of the first integral. The difference in value between adjacent peaks in this integral profile is proportional to the corresponding pole integral of the field peak at that location. Thus, very high-precision measurements of the pole integral profile could be produced with the existing field measurement system.

3.6 Conclusions

A tunable electromagnet wiggler was used in the first free electron laser [Phillips, 1961], so that wiggler tunability is by no means a new concept. However, mine is the first device of which I am aware in which many tens of degrees of freedom have been systematically and efficiently exploited. In only a handful of iterations, my novel tuning algorithm produced a uniform-amplitude field profile (with end-tapering) with an RMS spread in the peak amplitudes of 0.12%, the most precise sub-cm-period wiggler field to date. Table 3-1 compares the MIT Microwiggler with other recently-reported short-period wigglers. An important figure of merit not listed in Table 3-1 is cost. While detailed information was not available, I can state with reasonable certainty that the other devices shown are 5-20 times more expensive than the MIT Microwiggler. The total expense of the Microwiggler's materials and equipment was of order $30,000, and the labor cost was about $70,000. The cost of equipment and materials alone for the other devices greatly exceeds this figure. However, it must also be noted that the Microwiggler produces pulsed fields with a modest repetition rate (1/2 pulse per second), and the other devices produce DC fields. For applications requiring a high duty cycle, such as a FEL-based user facility providing, e.g., UV radiation [Ben-zvi et al., 1990 (ii)], the additional cost is justified. This suggests that the MIT Microwiggler design is best suited for either a single-user radiation source, or for FEL research.

Reduction in the RMS spread of the *pole integrals* to the 0.05% level is readily achievable in our device. This would be comparable to the world's most uniform periodic magnetic field, but at 1/3 the wiggler period- a formidible achievement. An improvement in the uniformity of the untuned profile would be required in order to reduce the magnitude of certain of the tuning resistances, but such an improvement could be made using a technique employed in samarium cobalt wigglers [Cover *et. al.*, 1990]: the individual electromagnet coils could each be tested and sorted according to their field strength produced by a standard input current. Coils with field strength outside a specified range could be re-wound. The coils would then be re-installed in order of increasing or decreasing strength, according to whether or not a particular order would be preferred to

Table 3-1: Comparison of some short-period wigglers

GROUP	TECHNOLOGY AND STATUS	#PER.	λ_w/mm G/mm	B_w/kG	PEAK RMS ERROR	POLE INT. ERROR
Stoner *et. al.* MIT	Pulsed ferrocore electromagnet; operational	70	8.8/4.2	4.2	0.12%	0.18%
Huang *et. al.* Stanford	Staggered ferro-core array in solenoid; test	50	10.0/2.0	10.8	1.2%	Not reported
Warren and Fortgang LANL	Permanent magnet; operational	73	13.6/1.5	6.5	0.3%	Not reported
Tecimer and Elias CREOL	Hybrid; test	62	8/Not reported	1.0	0.2%	0.6%
Ben-zvi *et. al.* BNL	Superconducting ferrocore electro-magnet; test	20	8.8/4.4	>5.5	0.29%	0.36%

implement a possible field tapering scheme. In this fashion, random error is transformed into systematic variation and the total spread in the peak fields' values is reduced. Converting to the total field integral measurement scheme of Sec. 3.5 would enable measurement of the pole integral profile to the necessary precision and accuracy to attain 0.05% RMS pole integral spread: as already mentioned, I currently achieve measurement precision of 0.035% for the peak amplitudes.

With considerable effort and expense, pole integral errors of order 0.02% might well be achievable. Significant and laborious improvements to the measurement system would have to be made, in addition to the coil reordering scheme outlined above: the wiggler tuning wires and analog integrator electronics would have to be temperature-stabilized, and an improved temperature-compensated A-D converter board would be required; smaller-gauge wire would need to be attached to the tuning resistor wires to reduce the minimum practical adjustment; a better bore mount for the pickup coil would be required in order to improve the pickup coil's positional reproducibility; a new and more stable capacitor bank and charging power supply would be required to reduce the shot-to-shot jitter; and etc.

Careful measures would have to be taken to reduce the pole-integral errors below 0.01%, because remnant fields and earth field coupling to the ferrocores are important; these are DC fields and would have to be measured independently of the pulsed portion of the wiggler field. Additionally, the variations in the position of the magnetic center (see Sec. 3.3.5) produce an additional effective field error of 0.01%: this might improve with reduced pole integral errors, but better coil fabrication techniques might also be required to provide adequate improvement. Also, stray pulsed fields generated by the pulsed power supply during the wiggler shots are of earth's-field magnitude at the wiggler, and so the pulsed power supply would have to be μ-metal-shielded. It could conceivably be easier to

reduce the effects of the earth's field with a μ-metal shield or Helmholtz coils, or both. Mechanical stability of the wiggler assembly also needs study at some level: the shock associated with the firing of the magnet slightly perturbs the positions of the coil windings and the drift tube, and adds shot-to-shot jitter. Thermal cycling could also disrupt the windings' configuration to the extent that the wiggler temperature might have to be controlled at all times, not just during operation. In light of these considerations, the probability of reducing the field errors below the 0.01% level seems small.

The MIT Microwiggler has unique flexibility as a research instrument for study of FEL physics. Profiles other than a uniform profile with tapered ends can easily be installed in this wiggler. For example, one might wish to operate an optical klystron [Drobyazko *et. al.*, 1989], which requires two distinct interaction regions with sinusoidal fields of the same period, separated by a dispersion region. It may also be possible to rewire the coil connections to produce a field region with three times the existing period, and another field region with the existing period, to permit operation of a harmonic generation FEL.

There are limits, however, to the kinds of profiles that can be tuned into the Microwiggler. As shown in the field time dependence studies of Sec. 3.3.2, half-periods operating in the linear regime have different timing characteristics than those operating in the saturated regime. To avoid temporal asynchronism of the kind described in Sec. 3.3.2, the only practical profiles are those in which the coils (excluding the ends) are all operating in the saturated regime, or all operating in the linear regime.

CHAPTER 4

SPONTANEOUS EMISSION FROM A MICROWIGGLER

4.1 Introduction

This chapter presents the results of an experiment performed at the Accelerator Test Facility of the Brookhaven National Laboratory, in which 41 MeV electrons were passed through the Microwiggler magnet described in the previous two chapters. The resulting incoherent emission was collected and its spectral content determined. These measurements indicate that study of the incoherent emission (or "spontaneous emission", in analogy with incoherent atomic emission vs. stimulated atomic emission in a conventional laser) can provide a non-destructive diagnostic of the electron beam's transverse phase space distribution. Their acquisition also demonstrated the Microwiggler to be a useful scientific apparatus.

Section 4.2 describes the Accelerator Test Facility; this description is also important to the experimental work of Chapters 5 and 6. Section 4.3 is a brief description of the system for collecting, transporting, analyzing, and detecting the spontaneous emission. Section 4.4 presents measurement results and a comparison to theory. Conclusions and suggestions for future work are given in Sec. 4.5.

This chapter summarizes the masters thesis of Blastos [Blastos, 1994]. He has documented the spontaneous emission experiment*; the summary presented here is brief.

* And, indeed, he did all of the work of installing, aligning, and calibrating the apparatus for the transport, spectral analysis, and detection of the spontaneous emission. My only claim to any of these results is that I provided oversight to his diligent efforts..

4.2 The Accelerator Test Facility*

The Accelerator Test Facility [Batchelor *et. al.*, 1988] provides a high-brightness, short-pulse electron beam for use in development of novel acceleration schemes and new methods for free electron generation of coherent and incoherent electromagnetic radiation. The accelerator system consists of two principal subsystems: an injector and a LINAC. The high-brightness RF injection gun produces electron pulses of energy 1.5-3.6 MeV; these electrons can be used directly (as in the experiments of Chs. 5 and 6), or passed through the LINAC, which in turn accelerates the electrons to an energy of 20-70 MeV. Table 4-1 lists the ATF accelerator system's design goals**.

TABLE 4-1. ATF design specifications (from [Wang, 1992])

Energy, MeV	50-70
$\Delta\gamma/\gamma$ (1 standard deviation), %	0.3
Electron bunches/macropulse	1-200
Electron micropulse duration, psec	6-20
Macropulse duration, μsec (100 bunches)	2.1
Peak current, amperes	100
Normalized emittance ε, π mm-mrad	<7
LINAC repetition rate, shots/sec	1.25-6

* This discussion draws extensively from the Ph.D. thesis of Wang [Wang, 1992]. The presentation here is brief.

** While the system is reaching the conclusion of its development at the time of this writing, some of the design parameters listed in the table have not yet been achieved; the exceptions of note to this work will be mentioned as necessary.

4.2.1 The ATF injector

The ATF injector consists of a 1-1/2 cell, π-mode, side-coupled RF gun, excited by pulsed RF fields of frequency 2.856 Ghz. A short-pulse (5-20 psec), frequency-quadrupled Nd:YAG laser pulse (of total energy ~100μJ) enters the cavity along its axis and strikes a copper cathode. The 266-nm wavelength (4.65 eV) photons of the quadrupled Nd:YAG laser are sufficiently energetic to cause photoemission from the cathode; the laser is mode-locked to the RF cycle, and its pulses are timed to strike the cathode at a time when the axial electric field component is directed toward the cathode. Thus, electrons can be extracted from the cathode and accelerated at an appropriate time in the RF cycle to minimize their energy spread and transverse momentum. The electron pulse length closely follows that of the laser pulse.

The accelerator will ultimately produce a series of 1-200 electron bunches, or micropulses, at intervals of 12.25 or 24.5 nsec. Such an assemblage of micropulses is called a macropulse. For the experiments of this work (both the Smith-Purcell experiments of Chs. 5 and 6, as well as the experiments of this chapter) using the injector in photoemission mode, we used a single micropulse per macropulse, though on one occasion we used as many as seven.

There is another mode of operation of the injector system, extensively used in the experiments of this work. Rather than relying on prompt photoemission to produce electrons for acceleration, the laser is focused tightly on the cathode so as to ignite a plasma. The RF fields then extract electrons from the plasma cloud. A series of roughly twenty 20-psec micropulses occurs at intervals of 360 psec (one RF cycle). This process is known as "explosive emission" [Wang *et. al.*, 1992]. Explosive emission has stability properties useful to spontaneous emission experiments: Table 4-2 contrasts explosive

emission with photoemission. It must be emphasized that future coherent radiation experiments demand the superior beam quality (high current and low emittance) of photoemission operation. Explosive emission was useful for this work primariliy because of extreme stability and relative ease of operation of the laser system. We could tolerate reduced beam quality, since we detected total radiation emission energy per macropulse in all of the experiments of this work. Since the emission was incoherent, the signal was proportional to total charge- the peak current was irrelevant. This is decidedly not the case for a free electron laser; recall from eqn (1.27) that the FEL exponential gain factor scales as the 1/3 power of the beam current.

The ATF injector beam was used for the Smith-Purcell measurements of Chs. 5 and 6. The beam energy for those experiments was 2.8 MeV. Both the spectroscopy and coupling studies of Ch. 6 were carried out using explosive emission operating mode. I made a crude measurement of the emittance in explosive emission mode of the beam reaching the Smith-Purcell apparatus's vacuum chamber, with a result $\varepsilon = (4 \pm 1)$ mm $\cdot$ mrad. This is better than one might expect, but we hypothesize that the beam's emittance may be aperture-limited by obstructions (misaligned dipole chamber, etc.) upstream of the apparatus. The drawback of such unintentional collimation is reduction of the charge delivered to the experiment. Photoemission was used in selected runs to probe for possible coherence effects due to short electron bunch length (see Sec. 6.6). Though an emittance measurement was not performed, we did measure the total electron transmission efficiency in photoemission mode to be ~70% on one occasion, a value far exceeding that of explosive emission. This result suggests that the explosive emission beam may have been "cleaned up" by restrictions in the beamline.

TABLE 4-2. Photoemission vs. explosive emission

	Explosive emission	Photoemission
Charge per electron pulse: varies significantly with laser pulse energy?	Not significantly	Yes, total charge is proportional to total laser pulse energy
Beam steering: sensitive to position of laser pulse incidence on cathode?	No: plasma cloud created by laser is larger than laser spot	Yes
Beam emittance and energy spread: sensitive to timing of laser pulse incidence?	No	Yes
Beam emittance, π mm-mrad	~4-10 or greater	4
Beam energy spread, %	>1-2	0.3
Average current, amperes	< 10	100
Micropulse duration, psec	20 (fixed by RF cycle)	10 (adjustable)
Total charge per macropulse, nC	~3-10	1

4.2.2 The ATF LINAC

Electrons from the ATF injector could be routed into an RF LINAC consisting of 2 SLAC-style stages. These were powered by the same klystron used to drive the injector. When operated at full klystron power, the LINAC is capable of producing 70 MeV electrons: with the wiggler period of 8.8 mm, the emission from 70 MeV electrons has wavelength 235 nm, well into the UV. The experiment described in Sec. 4.4 was performed with electrons of energy 41 MeV, the klystron being incapable of driving higher

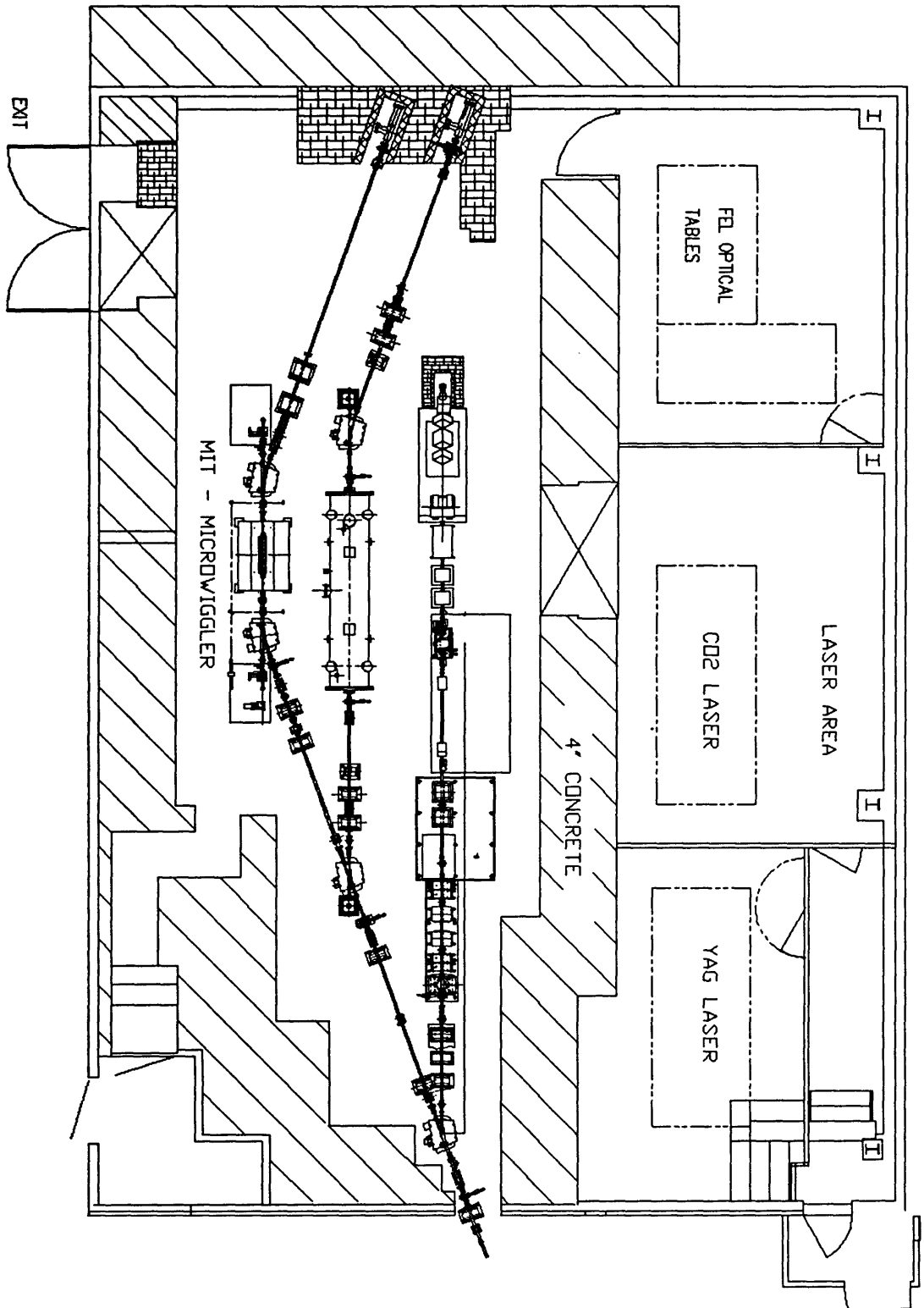

FIGURE 4-1. The Experimental Hall of the Accelerator Test Facility. The Microwiggler is situated in Beamline #3, along with its pulsed power supply. Trigger generation hardware, the pulsed power supply, and the control computer were located in the FEL room, which was shielded by a 4' thick concrete wall from the Experimental Hall.

energies at that time.

The ATF offers three high-energy beamlines for use by experimenters. The Microwiggler was placed in Beamline #3; Figure 4-1 depicts the ATF Experimental Hall, and the location of the Microwiggler therein. Beamline #3 contains beam profile monitors placed so as to permit beam alignment with the wiggler axis, as well as to support emittance measurements. Also depicted is the placement of the electron-optics elements to transport the beam to the wiggler; however, any discussion of the complex business of e-beam optics is beyond the scope of this thesis. The interested reader is again referred to [Wang, 1992] and the references therein.

4.3 Spontaneous emission: collection, transport, analysis, detection

4.3.1 The light transport system

Access to the experimental hall was forbidden to experimenters during accelerator operation due to a hard radiation hazard. Therefore, spontaneous emission produced in the Microwiggler was transported from the experimental hall to the FEL room (see Fig. 4-1) so as to provide experimenters with easy access to optical components. The transport path was totally analogous in structure to the light transport system used in the Czerny-Turner spectrometer of Sec. 5.3. Figure 4-2 shows the four 2" dia. lenses that collect and collimate the radiation. The source (for spontaneous emission, the middle of the Microwiggler) is placed in the focal plane of the collecting lens, which in turn is in the focal plane of the first transport lens. The two -identical- transport lenses are separated by twice their focal length. Finally, the condensing lens is located in the focal plane of the second transport lens, and the system images in the focal plane of the condensing lens. The transport lens' focal lengths were 2.5 m, and the collecting and condensing lens' focal lengths were 1.75 m, for an optical path of 13.5 m.

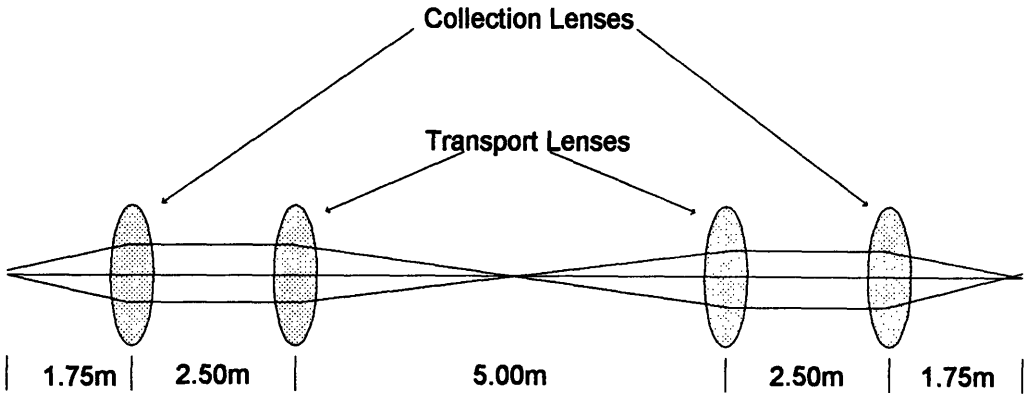

FIGURE 4-2. The optical transport scheme. The method is identical to that employed in the Czerny-Turner spectrometer of Ch. 5 (from [Blastos, 1994]).

The seven mirrors in the optical path were dielectric-coated for optimal operation from 400-690 nm. As it turns out, we observed emission in the wavelength range 690-840 nm. Accordingly, Blastos carried out reflectivity measurements on each of the mirrors in the transport system [Blastos, 1994]. These reflectivity measurements have been incorporated in the spectral analysis in the next section.

Background light was excluded from the transport path by means of a series of light-tight boxes and tubes, cunningly fashioned from PVC sheet and ABS plumbing tubing. Also, components on the optics table were placed inside similar light-tight boxes. This was necessitated by the broadband response of the Hamamatsu photomultiplier (PMT) tubes used to detect the emission (see Sec. 4.3.2): they were even more sensitive in the visible than in the near IR.

A HeNe laser was used to align the axis of the collection system with the nominal surveyed electron beam axis. Bending magnets at either end of the wiggler served to displace the electron beam from the Mirowiggler/emission axis. Two removable phosphor screens at either end of the Microwiggler were used as references for the HeNe alignment

of the optical system. Subsequently, during the measurements, the electron beam was aligned using the same removeable phosphor screens.

4.3.2 Emission analysis and detection

Figure 4-3 illustrates the experimental setup on the optical table. Upon entering the optics table in the FEL room, the light passed through a low-pass filter (cutoff wavelength 500 nm), and struck a 50-50 beam splitter; half the emission was directed onto a Hamamatsu PMT tube, the other half was focused onto the input slits of a SPEX 270M spectrometer. Another Hamamatsu tube was placed on the output of the spectrometer. This system permitted measurement of the total emission power simultaneously with the spectrometer-dispersed signal. Thus, the dispersed signal could be normalized to the total power, reducing the effects of shot-to-shot steering and amplitude jitter, since the gains of both tubes were known.

The spectrometer was of Czerny-Turner configuration, and was operated with 1200 lines/mm diffraction gratings; the resulting resolution was 3.1 nm/(mm output slit width). We typically operated with an output slit width of 2 mm, for resolution much better than the scale of the observed spectral features.

Blastos performed a careful absolute calibration of the PMTs with an LED whose brightness was reasonably well-known [Blastos, 1994]. Use of an LED permitted good determination of the relative gain of the tubes, though the absolute calibration has considerable uncertainty. The calibrations permitted him to estimate, based on the total detected emission power, the total charge in the electron beam. His result is presented in Sec. 4.4.

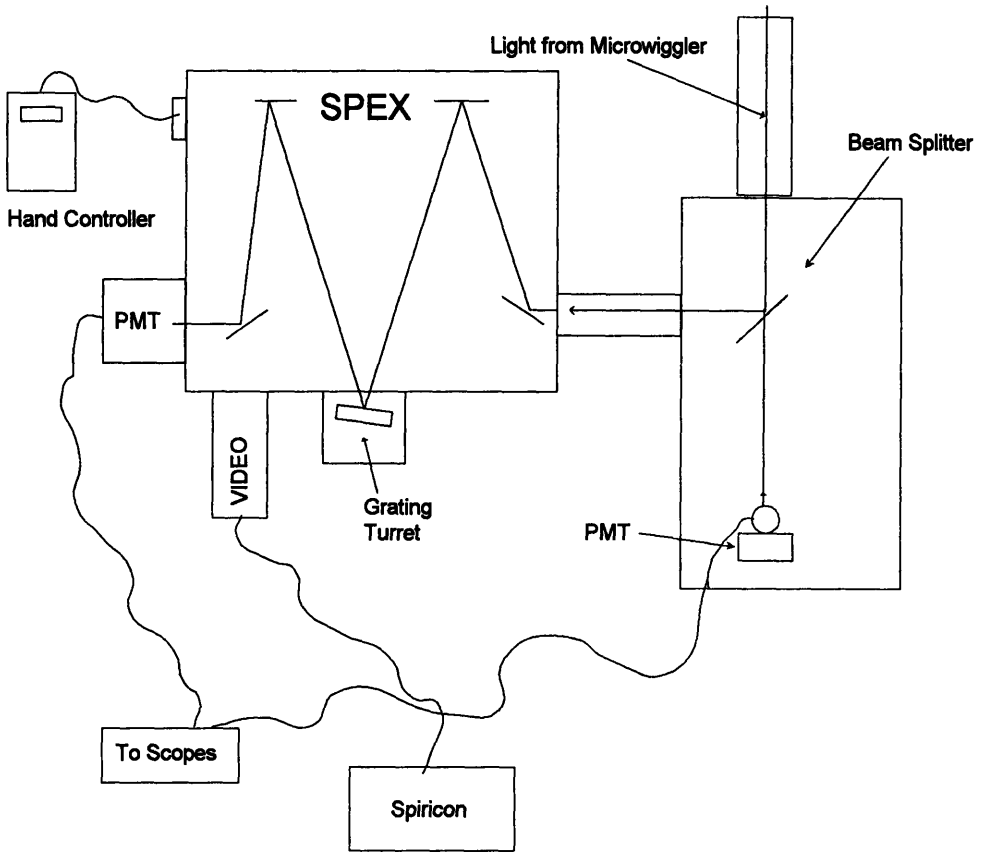

FIGURE 4-3. The optical table setup for spontaneous emission power and spectral analysis (from [Blastos, 1994]).

4.4 Spontaneous emission experiment and results

Spontaneous emission was observed during two runs as of June 1994: November 1993 and January 1994. The November 1993 results are presented in [Sisson, 1994] and will not be discussed here, except to say that the first convincing observations of the spontaneous emission were made. I will summarize the results of the January 1994 run, discussed in detail in [Blastos, 1994].

We were hampered during the run by a temperamental klystron (powering the injector and accelerator: see Sec. 4.2), which would periodically arc, with the effect of a significant power loss from which several minutes were required for it to recover. This

power loss resulted from vacuum degradation produced by the arc. The power loss had the undesireable effect of producing a concomitant sag in the beam energy. Since all the beam steering and focusing elements' current settings scale linearly with beam energy, severe steering aberrations were produced by the klystron arcs. Thus, two experimenters worked in the control room: one operated the accelerator, and the other remained in communication with experimenters in the FEL room by telephone, informing them of loss of beam. Both beam tuning and data acquisition were inhibited by the klystron problems- all the data presented in this chapter were acquired during the last four hours of a 29-hour run.

Beam energy and energy spread could be measured by examination of the beam's image on collimator slits downstream of a bending dipole (both downstream of the LINAC). We placed the energy spread at about 0.6 MeV, at a beam energy of 40.9 MeV; therefore $\Delta\gamma/\gamma = 1.5\%$ for the run. The diameter of the beam up and downstream of the wiggler could only be estimated since the phosphor screens there had no fiducial marks. However, I estimated the (2σ) diameter to be of order 2 mm.

Such a beam size is consistent with a very interesting effect observed on the downstream pop-up phosphor screen. The wiggler compressed the cross-gap size of the beam by about a factor of two as compared to the wiggler-off size, demonstrating wiggler focusing. I believe the effect to be beam compression rather than beam loss, since the compressed spot was much brighter than the uncompressed spot. The betatron period (see Sec. 1.2.3) was about 3.6 m, so that the electrons underwent 1/6 betatron periods inside the wiggler. An electron injected parallel to the axis, but at a non-zero y-value y_o, follows a y-trajectory given by the solution to the betatron equation of motion, eqn. (1.16), which is

$$y(z) = y_o \cos(k_\beta z). \tag{4.1}$$

For $z = \lambda_\beta/6$, this yields $y_o \cos(k_\beta z) = 1/2$, so that the observed beam compression is consistent with the result of the linearized betatron equation of motion. This suggests that the beam was probably not much larger than 1-2 mm or so in diameter.

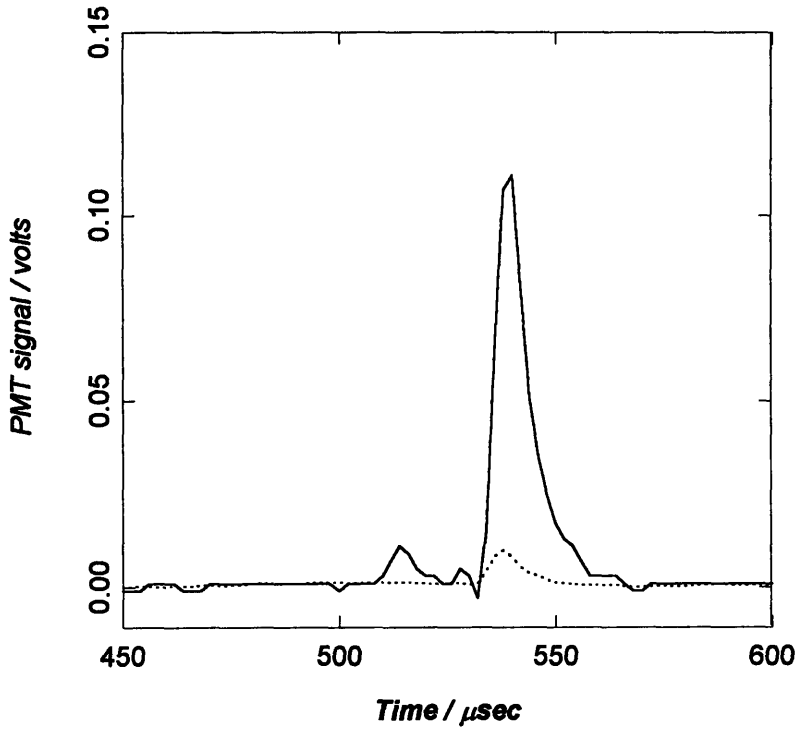

FIGURE 4-4. A plot of the PMT voltage with (solid line), and without (dotted line) the wiggler present during the passage of the electrons through the wiggler. There is a strong correlation between signal strength and the presence of a wiggler field.

The injector was operated in photoemission mode, with one micropulse for macropulse. The accelerator system operated at 3 pulses/sec, while the Microwiggler fired at only 0.5 pulses per second. This reduced the rate of data acquisition, but also provided a useful monitor of noise pickup, in that (of course) whatever signal was present with wiggler off was some kind of pickup. There was no automated experimental control, experimenters acquired oscilloscope traces from the PMTs and recorded peak pulse amplitudes by hand (a few sample traces were saved to disk). Figure 4-4 is a plot of a

PMT voltage pulse. Of course, no temporal information about the emission could be discerned from the voltage pulse (the radiation pulses were tens of picoseconds in duration, whereas the voltage pulses were of order 10 μsec in duration).

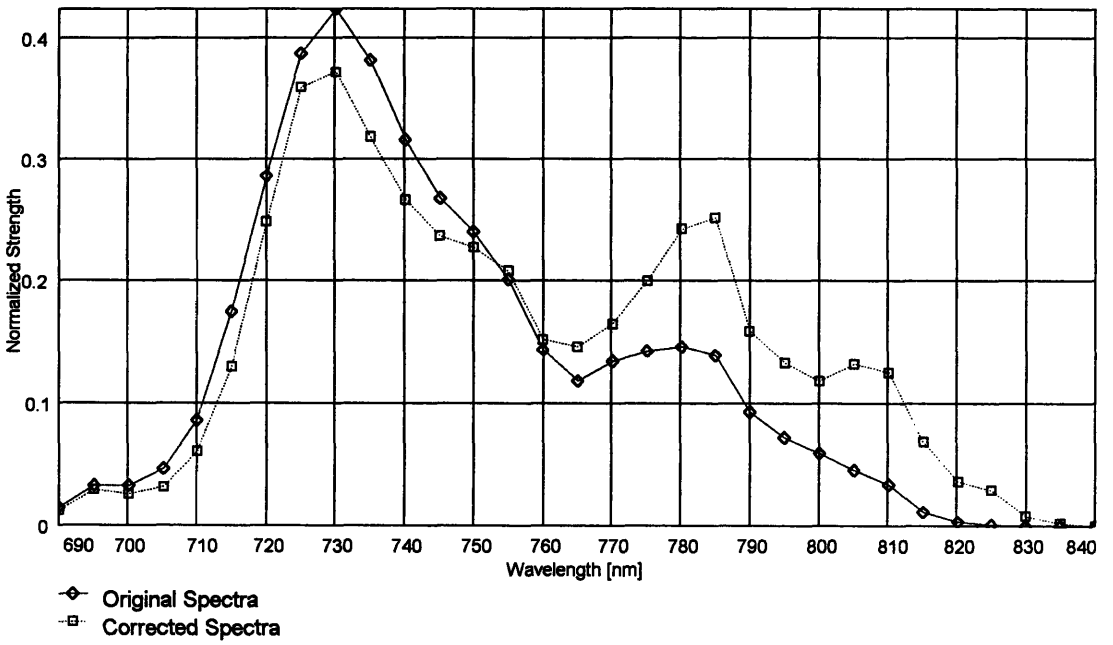

FIGURE 4-5. The measured spectral profile of Microwiggler-induced spontaneous emission, January 1994. Shown are plots of the raw spectrum, and the profile resulting from the application of the mirror reflectivity calibration of Sec. 4.3.1. (from [Blastos, 1994]). The energy was 40.86 MeV for these scans.

Each spectral datum was the average of 4 shots, and was normalized to the total emission energy (measured simultaneously- see Sec. 4.3.2). Four spectral scans were taken to reduce the considerable effects of charge amplitude and beam-steering jitter. The scans were averaged, and corrected for the effects of the mirrors' spectral response. The results are plotted in Fig. 4-5. The measured curve has also been smoothed with nearest-neighbor convolution, a legitimate expedient considering the breadth of the spectral peak. Several observations can immediately be made. The "natural linewidth" of emission from a single electron in a 70-period wiggler is around 10 nm (see Sec. 1.2.4, eqn. (1.23)); moreover, the single-electron spectrum is symmetric about its center value. The measured

spectrum of Fig. 4-5 is much broader, and asymmetric. Obviously, finite-beam effects are playing a significant role. Also, the spectrum's peak wavelength is displaced about 5 nm to the red of the expected single-electron spectral peak. The close agreement is strong evidence that the emission is due to a wiggler interaction, instead of some kind of electron impact excitation or other mechanism (the other indicator being that the signal extinguishes with the wiggler off).

We observed a pronounced shift in the peak wavelength with a shift in beam energy. Figure 4-6 shows two spectrometer scans conducted at energies different by about 0.5 MeV. Eqn. (1.6) would then predict an energy shift of $\Delta\lambda/\lambda = 2\Delta\gamma/\gamma \cong 2.5\%$, which amounts to a shift of about 18 μm. The observed shift was larger by a factor of two. The overall shift is in the correct direction in any case- further evidence that the emission is wiggler-induced.

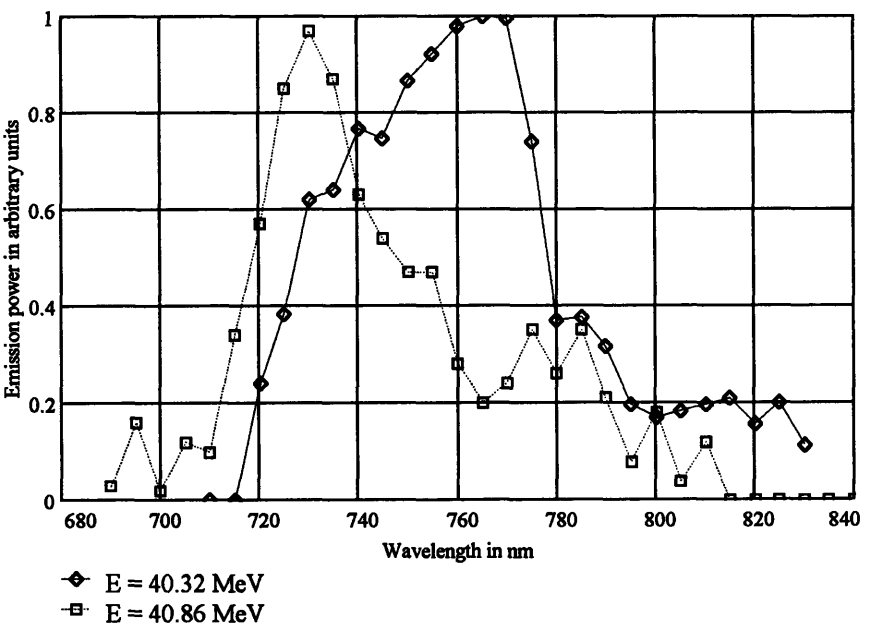

FIGURE 4-6. Scans at different energies exhibit a wavelength shift. The shift is about twice as large as would be indicated by an energy shift alone. Mirror reflectivity corrections have not been made.

Blastos has carried out a detailed analysis of the broadening/redshifting mechanisms acting to produce the spectrum of Fig. 4-5 [Blastos, 1994]. The mechanisms are:

- Energy spread. The emission wavelength scales as $1/2\gamma^2$, thus it can be easily shown that $\Delta\lambda/\lambda]_{\text{energy spread}} = \Delta\gamma/\gamma$. Thus, an additional 10 nm of broadening results from energy spread.

- Off-axis electron propagation. Electrons "see" a stronger wiggler magnetic field when displaced from the wiggler axis (see eqn. (1.9)). The emission wavelength is increased as a result- the wiggler parameter a_w is proportional to the wiggler field strength, and the emission wavelength scales as $(1 + a_w^2/2 + \gamma^2\theta^2)$ (see eqn. (1.6)). For a beam of 1 mm radius, the emission wavelength is shifted to the red by about 1/2 percent, and one would expect broadening of similar magnitude.

- Off-axis electron emission/transverse electron motion. Light propagating in a direction other than the electron's motion is redshifted in comparison to co-propagating emission (see Sec. 1.2.1, and eqn. (1.6)). We collected light over a solid angle of π(4 mrad)^2 about the wiggler/e-beam axis. Also, the beam divergence could easily have been of mrad order. In any case, at 4 mrad, $\gamma^2\theta^2 \cong 0.1$, so that this mechanism can broaden by a significant amount, of order 10%.

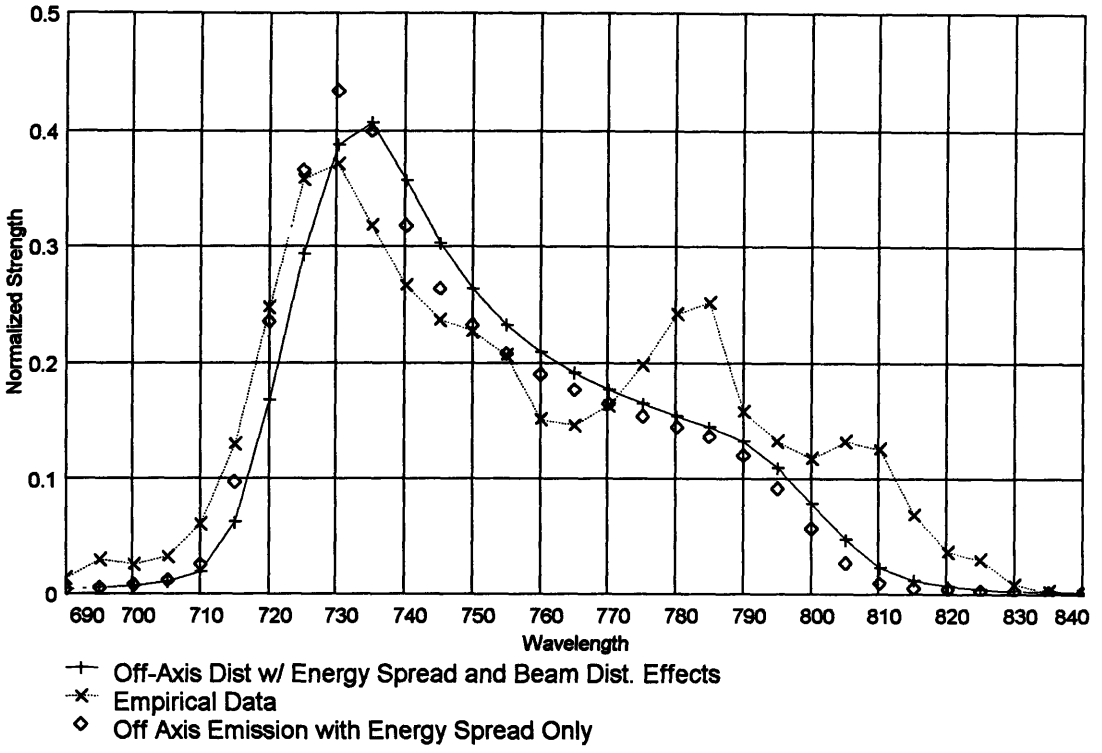

FIGURE 4-7. The emission spectrum: measured and theoretical emission spectral profiles. Off-axis emission effects dominate over the effects of off-axis electron propagation.

Based on these order-of-magnitude analyses, the main broadening mechanism was off-axis emission, with a small peak redshift due to off-axis beam propagation. Energy spread also contributed to the broadening as well. Blastos has confirmed these assertions with two detailed calculations. His results are plotted in Fig. 4-7. Both assume a perfectly collimated beam, i.e., no transverse momentum. Both assume that the emission is collected over a solid angle of $\pi(4\ \text{mrad})^2$. They differ in their assumptions regarding the transverse spatial distribution of the beam. One calculation assumes that all electrons propagate on the wiggler axis, while the other assumes a cylindrical beam with a Gaussian radial profile with $\sigma = 0.42$ mm. Addition of off-axis propagation induces a ~5 nm redshift, with little broadening. Both calculations show a long tail to the red, as do the measurements, but the calculations fall off more rapidly to the red than the data. This could be an artifact of the mirror reflectivity correction to the measured spectrum; the correction gets large at

wavelengths larger than about 770 nm, and errors therein have a significant effect on the spectral profile. The corrections may artificially amplify the red end of the spectrum. However, I do not ascribe the discrepancy solely to possible errors in the mirror reflectivity correction. I guess that the assumption of zero transverse momentum accounts in part for the discrepancy. In any case, the calculations do clearly demonstrate the dominance of off-axis emission broadening over off-axis electron propagation broadening- they show that the off-axis electron propagation induces a redshift, with little broadening.

Blastos has estimated the total bunch charge from the spectral data and calculations of Fig. 4-7. A high-precision calculation would require much more knowledge of the beam configuration than was available (essentially no quantitative information was available-- not even a Faraday cup total charge measurement). Appendix 2 describes how beam geometry affects Smith-Purcell emission, and analogous effects occur in the wiggler emission case. Thus, Blastos' estimate is unavoidably model-dependent. Along with his assumptions regarding the beam configuration (cylindrical beam with a Gaussian radial profile with $\sigma = 0.42$ mm and perfectly collimated and steered), he incorporated his PMT calibration, mirror reflectivity calibration, and collection system acceptance geometry to obtain the result $Q_{\text{total}} \cong 8$ pC. Given the uncertainty in his calibration of the PMTs, his estimate compares well to the estimate of 50 pC supplied by ATF personnel. Blastos apparently achieved an absolute total emission energy calibration accurate to better than an order of magnitude, an impressive result.

4.5 Conclusions and suggested future work

Our spontaneous emission spectral data and analysis demonstrate the dominance of off-axis emission in broadening the spectrum, as compared to off-axis electron propagation and energy spead effects. This dominance was predicted by [Friedman *et. al.*,

1988] in their exhaustive description of spontaneous and stimulated wiggler emission. With suitable collimation in the collection system, any off-axis emission collected will be due to electrons with significant transverse momentum. Thus, the spontaneous emission spectrum should serve as a fast (of order 10^1 sec), non-destructive diagnostic for assessment of the electron beam's transverse phase space distribution. Most techniques involve blocking the beam with a phosphor screen and varying the current setting of an upstream quadrupole over a range of settings; usually, time of order 10^1 minutes is required to carry out such a procedure.

This possibility can be explored in the next run, given that the charge per bunch is larger than the anemic value (~10-50 nC) used to produce the data of this chapter. With a factor-of-ten increase in the charge per bunch, the solid angle of collection can be reduced by a factor of three (to ~ π(1 1/3 mrad)^2) without loss of signal; the presence of electrons with normalized transverse momentum exceeding ~2 mrad would then be readily detectable. It should not be too difficult to extract a reasonable measurement of the transverse momentum distribution's FWHM from the spontaneous emission data. In addition, beam steering errors may well produce discernable redshifts, thus permitting their ready identification.

Multiple-micropulse operation will make possible the acquisition of an entire spectrum from a single macropulse, by dispersing the light onto a CCD camera array in the spectrometer, instead of the spectrometer output slit. The CCD array will integrate over the incident emission lightpulses; it can be shown that enough light will be generated from a single macropulse (consisting of 100, 1-nC micropulses) to provide SNR in excess of 10^1. Such rapid acquisition of the spectrum could permit measurement of the beam emittance in times of order 10^0 minutes, without blocking the beam. Conceivably, a user

downstream of the wiggler could simultaneously acquire beam emittance data while conducting another experiment.

Of course, exploitation of spontaneous emission spectra is only a means to the end of demonstrating at first a visible-wavelength, and then a UV-wavelength, free electron laser. A visible-wavelength or UV oscillator would be the first ever devised that employed a sub-cm-period wiggler. Gain-narrowing of the emission spectrum is one of the principal indicators of stimulated emission, so that hardware and expertise in acquisition of spectral data will serve well the FEL development effort.

At the time of this writing, considerable work remains before an attempt to produce lasing can occur. An optical cavity must be installed, and its mechanical and optical stability studied. The electron beam current and emittance must be improved significantly. Also, the photoemission multiple-micropulse system must be installed and tested.

CHAPTER 5

THE SMITH-PURCELL EFFECT: APPARATUS AND TECHNIQUES

5.1 Introduction

In this chapter I describe the experimental apparatus and measurement techniques used to perform the experiments of Chapter 6. The experiments were performed at the Accelerator Test Facility of the Brookhaven National Laboratory.

Section 5.2 describes the overall structure of the beamline apparatus, including the vacuum system and the optical system for collecting and transporting the Smith-Purcell emission out of the radiation shield to the experimenters. Section 5.3 describes the Czerny-Turner spectrometer used to analyze the spectral content of the emission. Section 5.4 discusses the liquid-helium-cooled detector for the FIR and mm-wave emission, and Section 5.5 documents the computer system for recording measurement results and remotely controlling the beamline apparatus. Section 5.6 describes in detail how the measurements of Chapter 6 were made, including both beam diagnostic measurements as well as radiation measurements.

5.2 The beamline apparatus

5.2.1 The vacuum system, mechanical supports, and radiation shielding

The beamline apparatus, including the vacuum vessel and the light collection system contained therein, was inherited from the Oxford/Dartmouth collaboration of [Doucas *et. al.*, 1992]. It remained for me to design and install a support stand for the vacuum vessel, to procure and install vacuum pumps and gauges, and to construct a radiation shield. The resulting configuration is shown in Fig. 5-1. The experiment was located at the terminus of the ATF's Z-line, fed directly by the ATF injector (see Sec. 4.2).

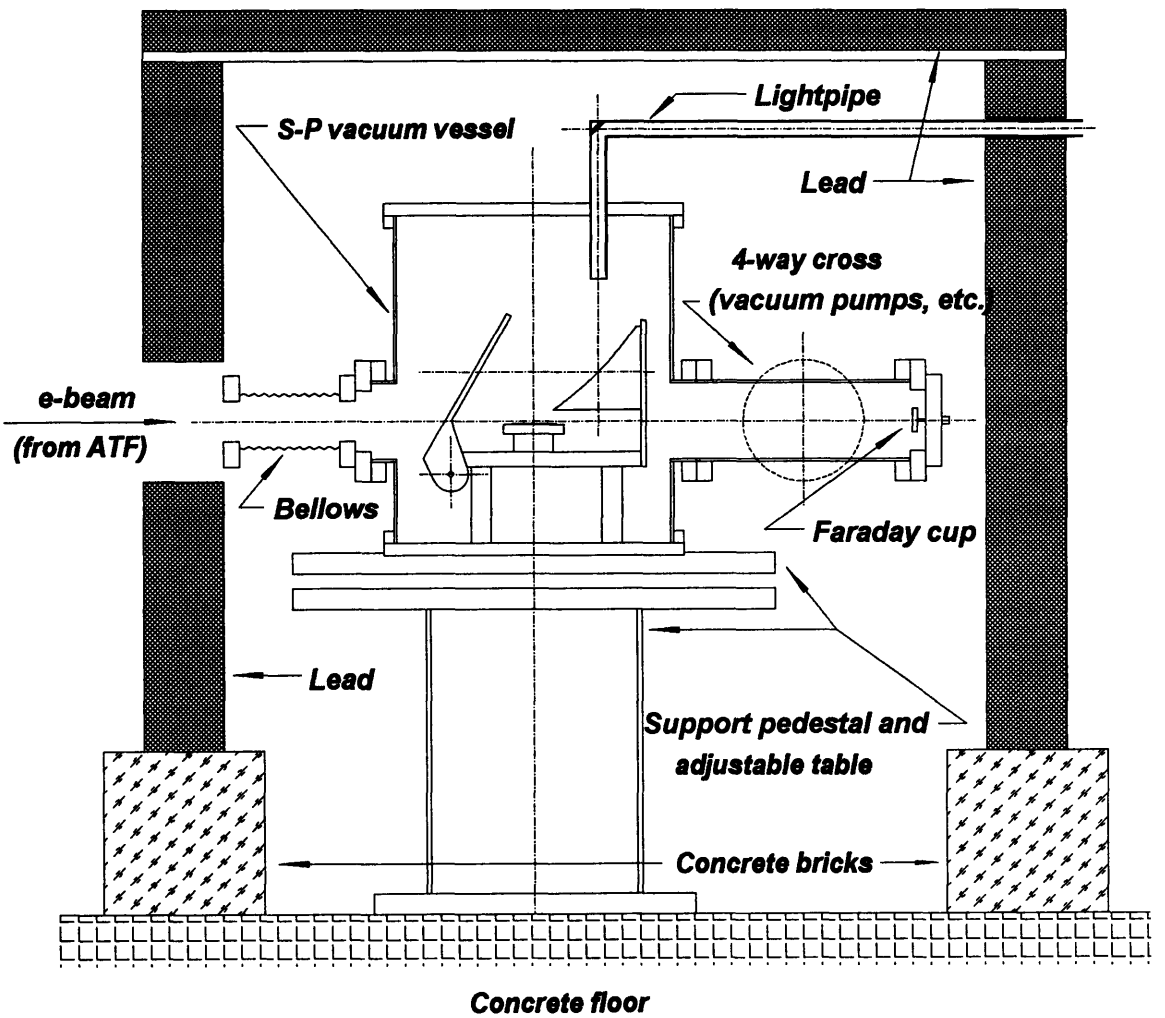

FIGURE 5-1. The Smith-Purcell apparatus, with support table and radiation shields. The system is shown in the configuration for viewing backward emission, and is drawn to scale. To establish scale, note that the beam axis is 24.125" above the floor.

The lightpipe was brought through the radiation shield via a small aperture. Electrical connections were routed though a gap in the concrete bricks supporting the lead. A Unistrut-braced, 1/2"-thick aluminum plate topped the shield walls, and supported a 700 kg* layer of lead bricks to provide the top shielding layer. The principal radiation hazard was x-rays, produced via bremsstrahlung interaction of the electrons with the Faraday cup and/or the Smith-Purcell grating. The support table was constructed of 2.54 cm aluminum plate, with 20 cm dia. tubing serving as the pedestal. The table was sufficiently strong to rigidly support the vacuum vessel (which massed at some tens of kilograms), and sufficiently adjustable to permit alignment of the vacuum vessel with the surveyed electron beam axis. I installed alignment pins into the vacuum vessel's bottom flange, which fit into holes in the adjustable table upon which rested the vacuum vessel. These pins precisely located the vessel, so that it could be detached and reinstalled without loss of alignment. This capability was necessary because the vessel had to be turned around (rotated 180° about its vertical axis) in order to change from viewing forward emission to backward emission, and vice versa.

A Varian cryopump provided the ultimate vacuum for the experiment, and was connected to the vacuum vessel via a 4-way cross attached to the downstream end of the vacuum vessel (see Fig. 5-1). Pressure was monitored with an ion gauge. Typical ultimate pressure was of order 10^{-7} torr, attained after several days of pumping subsequent to a vacuum break, though pressures of order 10^{-6} torr could be tolerated during experimental operation.

* The mass is relevant only because the top layer had to be frequently removed to access the vacuum vessel.

5.2.2 Mechanical actuators for experimental control

Three actuators inside the beamline apparatus were used to control the Smith-Purcell interaction. The mechanical force exerted by each was transmitted by a linear-actuator vacuum feedthrough, pushed by a micrometer drive. The activation torque to the micrometer drive was supplied by a 220 VAC induction motor. The position of the actuator was reported by a 10-turn potentiometer linked via a gear drive to the micrometer rotation; the potentiometer resistance thus established the actuator's position. Limit switches prevented the actuators from running out-of-range.

One actuator moved the grating vertically to vary the electron beam displacement relative to the grating surface. Another served to vary the collection mirror orientation. A third actuator moved the grating assembly laterally. Two gratings could be installed and used in turn by appropriate setting of the grating assembly's lateral position. A phosphorescent target was also attached to the grating assembly. With the assembly in the appropriate lateral position, the electron beam could be directed onto the target for viewing of the beam profile (see Sec. 5.6.4 for a description of the beam profile viewing system).

5.2.3 The Smith-Purcell emission collection system

The Smith-Purcell emission collection system is shown in Fig. 5-2, along with its optical equivalent. As discussed in Chapter 1, the dependence of emission wavelength on emission angle is a central distinguishing characteristic of Smith-Purcell radiation. It is therefore important to be able to select out desired emission angles in order to verify the angle-wavelength relationship. Electrons passed at grazing incidence over a grating, and induced it to emit as shown. A plane collection mirror, rotatable via mechanical actuators, selected emission at a desired angle. The grating could be moved vertically over a range of

7 mm. The collection mirror could view emission over an angular range of 90°-158° with the system set up for backward viewing (the orientation of Fig. 5-2); correspondingly, forward emission viewing angles ranged from 22°-90°. The emission reflected from the collection mirror was then focussed by an off-axis paraboloidal mirror (OAPM) into a lightpipe*. The emission then passed out of the vacuum vessel through a TPX** window; a periscope transported the emission around a 90° bend in the lightpipe. The emission was then borne by the lightpipe out of the radiation shielding to an optical table.

Figure 5-2 also shows a schematic of the collection system optics. Emission from the grating image is focused into the lightpipe aperture, placed in the focal plane of the focussing lens. A lens focuses the emission along a given direction into a point in the lightpipe aperture. Thus, the lightpipe aperture size determines the range of angles collected by the optics at a given setting. That angular range is given by the lightpipe diameter divided by the focal length of the lens. Thus, $\delta\theta \approx d/f = (20/116) = 0.17$ rad (= 9.7 °) was the full range of emission angles collected at a given emission angle setting. Since the OAPM does not behave like an ideal lens, this range is only an estimate. The fractional wavelength range corresponding to this emission angle acceptance range is emission angle dependent:

$$(\delta\lambda/\lambda) = \frac{1}{\lambda}\frac{d\lambda}{d\theta}\delta\theta = \left(\frac{\sin\theta}{1/\beta - \cos\theta}\right)\delta\theta \qquad (5.1)$$

* The term "lightpipe" might be misleading in that I do not refer to a device to convey visible light, like an optical fiber; the lightpipe referred to is a 2-m length of 20mm-ID copper tubing.

** TPX is a trade name for a plastic with good transmission properties in the sub-mm and mm wavelength ranges. Its refractive index is nearly constant from microwave to visible wavelengths. It is also transparent to visible light, a property useful when using a laser to align the system.

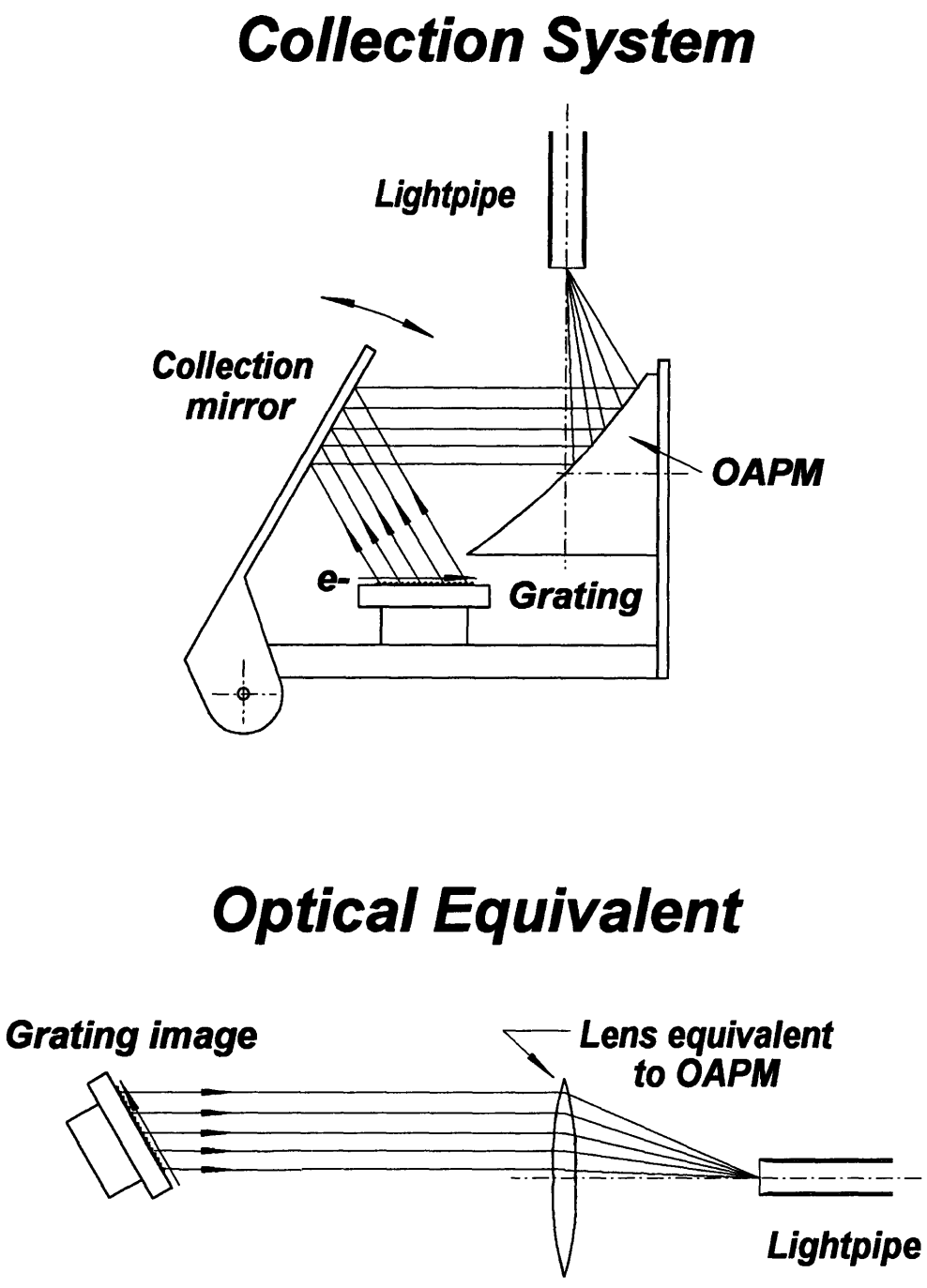

FIGURE 5-2. The Smith-Purcell emission collection system and its optical equivalent. The collection mirror can be rotated, in the direction indicated, to permit collection of emission at various angles. Rotating the collection mirror changes the orientation of the grating image, thus changing the angle of collected emission. The drawings are to scale.

As an example, this formula yields a value of $\delta\lambda/\lambda \approx 12\%$ full range at an emission angle of 112° (the angle at which an important spectral feature occurs- see Chapter 6).

The spectroscopy studies of Chapter 6 rely on having at least a qualitative knowledge of the collection system's angular range and response, since that response is imposed on the measured wavelength spectrum of emission emerging from the lightpipe. It is important to verify that the collection system response curve has no sharp structure or irregularities, and to show that its shape and amplitude do not change appreciably over the wavelength/emission angle range of the data of Ch. 6. Detailed knowledge of the collection system response is not required, however, since its effects can be integrated out (see Sec. 6.3.2). Unfortunately, it is not possible to measure that response in detail (though the FWHM of the response curve can be measured- see Sec. 6.3). Correspondingly, I constructed a computer simulation of the collection system. Figure 5-3 displays the results of a calculation modelling the collection of 113° emission. The plot shows the variation of transmitted power as a function of angle. The program traces a set of rays at a given emission angle from a grid of points on the grating surface to the lightpipe aperture plane. If the ray enters the lightpipe, it contributes to the power collected at the given emission angle according to how many bounces off the (finite-conductivity) lightpipe walls the ray executes while in the lightpipe. The ray's contribution is attenuated exponentially in the number of bounces:

$$P_{ray} = P_o \exp(-R \cdot n_{bounces}), \qquad (5.2)$$

where R is the lightpipe reflectivity, and $n_{bounces}$ is the number of bounces. The number of bounces for a given ray is determined by the angle of the ray's injection into the lightpipe. This ray-tracing approach is only valid in the limit of the wavelength being much shorter than the lightpipe radius ($r_{LP} = 1$ cm), so that waveguide and diffraction effects need not be considered. Figure 5-3's simulation assumes a wavelength of 1.4 mm, an acceptably

small value, and the wavelength at which the spectroscopy measurements of Chapter 6 were performed. Note that the response curve is non-zero over an angular range of 0.24 rad (=14°), a larger value than yielded by the simple estimate earlier mentioned, 0.17 rad (= 9.7 °). Diffraction effects will tend to further broaden the response curve. Radiation of finite wavelength λ cannot be focused to a point by the OAPM as are the rays in Fig. 5-2, but rather are concentrated into a region of size $\sim f_{OAPM}\lambda / D_{OAPM} \approx 1.25\lambda$, where f_{OAPM} and D_{OAPM} indicate the OAPM focal length and diameter. Thus, some radiation is introduced into the lightpipe aperture by incoming rays nominally focused at distances as great as 1.25λ outside it.

The reflectivity parameter R used in the collection system simulation has been estimated on the basis of the measured efficiency of the lightpipe in transporting FIR radiation from a 5000° blackbody source. The transmission efficiency was about 70%*. Thus, the appropriate value for R could be estimated by adjusting its value in the simulation so that the system passed 70% of the power in the (R = 1.0) case. This technique yielded a value of R = 0.98. It should be emphasized that neither the shape nor the peak amplitude of the simulated collection system response curve vary significantly with emission angle for $R > 0.9$ or so, so that exact determination of the value of the reflectivity parameter is unnecessary.

It should also be mentioned here that the collection system's angular (and therefore wavelength) response depends to some extent on the distribution of the beam current over the grating, since the emission strength from a given point on the grating is proportional to the beam density at that point. The collection system model can incorporate the effects of beam geometry, by weighting contributions from various grating positions according to

* This measurement was made by K. Woods.

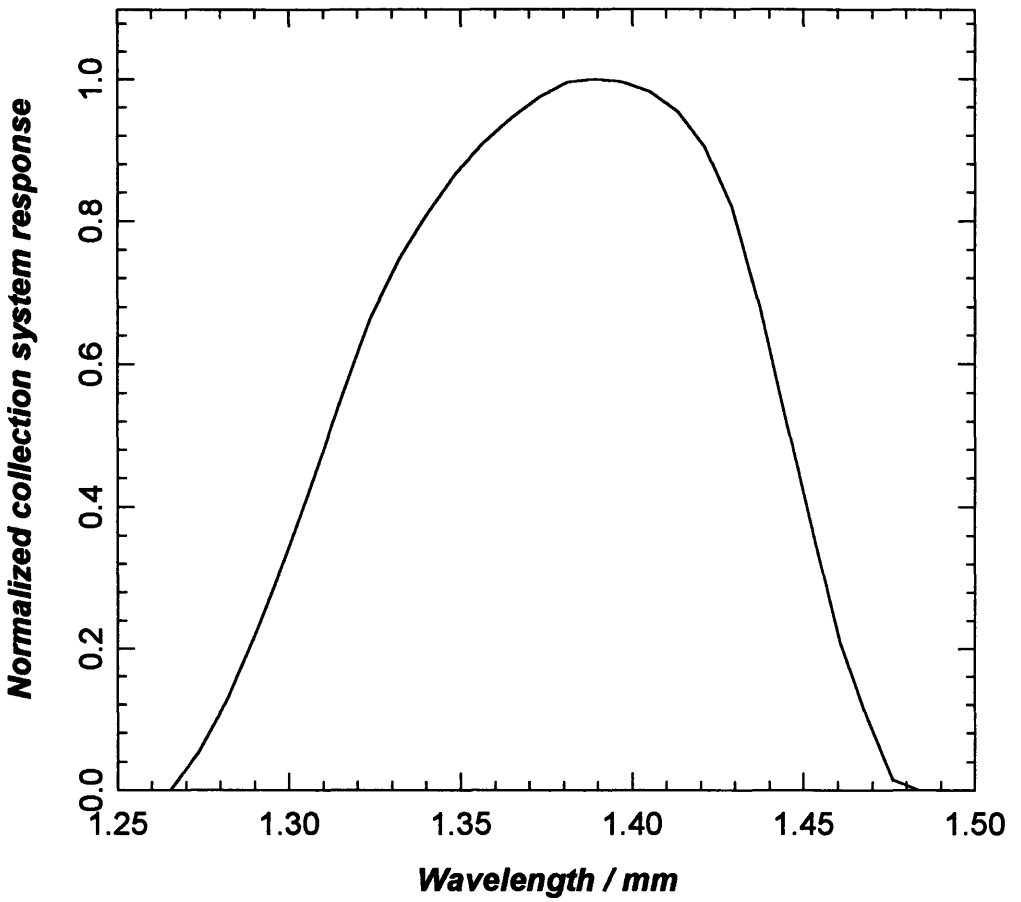

FIGURE 5-3. Collection system response curve, for a nominal setting of 112 degrees. The collection system model omits diffraction effects and waveguide effects.

the beam density distribution at those positions. However, I will show in Appendix 2 that the emission from the grating does not vary significantly along its length.

The ideal collection system would permit either the selection of a narrow range of emission angles (to permit identification of the emission as due to the Smith-Purcell effect), or a wide range of emission angles that contain some spectral feature of interest. The ideal response curve would be flat in either case. The collection system used was better adapted to identifying Smith-Purcell emission than to doing spectroscopy. A future

apparatus would do well by possessing a broader angular acceptance range and a flatter response curve to facilitate spectral studies.

5.2.4 The Smith-Purcell gratings

Figure 5-4 illustrates the surface geometry of the gratings used to produce Smith-Purcell emission in these experiments. We chose a blazed grating geometry for several reasons: such gratings are easily made; the emission spectra they produce is readily calculable theoretically; and a stock of such gratings was available at the outset of the experiment.

The gratings were fashioned from aluminum alloy 6061 on a CNC milling machine. The surfaces were cleaned with acetone and methanol prior to the gratings' installation into the beamline apparatus, but were not treated to remove the Al oxide layer; this omission did not result in any obvious experimental ill effects.

In nearly all of the experiments performed, the electron beam was at least partially intercepted by the grating (see Sec. 5.6). To prevent charge buildup, the grating was electrically grounded. The electrons were insufficiently energetic (2.8 MeV- see Table 4-1) to induce nuclear activation, so that the gratings could be installed and removed without concern over radiation hazard. Also, there was no heating problem associated with the beam impact on the gratings since the average beam power was of order 10-20 mW, and the gratings were of mass ~10^2 gm. In addition, the gratings were well thermally sunk to the vacuum vessel.

The periods of the gratings ranged from 1-10 mm. Their lengths varied from 62-200 mm, and their widths from 17-25 mm. The blaze angles θ_b used were 5°, 20° and 30°,

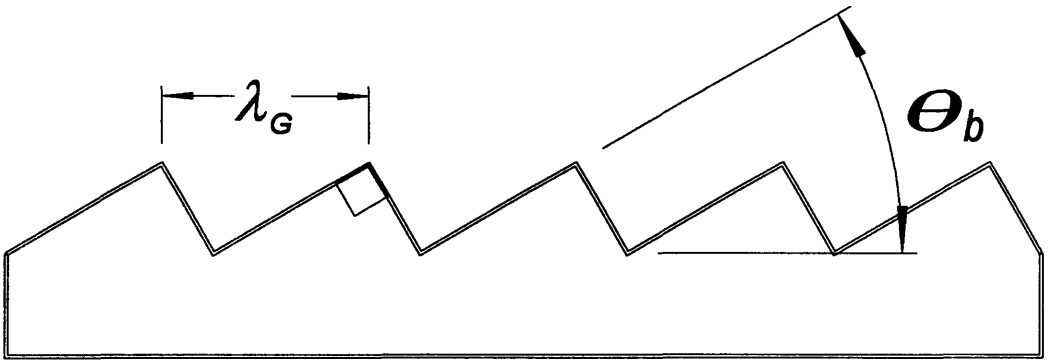

FIGURE 5-4. The gratings used to induce Smith-Purcell emission. The period is λ_G, and the blaze angle is θ_b. The cross-section of the grating rulings is a right triangle, as indicated.

though all of the data in this thesis were taken from the 30° gratings.

The gratings were always oriented so that the electrons of the beam "washed up onto shore"* , i.e., the beam for the grating oriented as in Fig. 5-4 would travel from left to right. This is an important point since the emission spectra for the two possible beam directions are different. In particular, Woods has shown [Woods, private communication 1993] that the spectral peaking effect described in Ch.6 is predicted to be much more pronounced for the beam direction we used in our experiments.

5.3 The Czerny-Turner spectrometer

In addition to the beamline apparatus, Prof. Walsh also inherited an old but serviceable mm-wave/FIR spectrometer from his Oxford collaboration. Though it originally saw service in fusion research in the 1950's, it proved quite valuable in our efforts. Figure 5-5 shows a scale drawing of the spectrometer, along with the optical equivalent. The spectrometer consists of a diffraction grating, and transport optics to present the radiation to, and carry the radiation from, the grating. All components are rigidly fastened to an uncovered aluminum frame open to atmosphere. Spectra are

* A mnemonic passed to me by Prof. Walsh.

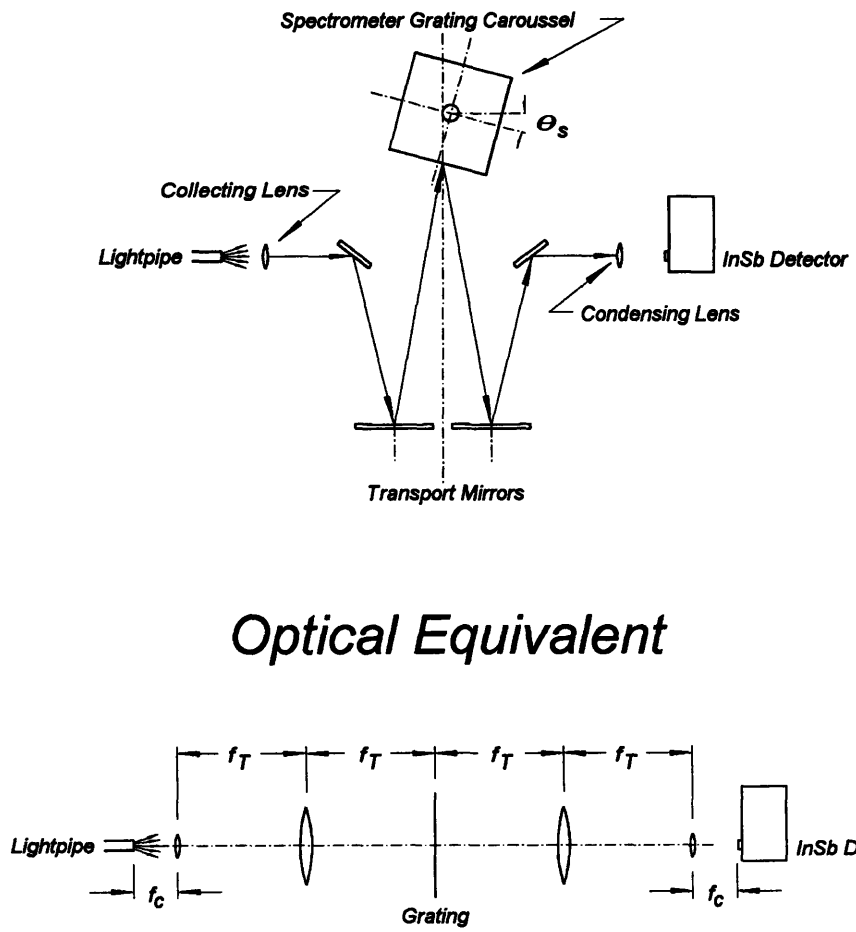

FIGURE 5-5. The Czerny-Turner spectrometer and its optical equivalent. f_T is the focal length of the transport mirrors, and f_C is that of the collecting and condensing lenses. Collimator slits are placed adjacent to the collecting and condensing lenses.

measured by rotating the diffraction grating so as to pass a series of wavelengths through to the detector. The lenses were of spherical configuration, made of TPX*. The collection lens gathered emission from the lightpipe, which was placed in its focal plane. Collimator

* The lenses were made by K. Woods.

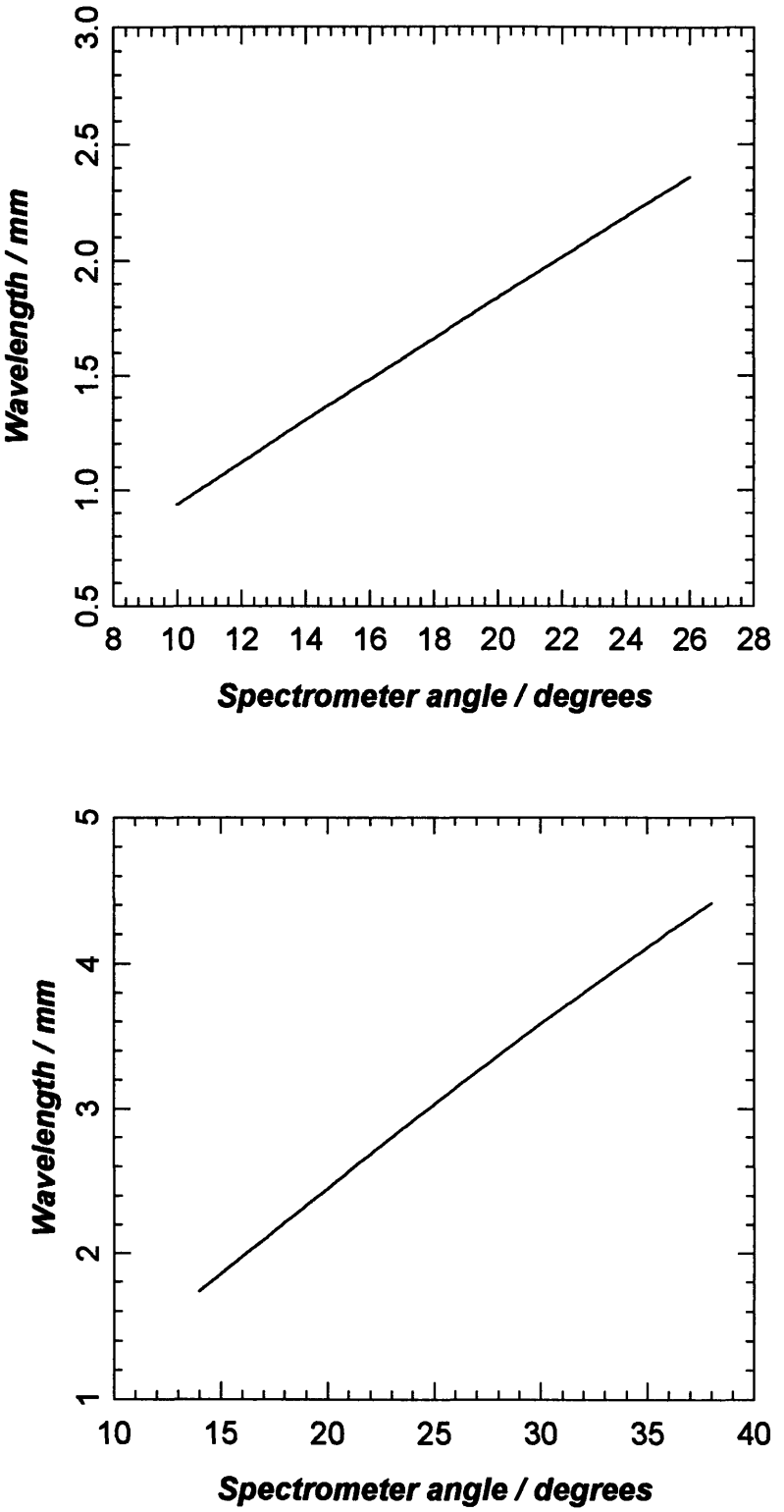

FIGURE 5-6. Calibration curves for spectrometer grating numbers 2 and 3 (top and bottom curves, respectively). The horizontal axes correspond to values of the angle θ_S of Fig. 5-5. The curves extend over the gratings' useful angular ranges. Grating #2 has a 10° blaze angle, and #3 a blaze angle of 20°.

slits were placed on the collection lens to reduce the angular acceptance of the spectrometer; since the diffraction grating effectively maps wavelength into angle, this narrows the spectral response of the spectrometer. The first transport mirror then images the lightpipe output onto the diffraction grating, which in turn disperses the light. The second transport lens conveys the dispersed image to the condensing lens, with its collimator slit. The condensing lens images the output onto the InSb cryogenic detector (see Sec. 5.4). Alignment of the spectrometer was accomplished with a HeNe laser.

Figure 5-6 shows angle vs. wavelength curves for spectrometer gratings 2 and 3. These are calculated, not measured. However, the calculation depends only on the spectrometer geometry and the diffraction grating period, along with the diffraction grating equation for first-order diffraction

$$\lambda_{diff}(\sin\theta_i - \sin\theta_f) = \lambda, \tag{5.3}$$

where as usual the radiation wavelength is λ; λ_{diff} is the diffraction grating period, and θ_i and θ_f are the incident and diffracted ray angles with respect to the normal. These dimensions are accurately measured, so the calculation legitimately serves for calibration.

In the spectroscopy studies of Chapter 6, it will be important to know the spectrometer lineshape, since the measured spectral profiles consist of the convolution of the spectrometer lineshape with the actual spectral profile. In the geometric optics limit, the spectrometer lineshape is the convolution of the image of the input slit with the output slit's "transmission function" (*i.e.*, 100% transmission within the slit width, and zero outside). Since the input slit image is also "flat" (*i.e.*, flat power density over a region of extent equal to the input slit's width), the spectrometer lineshape is then triangular in shape (sharply peaked in the center, rolling off linearly to zero on either side). The FWHM of the lineshape, in terms of spectrometer grating rotation angle, is

$$(\text{FWHM}) = \frac{w}{2f_{trans}} = 0.54° \qquad (5.4)$$

for a collimator slit width w = 12 mm. From the wavelength vs. angle calibration curve of Fig. 5-6, we see that for spectrometer grating 3, this angular FWHM corresponds to a wavelength FWHM of 0.072 mm. Grating #3 was used to measure wavelengths between 2 and 4 mm, so that the mean fractional resolution of the spectrometer with 12 mm slits was of order 2%.

Geometric optics was inadequate to explain the spectrometer lineshape in situations where the collimator slits produced discernable single-slit diffraction. The collimator slits used were of widths 12 and 25 mm. We observed Smith-Purcell emission of wavelengths as great as 7 mm. Moreover, 9 mm emission produced by another type of interaction was also observed. Significant diffraction occurred in these circumstances. The diffraction had the ultimate effect of broadening the spectrometer lineshape for long wavelengths.

Lineshape broadening occurs when the single-slit diffraction pattern from the input slit is significantly truncated by the transport mirrors. The input slit image presented to the output slit is the truncated diffraction pattern's inverse Fourier transform, which is just the convolution of the undistorted slit image with a sin(x)/x function of full width ($f_{trans}\lambda/2r_{trans}$), where f_{trans}= 67.3 cm is the transport mirror focal length, r_{trans} = 10.2 cm is the transport mirror radius, and λ is the emission wavelength. For λ = 9 mm, the "smearing" sin(x)/x function is of width 30 mm, a value larger than the largest slit width employed. Clearly, the resulting lineshape must be significantly broadened relative to the short-wavelength lineshape. Figure 5-7 shows a plot of the measured spectrometer lineshape using 8.8 mm wavelength radiation with 12 mm collimating slits. The data fit the

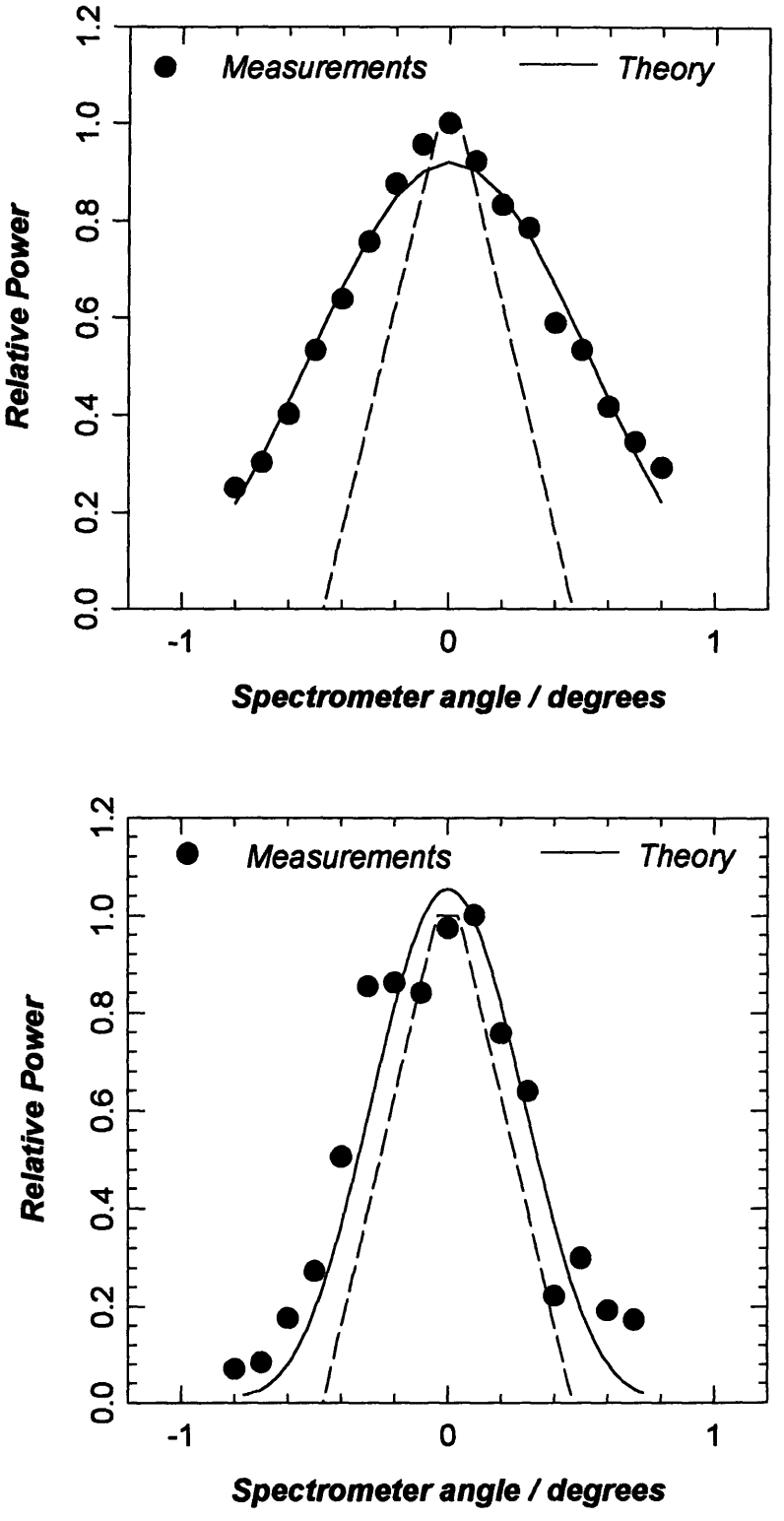

FIGURE 5-7. Spectrometer lineshape data and theory for 12 mm collimation slits. Top figure: 8.8 mm radiation, measured and theoretical results. Bottom: 2.4 mm radiation, measured and theoretical results. Both graphs also show a plot of the lineshape in the short wavelength limit (dotted line).

diffraction theoretical lineshape very well, and the measured lineshape is indeed much broader than the geometric optics theoretical lineshape also plotted for comparison. Figure 5-7 also shows a measured lineshape with 12 mm collimator slits and 2.4 mm radiation, along with the geometric optics theoretical lineshape. The measured lineshape is rather closer in width to the geometric optics limit than is the long-wavelength case.

5.4 The InSb electron bolometer detector

We used a cryogenic InSb detector to measure the power of the mm- and sub-mm-wave emission observed in the experiments of Chapter 6. The radiation is directed onto the InSb crystal, which is cooled to liquid helium temperatures inside a cryostat of roughly 75 cm height and 20 cm dia. Electrons are excited to the conduction band by the radiation, which results in a decrease in the resistance of the crystal. The relaxation time for the excited electrons is about 300 nsec; thus, the detector integrates radiation pulses of duration shorter than 300 nsec. A 5V source drives current though the detector crystal and a resistor connected in series with it. The crystal's resistance decrease is registered as a voltage change across the series resistor. Figure 5-8 shows plots of "typical" voltage traces from the InSb detector. The voltage pulse is AC-coupled to an amplifier system with a designed rolloff at around 3 MHz, a bandwidth compatible with the crystal's electron relaxation timescale of 300 nsec mentioned above. Consequently, no temporal structure in the radiation pulses beyond that bandwidth could be resolved.

The radiation pulses were much shorter than 300 nsec for all wavelengths we observed. Radiation pulse duration in this experiment is a function both of the electron pulse duration and the emission direction. For a single electron, it is easy to show that the pulse duration is given by (see Sec. 1.2.1):

$$\tau_{pulse} = \frac{L}{c}(\frac{1}{\beta} - \cos\theta) \qquad (5.5)$$

where L is the interaction (*i.e.* grating) length, βc is the elctron's velocity, and θ is the angle of emission. The duration of a radiation pulse due to an electron bunch is approximately by the sum of the single-electron pulse duration and the electron pulse

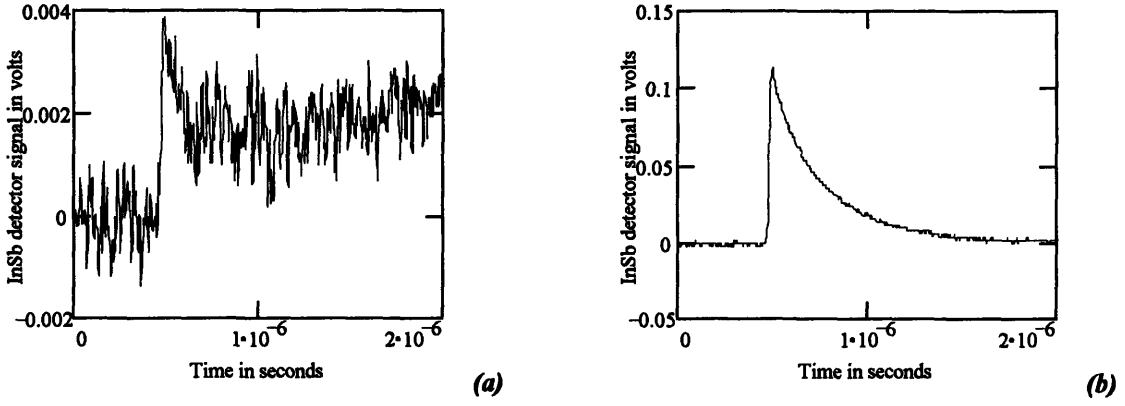

FIGURE 5-8. Oscilloscope traces of voltage signals from the InSb detector. Trace (a) is an example of a modest-to-small signal with typical SNR; (b) is an example of a large signal. The signal maximum is obtained from a nonlinear least-squares fit of an exponential function to the trace. Signal maxima are shown in plots of spectrometer and grating scan data (see Sec. 5.6).

duration. Table 4-1 of the previous chapter details the characteristics of the ATF electron beam: the electron micropulse duration in explosive emission mode (see Sec. 4.2) is of order 20 psec. The range of radiation micropulse durations on our detector was then (20 psec $\leq \tau_{pulse} \leq$ 0.6 nsec). None of the radiation micropulse temporal structure could therefore be resolved by our detector.

Fig. 5-9 displays power as a function of detector output voltage; this calibration was determined by previous workers [Price, 1991]. This curve is only valid in the long-pulse limit where the pulse duration is much greater than 300 nsec. The following relation

can be used to estimate the average power for very short pulses, when the pulse length $\tau_{short-pulse}$ is known:

$$P_{short-pulse} = P_{long-pulse} \cdot \left(\frac{\tau_{short-pulse}}{300 \text{ nsec}} \right)^{-1}, \tag{5.6}$$

where $P_{long-pulse}$ is the nominal power from the calibration curve corresponding to the detector output voltage. This estimate is based on the notion that the measured power is roughly the instantaneous power averaged over the electron relaxation time of 300 nsec (the relation can be obtained formally by employing a reasonable impulse response function for the InSb crystal, and assuming the short-pulse duration is much less than 300 nsec).

5.5 Data collection and experimental control

In this section I describe the means by which computer control was employed to remotely operate actuators in the beamline apparatus, store data, and orchestrate the activities of experimenters during performance of measurements. I designed and constructed the computer interface hardware (not including the A-D/digital output board installed in the IBM-compatible PC control computer), and wrote the ~3000-line Pascal experimental control program.

Figure 5-10 depicts the experimental control system. The experimenter controlled the actuators (see Sec. 5.2.2) to control the collection mirror position, vertical grating position, and lateral grating position via a computer interface. A digital output board installed in the control computer controlled four TTL outputs, which drove a relay box via the isolator box. The relay box contained a network of relays with DC amplifiers to boost the TTL signals to 12 VDC for energizing the relays' solenoids. The four TTL outputs

performed the following control functions: bit 0 turned the selected device on/off; bit 1 set the selected device's direction; bits 3 and 4 selected the desired device. The relay box also contained a FET switch network, operating in a fashion completely analogous to the relay network (using bits 2 and 3 of the TTL control inputs), to selectively connect the digital multimeter to the position-sensing potentiometer (see Sec. 5.2.2) of the device being operated.

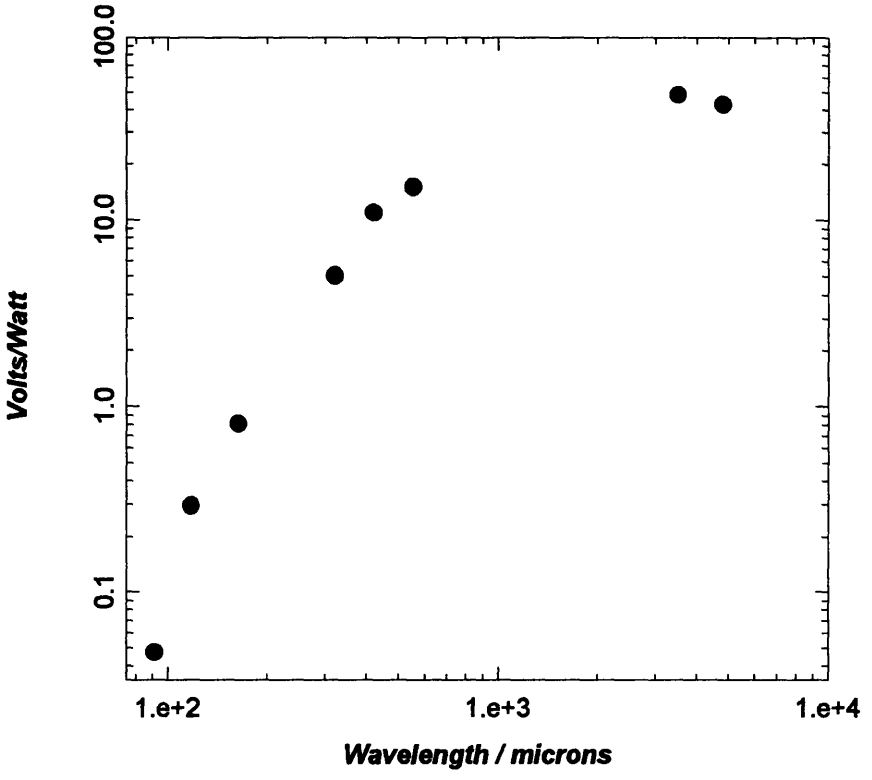

FIGURE 5-9. The InSb liquid helium-cooled detector calibration curve (from [Price, 1991]). Most of our measurements were made at greater than 1mm wavelength.

The computer was provided with position information for the three devices via an analog output of the digital multimeter, which was sensed by the A-D converter. In addition to the mechanical limit switches for the actuators, software position checks were also performed for safety purposes. The computer could select a device and move it through a displacement specified by the experimenter in convenient units (*i.e.*, mm or

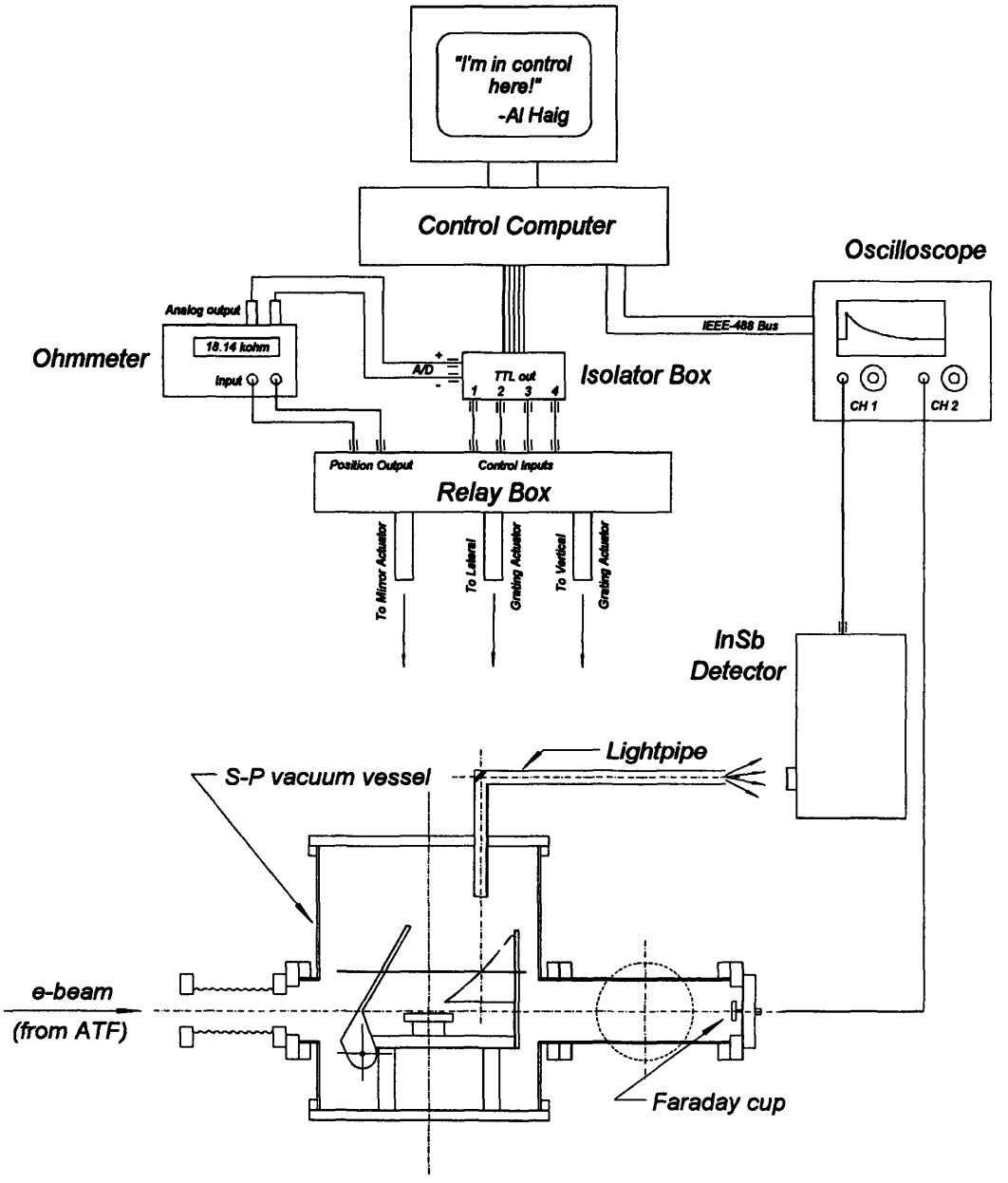

FIGURE 5-10. The Smith-Purcell experiment data collection and experimental control system. The control computer ("Haig") orchestrated the activities of both electrically-driven and experimenter-driven actuators, and retrieved and stored traces from the oscilloscope. The spectrometer was placed between the lightpipe and the detector, but is not shown here (see Fig. 5-5).

degrees), and then report a position indicated by the device's position-sensing potentiometer.

The spectrometer was not equipped to be computer-controlled. It was actuated by an experimenter via a rotary drive cable connected to an electric hand drill. The position was monitored by the experimenter by means of a vernier scale on the spectrometer carrousel.*

Charge data from the Faraday cup and radiation data from the InSb detector were acquired by a Tektronix 2731L digital storage oscilloscope. The data were then transferred to the hard drive of the control computer via an IEEE-488 bus for storage. The scope trigger was obtained from the Faraday cup signal. This was a reasonable approach insofar as the Faraday cup signal was easy to acquire, and was synchronous with the radiation signal. The computer could also issue instructions to carry out sequences of measurements, while exerting control over the beamline apparatus actuators. We typically measured radiation and charge signals over either a range of wavelengths, with fixed collection system orientation (spectroscopy), or a range of vertical grating positions at fixed wavelength (beam-grating coupling). Experimenters were required to operate the oscilloscope, and inform the computer when a measurement requested by it (e.g., radiation and charge signals at a given spectrometer or grating position) was completed. Upon completion, the computer would advance the grating position or request an experimenter to advance the spectrometer position. The process would be repeated until the desired grating position or wavelength range was examined. A sequence of data files, each containing an oscilloscope trace, was saved on the computer for subsequent analysis. As a

* Not surprisingly, the post of "spectrometer driver" was not eagerly sought after. In addition to the exacting, but repetitive and tedious nature of the job, one was positioned so that it was impossible to see the oscilloscope screen. One was reduced to attempting to discern results through the facial expressions of one's colleagues.

backup measure, experimenters also recorded peak charge and radiation signals by hand. In addition to having a backup representation of the data in a form invulnerable to magnetic fields, hard disk failures, etc., the handwritten journal also served as a useful record of a day's run.

Other less formal measurement regimens were also employed, particularly in the early stages of the experiment. These will be described in the next section.

5.6 Experimental procedures and techniques

In this section I describe the methods by which the principal results of Chapter 6 (the beam-grating coupling study and the spectroscopy study) were obtained, using the apparatus discussed in the previous sections.

5.6.1 Informal techniques

"Sanity-check" methods must be applied at the outset of any experiment to assure the genuineness of the first signals acquired. The simplest of these is the on-off test: the signal must be extinguished when the lightpipe is blocked. Convenient filters like wet paper towels (transparent to cm-waves but opaque to mm waves), glass, and metal mesh filters derived from machine shop scraps, were employed to good effect in the early stages. Of equal simplicity, but capable of surprisingly good quantitative wavelength measurements, are polyethylene cross-polarized diffraction filters [Kimmett p.113]. These consist of a pair of transmission gratings placed together with their rulings oriented perpendicular to one another. Wavelengths much longer than the grating period pass unimpeded, since the phase modulation induced by the gratings is small; wavelengths equal to or less than the grating period experience significant phase modulation and concomitant diffraction, thus reducing power transmitted to the detector. They act as a

low-pass filter (in frequency terms), with ~50% attenuation of wavelengths equal to their grating period. These filters were employed prior to the commissioning of the Czerny-Turner spectrometer, and afforded us our first verification of the presence of Smith-Purcell emission.

5.6.2 Spectrometer scans

The purpose of spectrometer scans was to measure spectral power density of Smith-Purcell emission. Figure 5-11 illustrates the Smith-Purcell interaction in the beamline apparatus and the coordinate system and variables used to describe it. As mentioned in the previous section, there were two principal measurement methods. One involved scanning the vertical grating position, the other scanning the spectrometer. When scanning the spectrometer, the collection system and the grating are static, and one surveys the spectral content of the emission coming out of the lightpipe. Since the grating position is static, the charge measurement would ideally register a constant value; deviations in the charge measurements from constancy thus serve as a record of the shot-to-shot beam stability and longer-term beam drifts. During a spectrometer scan, the grating was vertically positioned to maximize the signal (see Fig. 5-11). This tactic served two purposes: maximization of the signal-to-noise ratio, and the reduction of radiation signal fluctuation due to shot-to-shot vertical steering jitter. The latter benefit occurs because the derivative of the radiation signal as a function of vertical grating position, and therefore vertical *beam* position, is nearly zero at the vertical grating's maximum signal position.

As it turned out, for typical beam sizes and emission wavelengths, the beam was partially blocked by the grating during spectrometer scans (the grating was at ground potential, thus the charge intercepting the grating was not measured). Therefore, shot-to-

shot jitter in the charge measurements could occur because of charge jitter, steering jitter, or both. In the explosive emission mode of injector operation, steering jitter was not a serious problem for two reasons: the incident spot on the cathode of the explosive-emission-inducing laser varied little in the position of its incidence; and the steering sensitivity of explosive emission to the spot position was not great. Shot-to-shot variation in the charge measurements was therefore ascribed principally to charge jitter in explosive emission mode. In photocharge mode, however, the cathode laser spot position variations were greater than in explosive emission mode, and the steering sensitivity of photoemission to spot position variations was larger. Consequently, steering jitter played a larger role in photoemission measurements than in explosive emission measurements.

To reduce the effect of shot-to-shot jitter, we typically averaged over 16 shots at a given spectrometer setting. Since the injector was typically run at 1 1/2 - 3 Hz, shot averaging was not time-prohibitive. In fact, more time was consumed in repositioning the spectrometer and transferring data from the oscilloscope to the computer than was taken to acquire the data. A spectrometer scan was typically 10-20 points, and with data transfer and spectrometer control overhead included, this typically took about 15 min. to complete. The spectral range to be scanned was determined by first identifying the desired nominal center wavelength, and then moving the spectrometer in either direction until the signal was reduced to just above the noise level. The spectrometer lineshape was typically either 0.5° or 1° in width (see Sec. 5.3), so that spectrometer angle increments of 0.1°-0.25° were normally used.

5.6.3 Grating scans

The goal of the grating scan measurements was to deduce the beam density variation in the vertical (y) direction. It must also be mentioned that the grating scan measurements indicate that emission from a single charge is a monotonically decreasing function of its height above the grating. At the time of this writing, analysis of data collected to date is being carried out to determine the exponential attenuation length consistent with the consistently observed monotonic decrease. A grating scan measures the radiation and charge signal dependence on vertical grating position. This section describes the grating scan method and presents some typical data.

The principle of the grating scan was to simultaneously measure the charge and radiation signal as a function of vertical grating position, with the collection mirror and

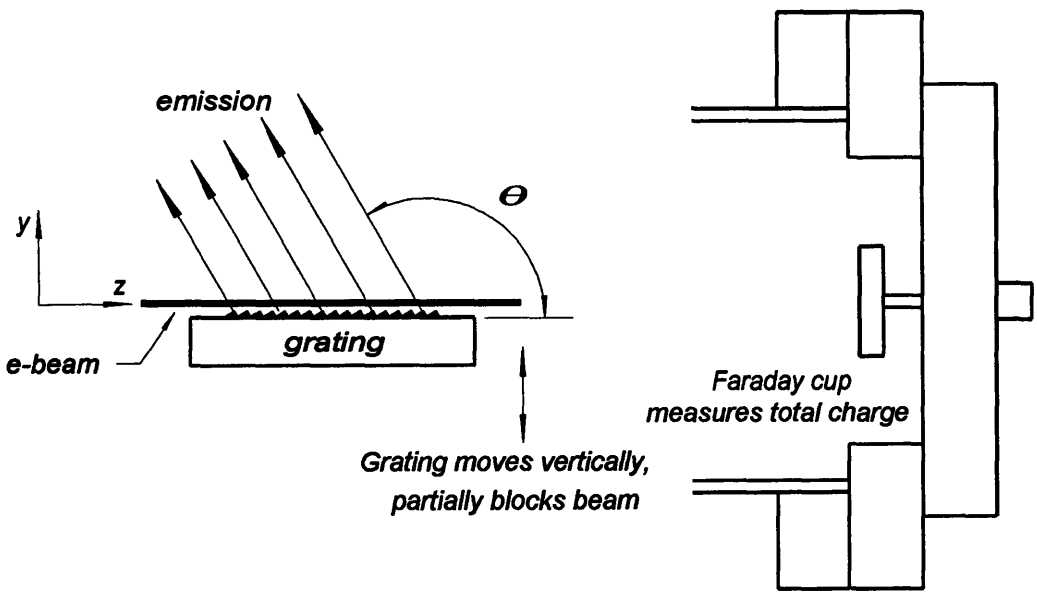

FIGURE 5-11. Coordinate system for describing the Smith-Purcell effect. The x-direction is into the paper. The grating and the electron beam diameter are shown in correct proportion. The beam diameter is about 1.5 mm. θ is the Smith-Purcell emission angle. Also shown is the Faraday cup (shown closer to the grating than in the actual system). The grating was moved vertically, and typically would partially block the electron beam. The grating was electrically grounded.

spectrometer fixed. The grating partially blocked the beam during these measurements to varying degrees (see Fig. 5-11), so that the charge measurement determined the amount of charge that was *not* intercepted by the grating, and then arrived at the Faraday cup. Unlike the spectrometer scan charge data, which in principle would remain nominally constant during the course of a measurement, the grating scan charge data could *not* serve to monitor the shot-to-shot stability. The data did, however, provide the integral of the transverse beam charge profile as a function of the grating surface vertical position y:

$$Q(y) = \int_{y}^{\infty} dy' \left(\int_{-\infty}^{\infty} dx' \varphi(x', y') \right). \tag{5.7}$$

Here, $\varphi(x,y)$ is the transverse density profile of the electron beam (see Sec. 6.3.3). As it turns out, beam steering and emittance effects complicate matters, so that eqn. (5.7) is an excessive simplification, because the transverse (i.e., (x, y)) profile was a function of z. In any case, the advantage of a stability monitor is partially lost, since it is not possible to completely distinguish between systematic variations and $\sim 10^0$ min. timescale drifts of the electron beam. This problem could have been circumvented by collecting and monitoring the charge incident on the grating, as well as that on the Faraday cup (see Fig. 5-11), so that the total beam charge would be measured.

Figure 5-12 presents a plot of charge and radiation power measurements from a typical grating scan. The charge signal grows smaller with increasing grating surface vertical position y because an increasing portion of the beam is being blocked by the grating. The radiation signal, however, grows with y for a while even though the charge is being reduced, because the remaining charge is closer to the grating surface and hence causes more emission per charge. Finally, the loss of charge dominates and the radiation and charge signals are both extinguished with the total blocking of the beam.

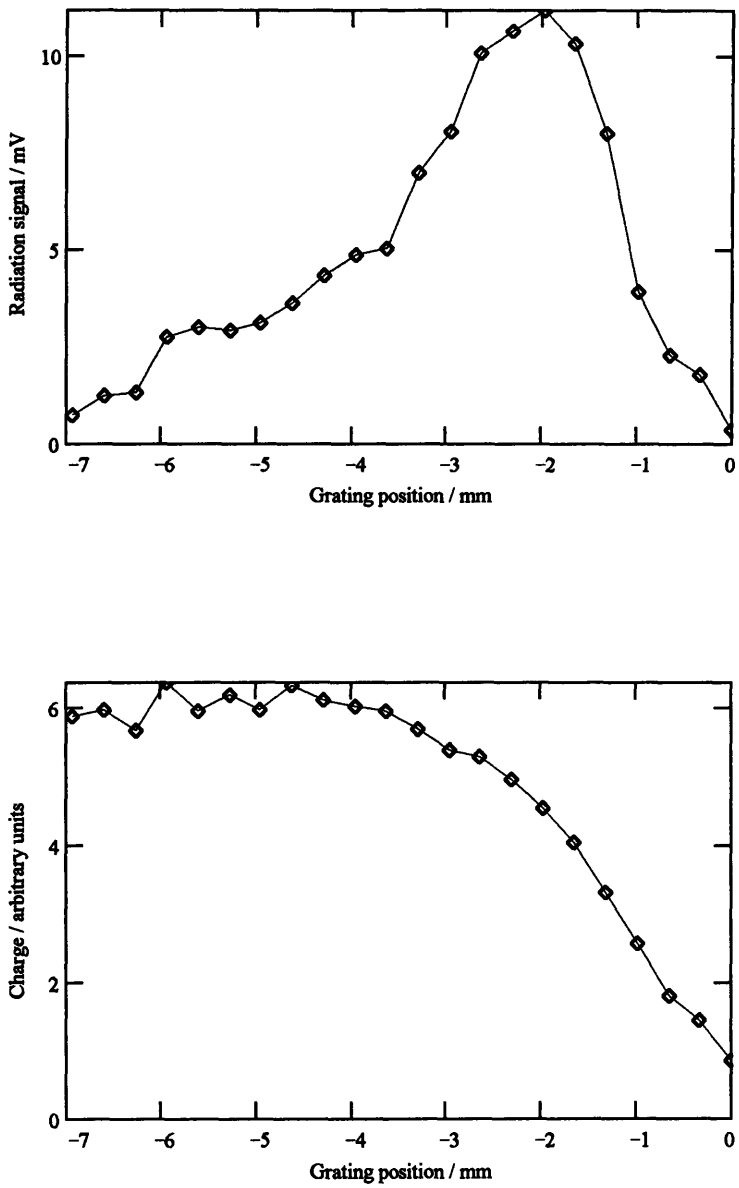

FIGURE 5-12. Radiation power and charge as a function of grating height *y*.

I earlier concluded that shot-to-shot jitter in the measured charge was primarily due to fluctuations in the total charge, rather than steering fluctuations. The charge signal plot of Fig. 5-12 bears this out; large fluctuations occur when the charge signal is large and when beam blockage is minimal. Were steering jitter the cause, the fluctuations would

be small when beam blockage is minimal (i.e., large charge signals), and large when blockage is significant (i.e., small charge signals).

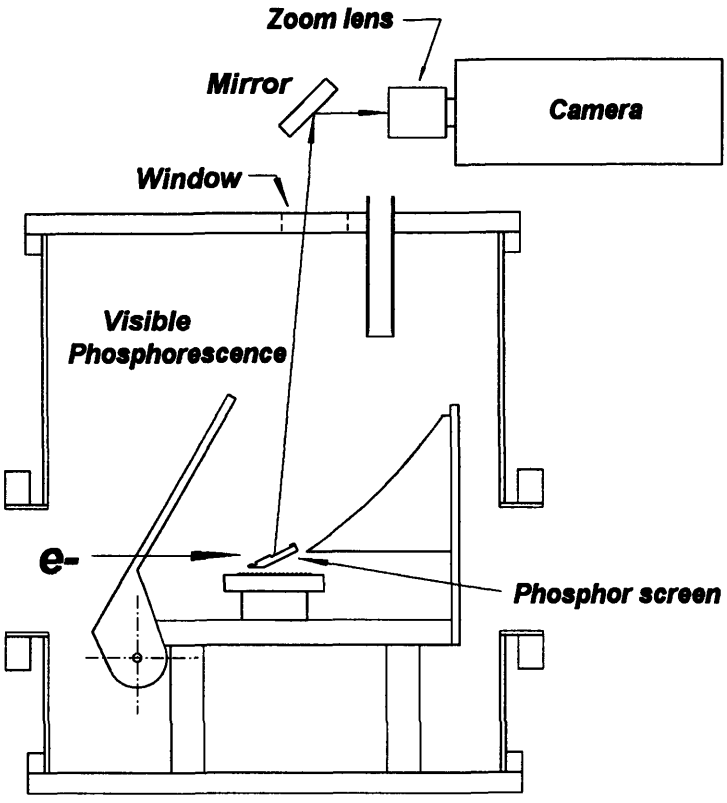

FIGURE 5-13. The transverse beam profile viewing system.

5.6.4 Electron beam diagnostic: measuring the spatial distribution of the electron beam

In addition to the spatial distribution information provided by the grating scan technique of Sec. 5.6.3, we made direct observation of the beam profile by placing a phosphor screen in the path of the electron beam. The phosphor screen was viewed by a video camera placed outside the vacuum vessel. Figure 5-13 depicts the system for viewing the phosphor screen. The video image was then studied with a SPIRICON LBA-100A beam profile analyzer. Figure 5-14 is a contour plot of the transverse electron beam profile. Size calibration is obtained through known separations of identifiable features of

the phosphor screen upon which the beam is imaged. These images are used to analyze the beam-grating coupling data of Chapter 6.

The resolution of the beam viewing system was limited by an inadequate zoom lens; only a (20 x 20)-pixel subset of the (120 x 120)-pixel SPIRICON image was occupied by the beamspot. Nevertheless, the overall shape and size was adequately captured.

5.6.5 Ratio measurements: an application of the grating scan technique

There is a simple but powerful application of the grating scan technique of Sec. 5.6.3. As mentioned earlier, a system was installed in the interaction region permitting the alternate use of two different gratings, without having to break vacuum. Only about three minutes was required to change from one to the other installed grating. Comparative assessments of the emission from the two gratings could be made, since the beam was stable over such timescales.

Comparisons of emission from two gratings at a single wavelength and emission angle are independent of the beam geometry, the collection system response, the spectrometer transmission and spectrometer grating efficiency, and the detector wavelength response characteristics. This is significant because all of these effects are difficult to account for. One simply carries out grating scan measurements from each grating in turn, without changing the collection system or the spectrometer orientation. The two measured charge density profiles, and the two emission power profiles, are then least-squares fit to one another with two free parameters, a ratio and a vertical position offset. The latter is required to allow for the fact that the two gratings' heights might not be identical. The ratio R of the emission from the two gratings can then be written

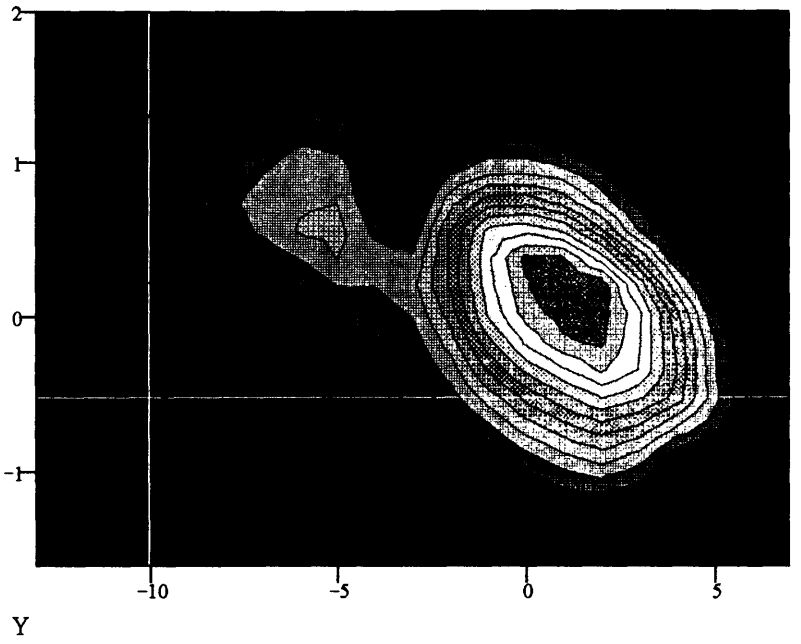

FIGURE 5-14. The transverse profile of the electron beam. The contours are curves of constant electron density. The standard deviation of the Gaussian fit to the vertical density is about 600 microns. Distance units shown on axes are mm. The relative smoothness of the profile is due to undersampling.

$$R = \frac{\{\text{Emission power ratio from least - squares fit of the emission data sets}\}}{\{\text{Charge ratio from least - squares fit of the charge data sets}\}} \qquad (5.7)$$

The charge ratio is incorporated to compensate for possible drifts in the beam state. The uncertainty in R can be estimated from the variances associated with the two least-squares fits from which it is derived. Such a measurement should attain high precision (<1 part in 10^{-2}), since approximately 80 individual measurements are averaged to obtain it. Moreover, such precision could be obtained under accelerator operating conditions where the beam is stable for times as short as 15 min. There are some intriguing measurements that could be performed:

- Comparison of emission power at a given wavelength from two gratings of the same period and different surface profiles, from any emission order.

- Comparison of emission power at a given wavelength from two different emission orders. This is achieved as follows: for example, suppose grating 1 has period λ_G, and grating 2 has period λ_G/n, where n is an integer. At a given emission angle, the nth order emission from grating 1 has the same wavelength as the 1st order emission from grating 2. The gratings could have geometrically similar profiles, or different profiles.

- Comparison of emission power at a given wavelength from two gratings of the same period and surface profile, but made of different metals with different *conductivities*. These measurements could be very important in understanding conductivity effects in Smith-Purcell emission at very high frequencies.

The first two comparisons would provide very high precision checks of the van den Berg theory that could be performed over a very wide range of emission wavelengths- - not restricted to particular spectral features as the experiments of Chapter 6. The latter comparison would be quite novel because it defies analysis by the currently available theories of Smith-Purcell emission [Haeberle *et. al.*, 1994].

A caveat: while the above measurements are indeed a *direct* comparison of the spectral profiles, the comparisons are of the spectral profile integrated over the collection system response times the spectrometer lineshape function. The spectrometer lineshape function must be made narrow compared to the characteristic width of structures in the spectral profiles- else much of the simplicity of the technique is lost, since then the spectral transfer functions must be accounted for in the comparison.

Unfortunately, I hadn't opportunity to carry out any of these measurements, but hope that my colleagues see fit to do so. High-precision results, coupled with ease of data acquisition and analysis, ought to exert an irresistable attraction.

CHAPTER 6

SPECTRAL PEAKING IN THE SMITH-PURCELL EFFECT

6.1 Introduction

In this chapter I present the results of an experimental investigation of the Smith-Purcell effect, performed at the Accelerator Test Facility of the Brookhaven National Laboratory. I observed sharp peaks in the Smith-Purcell emission frequency spectrum that have never before been observed experimentally. Their existence was first predicted by Hessel [Hessel, 1964]. Calculations based on the van den Berg theory [van den Berg, 1973] also predict these peaks. The theory also asserts that these peaks are not expected to occur in emission induced by non-relativistic or mildly relativistic electrons (50-100 keV) [Haeberle *et. al.*, 1994]. The existence of strong emission at certain favored angles is of obvious and critical importance to using Smith-Purcell emission as a source for FIR spectroscopy. Likewise, a FEL in the far infrared based on relativistic Smith-Purcell emission might employ a geometry to exploit these favored emission angles.

A clever dispersion diagram construction can be used to estimate where this peaking occurs [Hessel, 1964], as will be discussed in Sec. 6.3.1. The peaks result from a process that can be thought of as an "inverse Wood anomaly". A Wood anomaly [Wood, 1935] is a diffraction rating effect wherein a propagating wave incident upon a grating excites a surface mode that propagates parallel to the grating surface, and which carries no energy away from the grating. This process is reversible; parallel-propagating waves can diffract into radiating modes. Such parallel-propagating waves can be excited by electron-beam-produced evanscent waves (see Appendix 1), and result in strong emission. In any case, a comprehensive theory like that of van den Berg is needed to predict the shape, width, and precise location of the spectral peaks, but it is interesting to note that their location can easily be approximately determined. Our spectral measurements establish the

existence and location of one of these spectral peaks, and determine the FWHM of the peak. The 30° blaze gratings used have broad peak structures; the wings of two particular peaks overlap to produce a distinct spectral feature, which I call a dip. The position of this dip is determined by the widths of the peaks on each side of it. Since it is an artifact of the finite linewidths, its existence or position cannot be predicted with a simple geometric construction, as is the case with the peaks- a comprehensive theory taking into account the grating surface geometry is required for its description. Thus, the observation of this dip feature is just as valuable a test of a comprehensive theory as the FWHM measurement. As stated in Sec. 1.1, the combined use of large-period gratings and relativistic electrons has enabled me to carry out the most precisely controlled investigation to date of the Smith-Purcell effect. I show in this chapter that these precise spectral measurements agree very well with the theory of van den Berg.

Section 6.2 summarizes the considerations to be accounted for in the comparison of the van den Berg theory with experimental results. Section 6.3 describes the simple construction for deducing wavelengths at which emission peaks occur, and relates the emission peaks to Wood anomalies. The spectral measurements, and concomitant data analysis, are also presented in Section 6.3. Summary and conclusions are given in Section 6.4.

6.2 Relating theory and experiment

In this section, I summarize the analytical framework for comparing the spectroscopy measurements of Sec. 6.3 to the predictions of the van den Berg theory. A detailed discussion has been relegated to the Appendices . I discuss here the effects of the two spectral transfer functions, the spectrometer and the collection system, that must be accounted for in analysis of the measurements.

In any experiment involving the study of any emission process, the geometries of both the emission source and the emission collection system must be accounted for to compare experimental results to theory. This accounting is complicated in the case of Smith-Purcell emission by the correlation between wavelength and emission angle. I have already discussed the collection system in Sec. 5.2.3. Its angular acceptance is equivalent to a set of wavelength acceptance curves for the various emission orders. An emission *order* in Smith-Purcell emission is analogous to that for grating diffraction. The wavelength of emission order n is given in Appendix Sec. A1.3 by

$$\lambda_n(\theta_n) = \frac{\lambda_G}{|n|}\left(\frac{1}{\beta} - \cos\theta_n\right). \tag{A1.16}$$

As already mentioned, the collection system acts in a fashion analogous to a spectrometer; it introduces to measured spectra a spectral transfer function of equal influence to that of the spectrometer lineshape function discussed in Sec. 5.3. The use of a spectrometer is required, however, to verify that the emission being observed is Smith-Purcell emission. The spectrometer also enables discrimination between Smith-Purcell emission orders accepted by the collection system.

The collection system model of Sec. 5.2.3 accounts for both the source and collection geometries. The computer ray-tracing analysis of the collection geometry has already been described. The beam density distribution can be estimated from the electron beam measurements of Secs. 5.6.3 and 5.6.4, by a procedure described in detail in Appendix Sec. A2.3. Secs A2.1 and A2.2 show in detail how knowledge of the density distribution enables calculation of the emission intensity variation over the grating surface. Thus, in the collection system model, rays from various points on the grating are weighed according to the calculated emission power at the given point, and the source geometry is

accounted for. I call the collection system response function $C(\theta_n, \theta_c)$; it is proportional to the emission energy per collection angle increment $d\theta_n$ accepted from emission order n, with the collection system set at a nominal acceptance angle of θ_c. Direct measurement of the $C(\theta_n, \theta_c)$ function is not possible without the use of radiation with emission-angle-dependent wavelength, the only easily available source of which was the Smith-Purcell emission I was trying to characterize. However, I was able to do just that (in a logically consistent fashion), and measure the FWHM of the collection system (see Sec. 6.3). For 1.4 mm-wavelength emission, the measured FWHM is 0.8±0.1 times that of the collection system response function model. This agreement shows the collection system model to be reasonably successful.

The other spectral transfer function, the spectrometer, can be more easily characterized empirically. Direct measurements of the lineshape were made, and they agreed well with computed lineshapes (see Sec. 5.3). I therefore use the calculated spectrometer lineshapes in comparing the measurements to theory.

Appendix 2 describes in detail how the spectrometer lineshape and the collection system response function are combined with the van den Berg theory to predict the results of experiment. This discussion requires defining the collection system response function in terms of nth order emission wavelength instead of emission angle:

$$C_n(\lambda, \lambda_c) \equiv C(\theta_n(\lambda), \theta_c(\lambda_c)) \qquad \text{(A2.29)}$$

For spectroscopy experiments performed over wavelength (angular) ranges whose extent is much less than the center wavelength (angle) of the range, the collection system response function's shape and amplitude remains essentially constant as the collection

system is scanned over the range. Under these conditions (fulfilled in the measurements of Sec. 6.3), the collection system response function can be written

$$C_n(\lambda,\lambda_c) \cong C_n(\lambda-\lambda_c)\,. \tag{A2.32}$$

The spectrometer lineshape function $\Sigma(\lambda_s-\lambda)$ can likewise be written in a similar form, since neither its shape nor magnitude varies appreciably over the range of wavelengths measured in Sec. 6.3.

Having accounted for beam and collection system geometry, and the effects of the spectrometer, all that remains is to combine those elements with the van den Berg theory. Sec. A2.5 defines the spectral distribution function $S_{n,\lambda}(\lambda)$ as the spectral power wavelength distribution function of the *n*th emission order (note that this function describes the emission of a single electron at zero height above the grating rulings- beam geometry has already been accounted for). The function describing the collected emission has the form of a double convolution of the spectrum with the collection system response and the spectral lineshape function:

$$W_{\text{collected, beam}}(\lambda_s,\lambda_c) \cong \int_0^\infty d\lambda \cdot S_{n,\lambda}(\lambda)\cdot C_n(\lambda-\lambda_c)\cdot \Sigma(\lambda_s-\lambda) \tag{A2.33}$$

This relation dictates the measurement strategy to be adopted, depending on the relative spectral width of $\Sigma(\lambda_s-\lambda)$ and $C_n(\lambda-\lambda_c)$ in the spectral region of interest. If the spectrometer lineshape function has width of the same order as that of the collection system response, one proceeds by acquiring a two-dimensional matrix of data $W_{\text{collected, beam}}(\lambda_s,\lambda_c)$ in the region of the (λ_s,λ_c) plane containing the spectral feature of interest. One can then integrate over one or the other of the variables (λ_s,λ_c) to obtain a

profile that is a single convolution in the other variable. This is the method of Sec. 6.3.2, and is described in more detail there. However, if the spectrometer lineshape is narrow compared to the collection system, and the collection system is broad enough to subtend

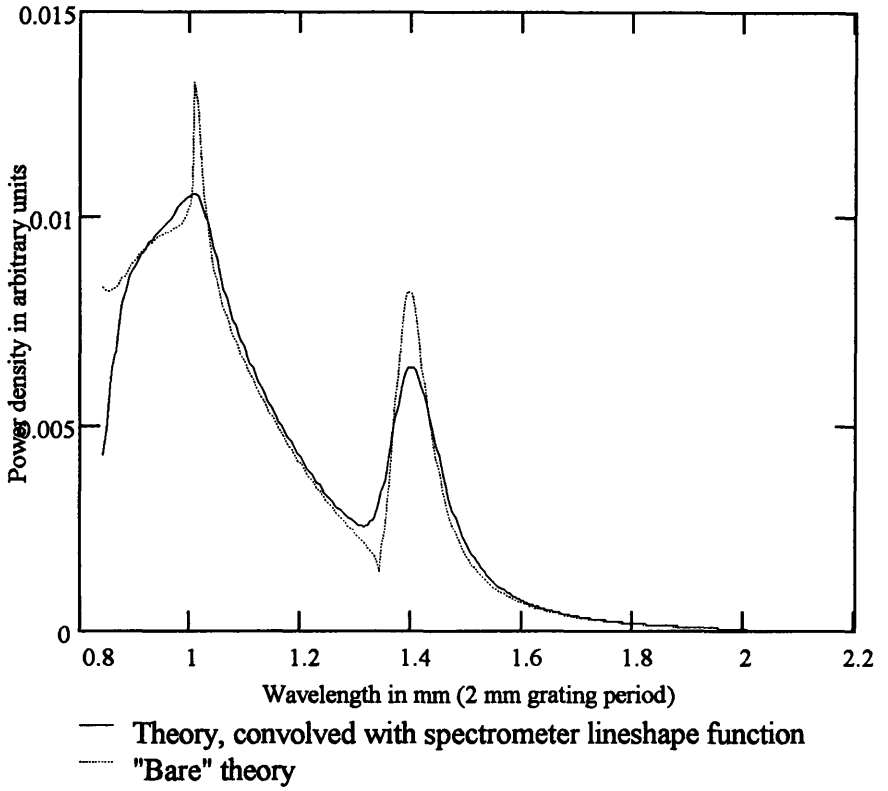

FIGURE 6-1. The van den Berg theoretical emission spectrum, with and without convolution of the spectrometer lineshape function. We studied the peak near 1.4 mm, and the dip just to its blue side. The dip results from the overlap of the shoulders of two adjacent broad peaks. The structure at 1 mm (90° emission angle) was not accessible to us because the collection system could not change from collecting forward to backward emission without a vacuum break.

the spectral feature of interest, then the spectral feature can be captured by a spectrometer scan. The scan must of course be performed at a collection system setting λ_c such that the collection system response encompasses the spectral feature of interest. This is the approach taken in Sec. 6.3.3.

6.3 Spectral peaks and dips

This section describes measurements of a second-order spectral peak feature emitted from a 30° blazed grating (see Sec. 5.2.4 for a description of the gratings), at an emission angle of about 113°. I also present measurements of a spectral dip in the emission from a grating of the same geometry. Figure 6-1 is a plot of the van den Berg theoretical emission spectrum from a 30° blazed grating*. For reasons to be explained below in Sec. 6.3.1, the peak feature is present in the spectrum of gratings of any blaze angle of modest value ($\theta_b \leq 40°$ or so). The peak is increasingly strong and narrow with decreasing blaze angle. In fact, one of the reasons we chose the 30° blaze is because the peak from this grating has structure broad enough to be discernable with the available spectrometer. Even a coarse assessment of its structure provides a comparison to the van den Berg theory's prediction of the peak's linewidth. However, a radiation source exploiting the emission peaks would most likely employ a grating with a blaze angle much smaller than 30° ; initial experiments with 5° blaze angle gratings are under way.

We measured the location of the peak structure from both a 2-mm and 4-mm period grating, the width of the peak structure from a 2-mm period grating, and the location of the dip structure from a 4-mm period grating. The results agree very well with the van den Berg theory. The peak is shown to occur at a fixed angle of emission for the gratings of two different periods. The peak measurements from the 2 mm period grating are presented and compared to the van den Berg theory in Sec. 6.3.2; peak measurements from the 4 mm period grating are given in Sec. 6.3.3. Sec. 6.3.4 presents the spectral dip measurements and theoretical comparison. Before presenting the data, however, I discuss in Sec. 6.3.1 the simple construction to compute the frequencies of emission peaks, and relate this construction to the phenomenon of Wood anomalies [Wood, 1935]. The

* These calculations were performed by K. Woods.

peaking phenomenon is described as an inverse Wood anomaly. This description was first offered by van den Berg [van den Berg, 1974].

6.3.1 Spectral peaking and Wood anomalies

A Wood anomaly is a grating diffraction phenomenon in which a propagating free-space wave incident on a grating diffracts into an evanescent mode bound to the grating and propagating parallel to it. The term "anomaly" is used because the efficiency of the diffraction grating is zero in this circumstance, since none of the radiation incident on the grating is re-radiated. The time-reversed process in which a bound mode is excited and then diffracts into a propagating mode is also allowed; such bound modes can be excited by the evanescent waves of an electron passing over the grating. Thus, Smith-Purcell emission at certain angles consists of exciting time-reversed Wood anomalies.

To see at what frequencies these resonances occur, I will derive the dispersion relation for bound grating modes propagating in the z-direction. The electric and magnetic field components of a bound mode can be written as the elements of a Floquet expansion, in the form

$$\Psi_{\text{bound},n}(y,z,t) \propto \exp(ikz - i\omega t)\cdot\exp(ik_n z - \gamma_n y). \tag{6.1}$$

where $k_n \equiv 2\pi n/\lambda_G$, and γ_n is real. The requirement that this satisfy the wave equation yields the dispersion relation

$$-(k+k_n)^2 + \frac{\omega^2}{c^2} + \gamma_n{}^2 = 0. \tag{6.2}$$

We cannot determine values of the γ_n's without employing boundary conditions, which of course requires specification of the grating surface geometry and conductivity. However, the special case of a flat plate "grating" yields $\gamma_n = 0$. Gratings with smooth features

having y-extent much less than the grating period should approach this limit. Figure 6-2 shows a plot of the dispersion relation (6.53) for various values of n, in the case $\gamma_n = 0$. Also shown is a plot of the line $\omega = \beta kc$, where β is the speed of an electron passing over the grating surface. Appendix Sec. A1.2 shows that the phase velocity of the electron's evanescent waves is also β. Intersections of this line with dispersion curves represent points at which the electron's evanescent modes are phase-coherent with bound grating modes and will thus couple strongly to them. Strong Smith-Purcell emission will then occur at the frequencies associated with these intersections.

The frequencies associated with the intersections, and their corresponding wavelengths, can be easily computed, and are given by

$$\omega = \frac{k_n c}{1+\beta} \Leftrightarrow \lambda = \frac{\lambda_G}{n}(1+\beta) \tag{6.3}$$

At this point, note that the intersection wavelengths are proportional to the grating period. Therefore, their Smith-Purcell emission angles are independent of grating period. The peak measured in this work corresponds to the $n=3$ case. The wavelength of the $n=3$ intersection, and the first and second-order emission angles, are then (for a grating period of 2 mm and a beam energy of 2.8 MeV)

$$\lambda_{n=3} = \frac{\lambda_G}{3}(1+0.9880) = 1.325 \text{ mm};\ \vartheta_{-1} = 69.5°;\ \vartheta_{-2} = 108.25°. \tag{6.4}$$

The 30° blaze grating used in this work deviates significantly from the flat-plate grating case, and thus its peaks are significantly displaced from the flat plate model values.

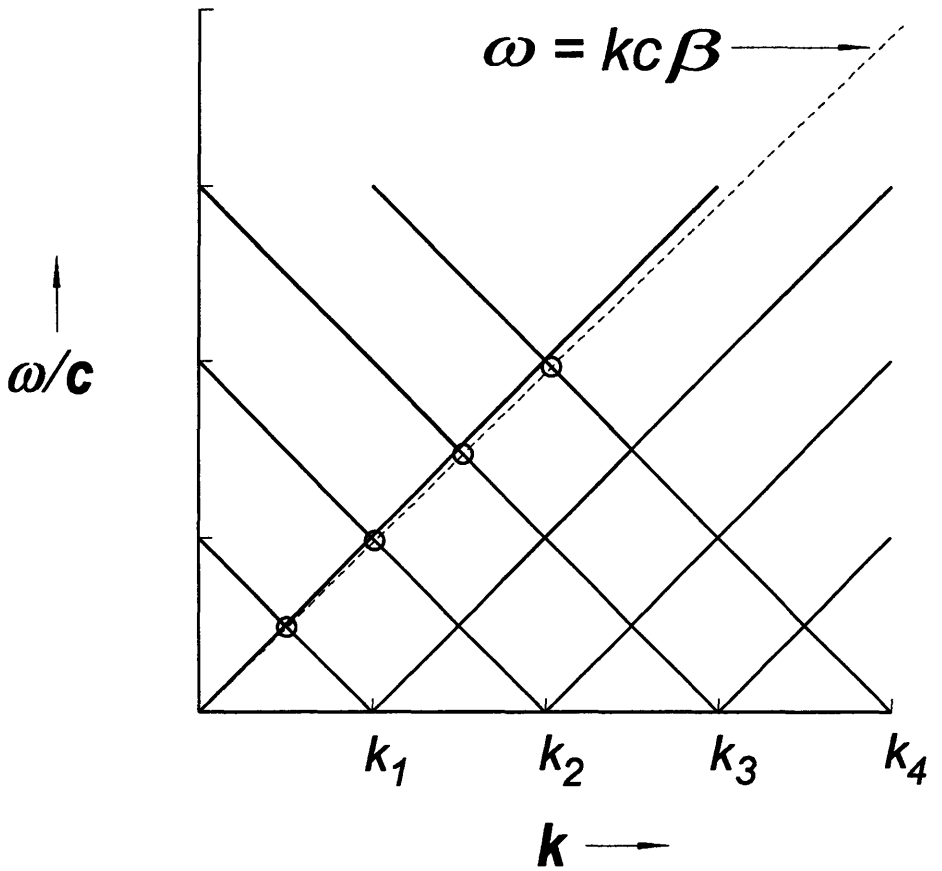

FIGURE 6-2. A plot of the flat-plate grating dispersion relation (eqn. 6.53). The circled intersections denote points at which electron evanescent waves match bound grating modes propagating parallel to the grating surface, along the *z*-axis. Here, $k_n \equiv 2\pi n/\lambda_G$. Also, note that the slope of the "beam line" $\omega = kc\beta$ is much closer to unity than depicted here for the beam energy used in the experiments of this chapter.

6.3.2 Measurements of a spectral peak: the 2 mm period grating

We obtained second-order emission measurements from a 30° blaze angle grating of period 2 mm, in the backward emission direction (i.e. the *z*-component of the emission's *k*-vector was in the opposite direction of the beam propagation). Measurement of a (6 x 7) matrix of values of the function $W_{\text{collected, beam}}(\lambda_s, \lambda_c)$ (defined by eqn. (A2.33)) over the ranges of wavelengths $(1.36 \text{ mm} \le \lambda_s \le 1.48 \text{ mm})$, $(1.27 \text{ mm} \le \lambda_c \le 1.48 \text{ mm})$ was performed in seven spectrometer scans. A nice overview of the measurements is provided by the contour plot of Figure 6-3. A peak feature is clearly discernable. Each of the signal

data was normalized to its corresponding total charge measurement, to reduce the effects of shot-to-shot charge magnitude jitter.

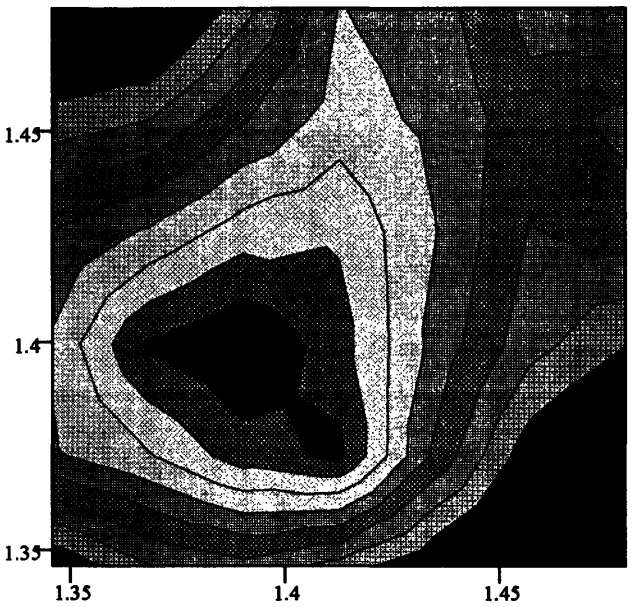

FIGURE 6-3. A contour plot of the measured double convolution of the spectrum with the collection system response (horizontal axis) and the spectrometer lineshape (vertical axis). Units are the nominal center wavelengths of the respective devices in mm.

The spectrometer scans were taken over a sequence of 7 collection system orientations, ranging over emission angles of 105°-118°. The scans are displayed in Figure 6-4. Shown with each spectrometer scan are the computed collection system response curves corresponding to the collection system setting for that scan. The "center" emission angle positions of the collection system response curves in their respective scans have all been offset by an angle of +1.9° (= 31 μm) from the nominal positions recorded at run time. That this was necessary was obvious at first glance of the collection system response curves with the data: moreover, there was sufficient uncertainty in the collection mirror angle calibration to realistically permit including an offset. The offset was determined by a least-squares fit of all the collection system response curves to their respective data; the parameters varied were amplitude factors for each collection system curve, and a single emission angle offset applied to all of the curves' central positions. The application of the offset does *not* affect either the peak wavelength or peak width measurement results, as will be seen shortly.

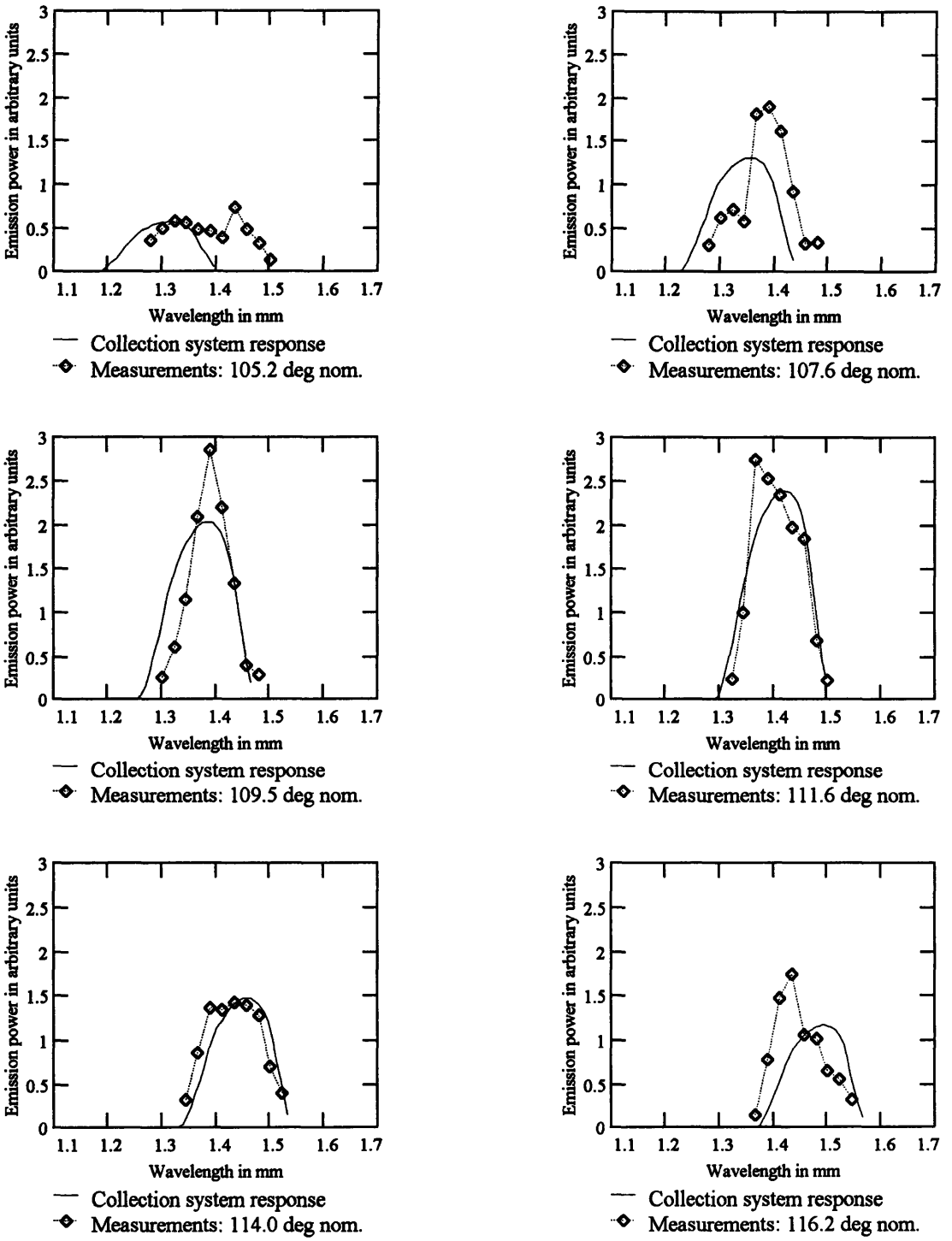

FIGURE 6-4. The spectrometer scan data for the peak measurement. The collection system acceptance angle for each scan is indicated (the indicated angles do not include the 1.9° offset referred to in the text). Plotted with each scan is its corresponding computed collection system response curve.

Some interesting observations can be made about the scans. First, the actual collection system response curves must be narrower than the computed curves shown. I say this because in none of the scans does the measured profile appear to be wider than the computed collection system response. Since the measured profile is the portion of the spectrum passed by the collection system, convolved with the spectrometer lineshape, the measured profile must be wider than the collection system response (I will presently remark further on the collection system response width). Second, that there is a peak is very clear when one examines the overall magnitude of the signal in the various scans (displayed in order of increasing wavelength). Moreover, the "center of mass" of the measured data in each scan is always shifted towards the direction of the peak, with respect to the collection system curve for that scan. Third, it is interesting to see what is in all likelihood the dip structure, in the scan with collection system setting of 108° (see Sec. 6.3.4). Unfortunately, the sample density is inadequate to clearly establish its existence or location: the dip here is registered by only one point, which could be a fluctuation.

At this point I present the two spectral profiles that can be derived from the data. The first is the convolution of the emission spectrum with the spectrometer lineshape. This profile is used to for comparison with the theory. Reference to eqn. (A2.33) indicates how this profile is obtained, one integrates the measured two-dimensional profile over collection system wavelength:

$$\begin{aligned}\int_0^\infty d\lambda_c \cdot W_{\text{collected, beam}}(\lambda_s,\lambda_c) &= \int_0^\infty d\lambda_c \cdot \left(\int_0^\infty d\lambda \cdot S_{n,\lambda}(\lambda) \cdot C_n(\lambda-\lambda_c) \cdot \Sigma(\lambda_s-\lambda) \right) \\ &= \int_0^\infty d\lambda \cdot S_{n,\lambda}(\lambda) \cdot \Sigma(\lambda_s-\lambda) \left(\int_0^\infty d\lambda_c \cdot C_n(\lambda-\lambda_c) \right) \\ &= (\text{const}) \cdot \int_0^\infty d\lambda \cdot S_{n,\lambda}(\lambda) \cdot \Sigma(\lambda-\lambda_s)\end{aligned} \qquad (6.5)$$

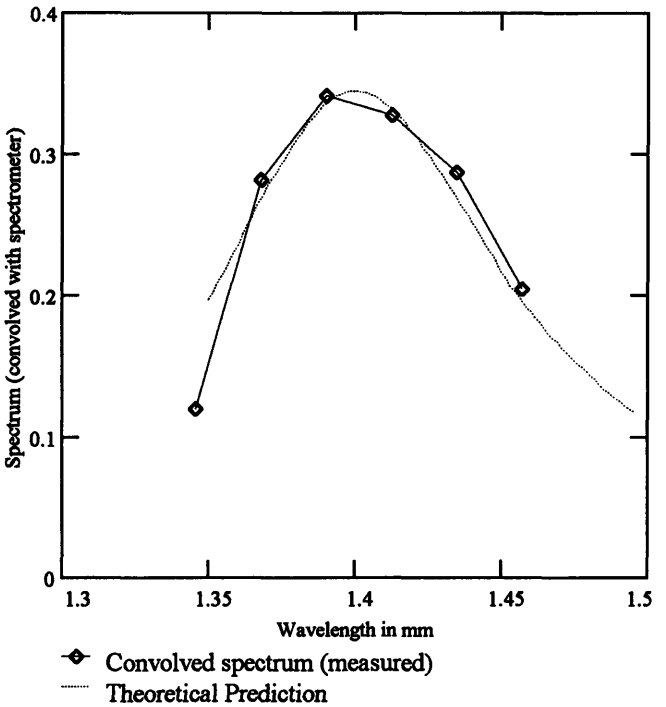

FIGURE 6-5. The measured profile of the emission spectum/spectrometer-lineshape convolution, compared to the van den Berg theory convolved with the spectrometer lineshape function. The agreement in the measured vs. theoretical peak wavelengths is not as good as shown here; I have shifted the data 20 μm to the red so as to permit a comparison of the shapes of the measured and theoretical peaks.

That is, each point of the convolution profile is obtained by summing the data taken at a given spectrometer setting from the various scans taken at different collection system positions. Figure 6-5 is a plot of these sums, compared to the profile comprised of the spectrum convolved with the spectrometer lineshape function. The measurements clearly show a peak structure; it is not subtle. The position of the experimental and theoretical peaks are in good agreement. The measured wavelength at the maximum is $\lambda_{\text{peak, measured}} = 1.424 \pm 0.009$ mm (equivalent to an emission angle $\vartheta_{\text{peak, measured}} = 114.3 \pm 0.6°$); the FWHM of the measured peak structure is 0.114 ± 0.005 mm. The peak of the profile obtained by convolving the spectrometer lineshape with the van den Berg theoretical spectrum is located at $\lambda_{\text{theory, peak}} = 1.400$ mm (corresponding to an emission angle of $\vartheta_{\text{peak, theory}} = 112.8°$), with a FWHM of 0.124 mm. The agreement between theory and experiment is good. The discrepancy in the peak wavelength between theory and experiment can be attributed to ambiguity in determining the "zero-offset" angle of the spectrometer (i.e., the orientation at which specular reflection is passed by the spectrometer). The error bars on the measurement are probably unduly optimistic. The discrepancy between the theoretical and

measured FWHM values is attributable in part to the fact that the data points at each end of the profile are systematically depressed with respect to the remainder of the profile. Remember that the data of this profile are composed of sums over collection system wavelength settings: the integrals comprising the end points were each missing a datum, and it was not possible to reasonably extrapolate. Thus, I estimate each of the end points to be roughly 10-15% below its "real" value. The effect will be to make the measured curve appear narrower. Moreover, there is uncertainty (which is very hard to assess without more and better lineshape data) in the spectrometer lineshape function that is not taken into account in this analysis, which could affect the FWHM comparison.

I also derived another profile from the 2-dimensional data array, that of the convolution of the emission spectrum with the collection system response curve. This convolution profile is obtained from an integration over spectrometer wavelength settings:

$$\begin{aligned}\int_0^\infty d\lambda_s \cdot W_{\text{collected, beam}}(\lambda_s,\lambda_c) &= \int_0^\infty d\lambda_s \cdot \left(\int_0^\infty d\lambda \cdot S_{n,\lambda}(\lambda) \cdot C_n(\lambda-\lambda_c) \cdot \Sigma(\lambda_s-\lambda) \right) \\ &= \int_0^\infty d\lambda \cdot C_n(\lambda-\lambda_c) \cdot S_{n,\lambda}(\lambda) \left(\int_0^\infty d\lambda_s \Sigma(\lambda_s-\lambda) \right) \\ &= (\text{const}) \cdot \int_0^\infty d\lambda \cdot S_{n,\lambda}(\lambda) \cdot C_n(\lambda-\lambda_c)\end{aligned} \qquad (6.6)$$

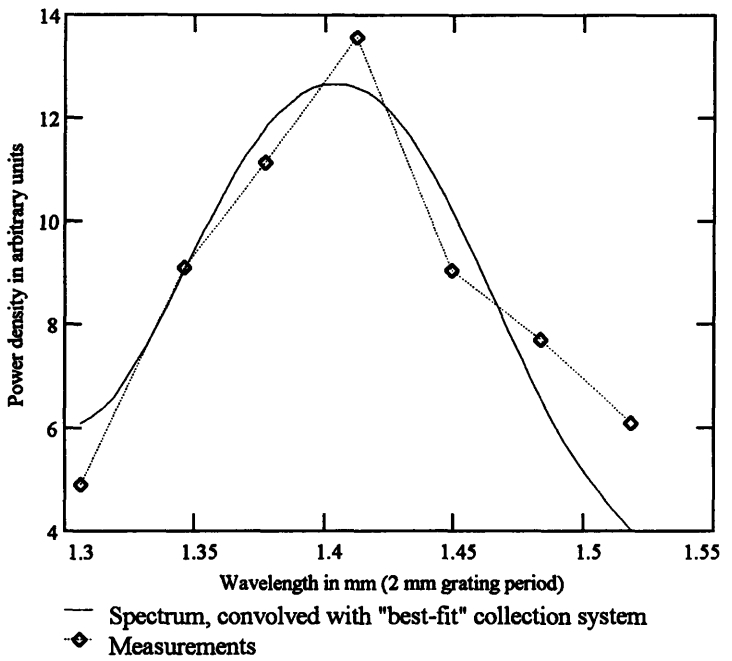

FIGURE 6-6. The convolution of the collection system response with the emission spectrum. The theory curve (solid line) is the convolution with an adjusted-width collection system curve, the width being adjusted to yield the best least-squares fit to the data.

That is, each point of this convolution profile is obtained by summing the data taken at each collection system setting. Figure 6-6 displays a plot of the result. Since the spectrum-spectrometer lineshape function convolution measurements agree well with the theory, I use the spectrum-collection system response convolution measurements to estimate the width of the collection system response. The theoretical curve shown is a narrowed collection system response profile, the width of which was adjusted by a least squares fit of the convolution to the measured profile. The best fit was obtained by a collection system profile with a width of 0.8 ± 0.1 times that of the original calculated collection system curve. Thus, I estimate that the actual collection system response is ~20% narrower than the curves calculated in Sec. 5.2.3. This fact must be taken into acount in planning future experiments with this apparatus.

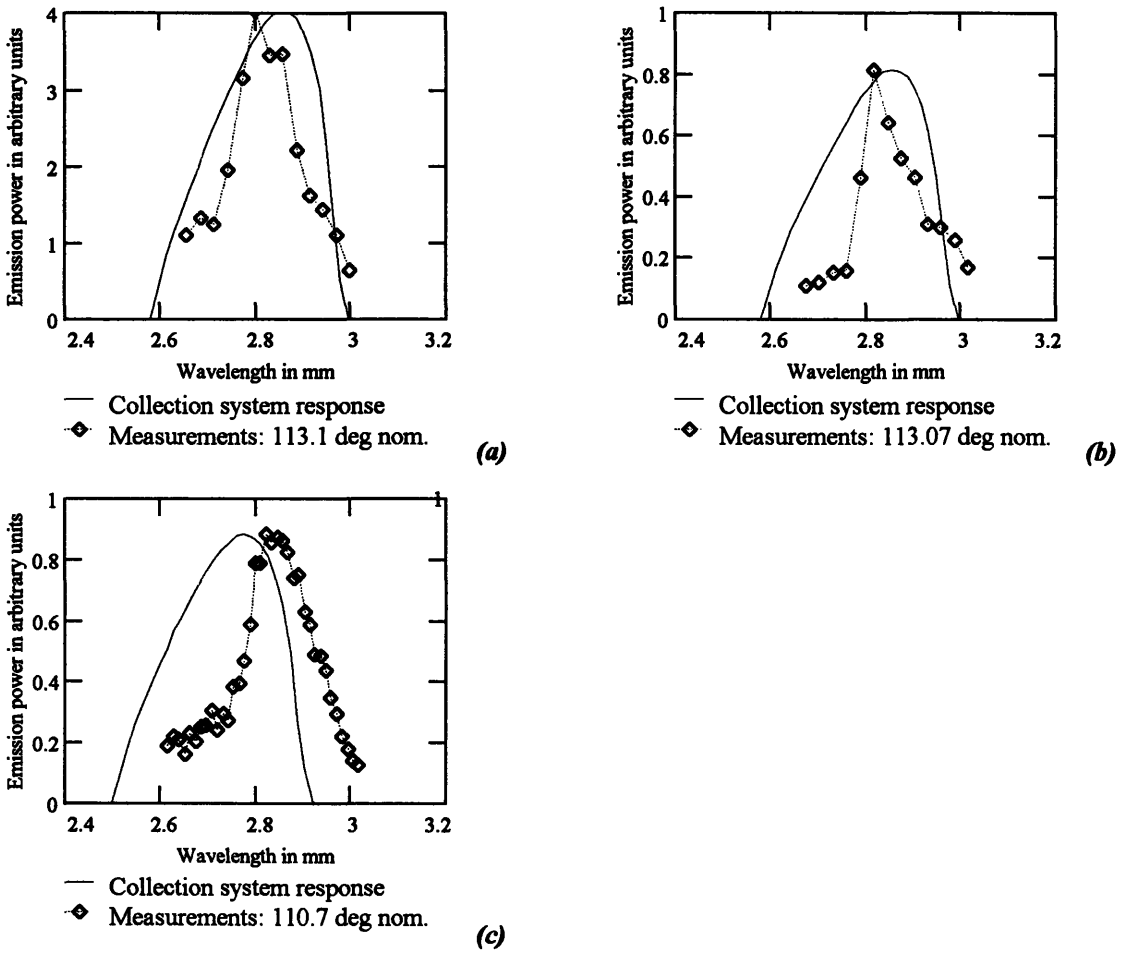

FIGURE 6-7. The spectrometer scans used for the spectral peak measurements. The nominal collection system setting for scan (c) is lower in wavelength than the other two scans; I suspect that the actual collection system position was not as far to the red as the nominal position would imply.

6.3.3 Measurements of a spectral peak: the 4 mm period grating

Having established the existence of a peak via the matrix measurement and analysis discussed in the previous section, we could study the analogous peak structure in the second-order emission spectrum of a 30° blaze grating of period 4 mm by means of well-placed (i.e., with appropriate collection system settings) spectrometer scans. Three such scans were taken. These measurements do not provide very accurate assessments of the peak's width, since the collection system response curve will distort the peak's shape. Nevertheless, the wavelength of the peak is reasonably well-determined. Figure 6-7

presents the spectrometer scan data. I report the measured peak wavelength as the mean value of the results from the three scans, and report the standard error as the uncertainty, resulting in $\lambda_{peak,\,measured} = 2.830 \pm 0.007$ mm. The van den Berg theory predicts the peak wavelength to be $\lambda_{peak,\,theory} = 2.800$ mm (twice that of the 2 mm period grating peak wavelength). This agreement is good, but just as the results of the previous section and the next section, the measured wavelength exceeds the theoretical; I suspect a systematic error in determination of the spectrometer offset angle (i.e., the angle registered on the vernier scale at specular reflection from the spectrometer grating). In the next section, I will compute the wavelength difference between the peak and the dip features from the 4 mm period grating, and it will be seen that the measured and theoretical wavelength differences agree within the bounds of uncertainty.

I must emphasize that the above results derive much of their value from the measurements and analysis of Sec. 6.3.2 above. They do not by themselves *prove* the existence of the peak, since the peak structures they show could be argued to be due solely to the shape of the collection system response curve, in the absence of additional evidence for the peak's existence. Indeed, the peak structures are discernably narrower than theory would predict, because the measured emission peak is somewhat narrowed by the collection system response. However, the structure of the red side of the scan in each case shows a flat emission profile, followed by a sharp rise- a characteristic signature of a peak. Also, the empirical knowledge of the collection system width (i.e., that the collection system acceptance is about 80% the calculated width) obtained from the results of Sec. 6.3.2 gives me confidence that the collection system response encompasses the peak structure in each of the scans. In each scan, there is only a barely discernable signature of the dip feature, thus the collection system was positioned at least half a FWHM of 240 μm or more to the red of the dip. The dip is located at 2.67±0.01 mm (see Sec. 6.3.4 below), and so the red side of the collection system's FWHM thus extends to

about 2.91 mm, well beyond the peaks seen in the scans. Thus, one cannot dismiss the scan as showing a "shelf" structure rather than a peak, with the peak and the rolloff on the red side created entirely by the collection system response.

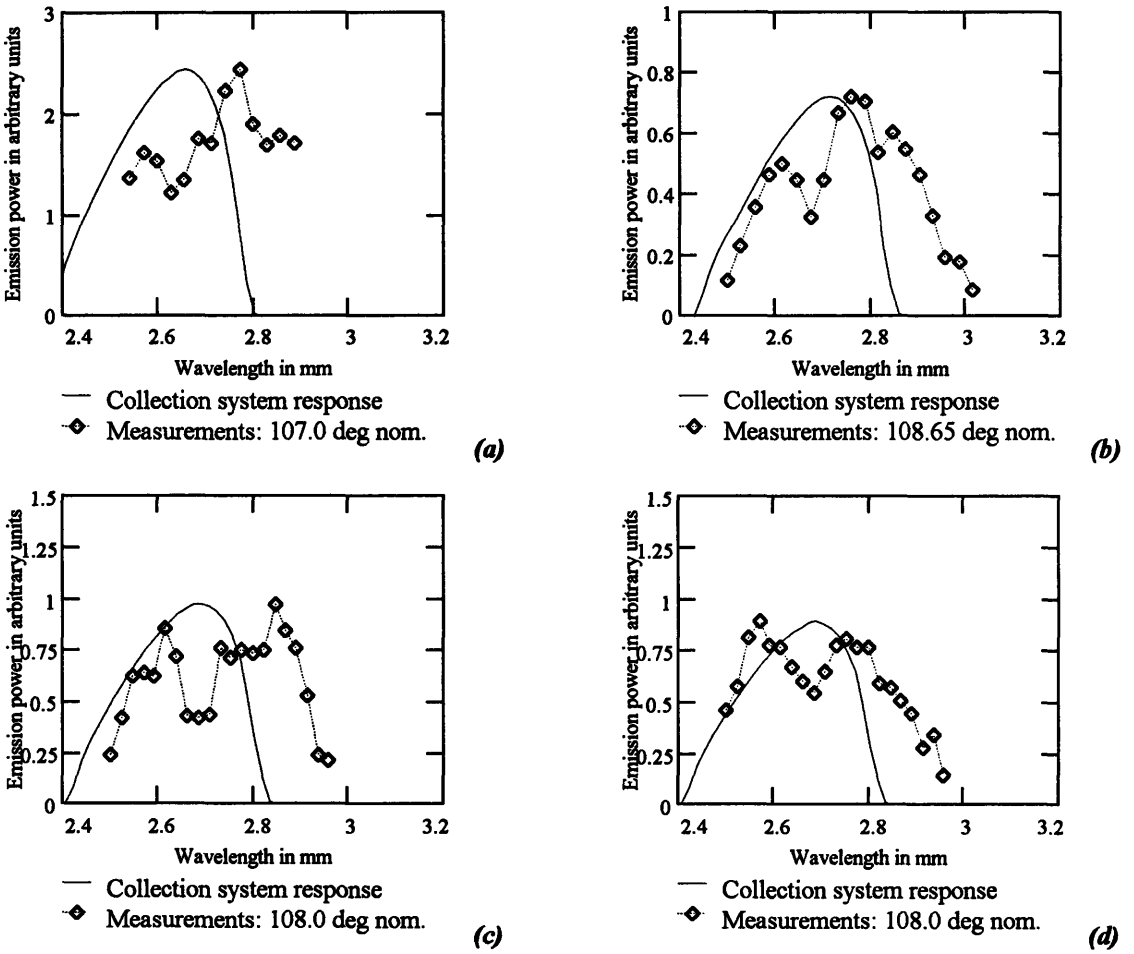

FIGURE 6-8. The spectrometer scan data for the dip measurements.

6.3.4 Measurements of a spectral dip: the 4 mm period grating

We were fortunate to observe and measure a spectral dip in the emission from a 30° blaze grating of period 4 mm, in the second order. I say "fortunate" because at the time the measurements were made, we were unaware of its possible existence; the theoretical calculations at that point were in a developmental state. The measurements do not permit any characterization of the dip beyond a determination of its location, since we

did not acquire a spectrometer/collection system matrix of data in the vicinity of the dip, as we did in the case of the peak. A total of four spectrometer scans were taken with the collection system placed so as to show a very clear dip. Figure 6-8 shows the scans. I report the measured position of the dip as the mean of the measured values, and report the standard error as the uncertainty, resulting in $\lambda_{\text{dip, measured}} = 2.667 \pm 0.012\,\text{mm}$. The van den Berg calculations place the dip of the "bare" (i.e., unconvolved) spectrum at $\lambda_{\text{dip, "bare" theory}} = 2.680$ mm, and the dip of the spectrum convolved with the spectrometer lineshape function at $\lambda_{\text{dip, convolved theory}} = 2.645\,\text{mm}$. The latter value agrees very well with the measurement.

In contrast to the peak measurements of Sec. 6.3.3, the dip measurement is independently reliable. No collection system artifact would produce a dip that appeared at a fixed *wavelength*, but would rather produce an artifact at some fixed angular displacement from the nominal accepted emission angle. The collection system is at three different settings in the four spectrometer scans, yet the dip appears at very nearly the same wavelength. One therefore cannot dismiss the dip as a collection system artifact.

I remarked in Sec. 6.3.3 that I suspect a systematic error in the wavelength measurements, resulting in both the peak and dip measurements being to the red of the theory. The difference between these measurements will not suffer from such an error, however. That difference is 163±14 μm, compared to the theoretical value of 155 μm (in the profile given by the spectrometer lineshape convolved with the theoretical spectrum).

Table 6-1. Summary of quantitative results and comparison to theory. Units are mm.

FEATURE	$\lambda_{measured}$	λ_{theory}	$FWHM_{meas}$	$FWHM_{theory}$
Peak, 2mm period grating	1.42(1)	1.400	.114(5)	.124
Peak, 4 mm period grating	2.83(1)	2.800	-	-
Dip, 4 mm period grating	2.67(1)	2.645	-	-
$\lambda_{peak} - \lambda_{dip}$	.163(14)	.155	-	-

6.4 Suggested future work and conclusions

Table 6-1 summarizes the quantitative results of this chapter. The most precisely controlled study to date of the Smith-Purcell effect strongly supports the theory of van den Berg.

The many difficulties overcome in the process of performing the measurements of this chapter- sorting out the two spectral transfer functions to successfully produce a conclusive spectral measurement and empirically characterize the collection system response curve FWHM, identifying and characterizing diffraction effects as the cause for the seemingly anomalous spectrometer lineshape function, as well as the long job of bringing the experiment to life- have paved the way for some very interesting future work with this apparatus at the ATF. There remain many spectral measurements of value to be made of the inverse Wood anomaly peaks. A variety of lineshape studies of peaks at various emission angles from gratings of various blaze angles could be performed. For example, the exhibition of narrowing of a particular peak with reduced grating blaze angle would be both easy (knowing what is now known) and instructive. Studies to identify grating geometries to exploit the inverse Wood anomaly for use for FIR sources would be useful.

Much was sought for and not found, but remains worth finding. Emission from electrons compressed into a bunch much shorter than some emission wavelength should emit coherently at that wavelength. I searched vigorously for such coherent emission, but was hampered by using long electron bunches and never saw the effect. I hypothesize that the coherent enhancement of emission power of wavenumber k_o in Smith-Purcell emission, from a pulse of N electrons distributed in a Gaussian longitudinal density distribution having standard deviation σ_z, scales as $N^2 \exp\left(-k_o^2 \sigma_z^2 / \beta^2\right)$ (the argument follows that of [Nodvick and Saxon, 1954]). An interesting signature of such an effect would be anomalously strong emission for wavelengths larger than a threshold wavelength of order $\lambda_{\text{threshold}} \equiv 2\pi\sigma_z/\beta$. Another signature would be anomalously strong emission in the first order, as compared to higher emission orders, at a given emission angle. In any case, short-bunch-length coherence is of great potential importance since one obtains high emission power without the overhead of a resonator cavity as in a FEL. Demonstration of this effect may be possible at the ATF, since the threshold wavelength is $\lambda_{\text{threshold}} = 17.6$ mm for an electron pulse of duration FWHM 11 psec* , and a wavelength three or four times shorter would perhaps produce a discernable effect. In fact, were such pulses available during the photoemission run of August 1993, we should have seen the effect. No effect was observed then, though I suspect that the pulse length was greater at that time.

Another important effect could be produced with the 50 MeV beam at the ATF. Just as in wiggler emission, Smith-Purcell emission from highly relativistic electrons is expected to be sharply peaked in the forward direction [Walsh *et. al.*, 1994]. He will require no urging from my quarter to pursue this very interesting potential FIR source.

* This electron pulse length was recently obtained at the ATF [X.J. Wang, private communication 1994].

CHAPTER 7

CONCLUSIONS

7.1 The theses

To summarize my work, I will explicitly state its theses and list their support.

• Short-period wigglers with very high field precision, costing more than an order of magnitude less than permanent-magnet, hybrid, or superconducting wigglers of comparable performance, can be built.

- The MIT Microwiggler for free electron lasers

• I have constructed a novel 8.8 mm period Microwiggler which generates the world's most uniform magnetic field having a period of less than 10 mm.

- Novel tuning scheme
- Complete battery of wiggler field measurements

• Wiggler-induced incoherent emission can be exploited as a measure of an electron beam's transverse phase space.

- Incoherent wiggler emission spectrum measurements and modelling of spectral broadening effects

• My grating emission measurements are the most precisely controlled experiments performed to date of the Smith-Purcell effect.

- Use of relativistic electrons from a high-brightness accelerator, with mm-period gratings (after [Doucas *et. al.*, 1992])
- Careful microwave spectroscopy (characterizing the two spectral transfer functions in the system)

- An inverse Wood anomaly peak predicted by Hessel exists.

- Cursory examination of the spectrometer/collection system data matrix

- The van den Berg theory correctly describes detailed features of spectral peak structures.

- Careful analysis of the spectrometer/collection system data matrix
- Peak wavelength and FWHM, 2 mm period 30° blaze grating
- Peak wavelength, 4 mm period 30° blaze grating
- Dip wavelength, 4 mm period 30° blaze grating

7.2 The implications

The Microwiggler project from its outset has been a technology development effort, with the goal of operating and studying a free electron laser based on a short-period wiggler. The successful design, construction, and operation of the Microwiggler comprises great progress towards that goal. Moreover, the design of the Microwiggler is generally applicable to single-user FEL radiation sources, and to FELs constructed for study of FEL physics. The tunability of the Microwiggler makes it particularly suited to the latter application- a variety of field tapers can be installed, perhaps including optical klystron or harmonic generation field configurations.

The spectral measurements of incoherent emission from the Microwiggler are in themselves perhaps of less general importance, but they comprised a crucial programmatic milestone for both the FEL project at the ATF, and the ATF itself. They are also a good starting point for developing incoherent emission as a diagnostic of the electron beam's transverse phase space. Such a diagnostic may be very useful to make the FEL lase.

My measurements of the Smith-Purcell effect have both scientific and technological implications. They precisely test for the first time a comprehensive theory of the effect of Smith and Purcell, forty years after their original work. Thus, the measurements are new physics of general interest, addressing a problem of long standing. The measurements demonstrate a new phenomenon, the inverse Wood anomaly resonance, which is interesting physics as well as potentially useful for FIR source technology. This peaking effect may find potential application in a Smith-Purcell free electron laser or as a bright source of incoherent FIR to compete with synchrotron FIR sources.

APPENDIX 1

SUMMARY OF THE VAN DEN BERG THEORY

A1.1 Introduction

This appendix summarizes results from a the theory of the Smith-Purcell effect, as presented by van den Berg [van den Berg, 1973]. The theory is a rigorous application of the concept originally advanced by Toraldo de Francia [Toraldo de Francia, 1960] of the Smith-Purcell effect as grating diffraction of the evanescent waves produced by the electron's uniform motion. Section A1.2 presents the form of these waves. In Section A1.3, I show that the Smith-Purcell wavelength relation (1.4) is an immediate consequence of expressing the emitted waves as a Floquet series, and present the integral equations which determine the coefficients of those series. Finally, I present van den Berg's result relating the solutions of that equation to power lost by the electron to the radiation field, thus enabling comparison of my experimental results to the theory.

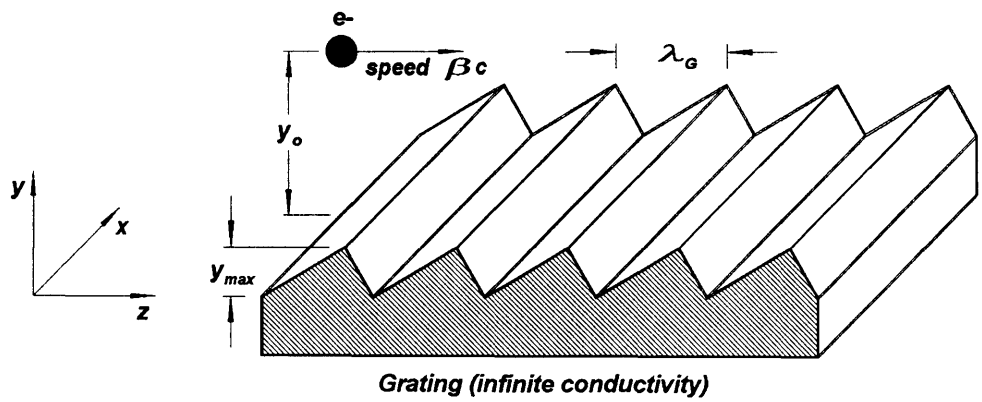

FIGURE A1-1. The coordinate system used in the presentation of the van den Berg Smith-Purcell theory. The grating is assumed infinite in x, and infinite and periodic in z. The origin (z=0) is taken to be at grating bottom; the electron height above grating bottom is y_o, and the grating groove depth is y_{max}. Also note that the (x, y, z) field components are labelled (1, 2, 3), respectively.

A1.2 The fields of an electron in uniform motion: decomposition into evanescent waves

A moving electron has electric and magnetic field components which vary in both time and space. The fields can be described in terms of a Fourier transform. One can state *a priori* certain properties of the waves composing the Fourier transform representation of the field. First, there is net energy transport by the waves only along the electron's direction of motion. If energy were transported in other directions by the waves, the electron would be radiating; a charge in uniform motion cannot emit radiation. Second, all of the waves must travel with the same phase velocity, which must be equal to the electron's speed of propagation. This is required by the fact that the fields are static fields in the electron's rest frame. Third, the waves do not extend over all space, but must decrease with distance from the electron. It will be seen that this decrease is exponential.

I will now describe van den Berg's results. Figure A1-1 shows the coordinate system for describing the fields. **Note that the (*x, y, z*) field components are labelled (1, 2, 3),** respectively in the discussion that ensues. The Fourier transform is carried out in the time and the spatial *x*-coordinate; the electron travels parallel to the *z*-axis; the grating lies in the *x*-*z* plane; and the rulings of the grating are parallel to the *x*-axis. The Fourier transforms of the electric and magnetic fields are*

$$\begin{aligned}\vec{E}^i(x,y,z,t) &= (2\pi)^{-2}\int_0^\infty d\omega \int_{-\infty}^{\infty} db\cdot \vec{\varepsilon}^i(y,z;b,\omega)\cdot\exp(ibx-i\omega t)\\ \vec{H}^i(x,y,z,t) &= (2\pi)^{-2}\int_0^\infty d\omega \int_{-\infty}^{\infty} db\cdot \vec{\eta}^i(y,z;b,\omega)\cdot\exp(ibx-i\omega t)\end{aligned} \qquad \text{(A1.1)}$$

* This notation is at variance with that of [van den Berg, 1973]. This was unavoidable in that he chose a coordinate system orientation different from that of most authors. Moreover, he chose to use MKS units, whereas the units used in this thesis are CGS.

where the superscript *i* indicates that the fields are *i*ncident on the grating. Positive frequencies only need be considered because the fields are real-valued. The current density associated with the electron has form

$$\vec{\mathrm{J}}(x,y,z,t) = -e\beta c \cdot \delta(x, y - y_o, z - \beta ct) \cdot \hat{e}_3 \tag{A1.2}$$

which is just a three-dimensional Dirac delta-function describing a current density due to a charge moving parallel to the z-axis at height y_O above the grating at speed βc. The Fourier transform of the current density can be shown to be

$$\begin{aligned} \vec{J}(y,z;b,\omega) &= \hat{e}_3 (2\pi)^{-2} \int_{-\infty}^{\infty} dt \int_{-\infty}^{\infty} dx \cdot \vec{\mathrm{J}}(x,y,z,t) \cdot \exp(-ibx + i\omega t) \\ &= \hat{e}_3 \cdot (-e \cdot \exp(ia_0 z)\delta(y - y_o)) \end{aligned} \tag{A1.3}$$

in which $a_0 = \omega/\beta c$. We further define the magnitude of the free-space wave vector as $k_o = \omega/c$.

It can be shown that finding two of these six field components allows determination of the remaining four (via the Maxwell divergence equations). The same is true for the problem of computing the fields produced by the diffraction from the grating of the electron's evanascent waves. The x-components, ε^i_1, η^i_1, of the Fourier-transformed electric and magnetic fields, respectively, are chosen for solution.

The Fourier transforms $\vec{\varepsilon}^i, \vec{\eta}^i$ must satisfy the Maxwell equations. The equations determining the fields' x-components are just driven wave equations in which the driving term is the Fourier-transformed current density. They can be shown to be

$$\begin{aligned} \left\{ \frac{\partial^2}{\partial z^2} + \frac{\partial^2}{\partial y^2} + k_o^{\,2} - b^2 \right\} \eta^i_1 &= \frac{-4\pi}{c} \frac{\partial}{\partial y} J_3 \\ \left\{ \frac{\partial^2}{\partial z^2} + \frac{\partial^2}{\partial y^2} + k_o^{\,2} - b^2 \right\} \varepsilon^i_1 &= \frac{4\pi b}{k_o c} \frac{\partial}{\partial z} J_3 \end{aligned} \tag{A1.4}$$

where J_3 is the z-component of the Fourier transform of the current density due to the moving electron. The solutions to these equations (the desired Fourier transforms of the electron-produced fields) are found to be

$$\begin{aligned} \eta^i_1(y,z;b,\omega) &= \frac{4\pi e}{2c}\exp(ia_0 z)\exp(ig_0|y-y_o|)\cdot \mathrm{sign}(y-y_o) \\ \varepsilon^i_1(y,z;b,\omega) &= -\frac{4\pi e b}{2g_0\beta c}\exp(ia_0 z)\exp(ig_0|y-y_o|) \end{aligned} \quad , \qquad \text{(A1.5)}$$

where we define

$$g_0 \equiv i\sqrt{a_0^{\,2}+b^2-k_o^{\,2}}; \qquad \begin{aligned} \mathrm{sign}(y) &\equiv +1,\ y>0 \\ &\equiv -1, y\le 0 \end{aligned} \qquad \text{(A1.6)}$$

As earlier remarked, the Fourier transforms (A.5) describe plane waves propagating in the same direction as the electron. Likewise, the components at all frequencies have the same phase velocity, equal to that of the electron's propagation speed, as was stated at the outset. Also, since g_0 is imaginary, we see that the fields indeed are attenuated exponentially in distance away from the electron, with a 1/e attenuation length of

$$\frac{1}{g_0} = \frac{1}{\sqrt{a_0^{\,2}+b^2-k_0^{\,2}}} = \frac{1}{\sqrt{k_0^{\,2}\left(\frac{1}{\beta^2}-1\right)+b^2}}. \qquad \text{(A1.7)}$$

This implies that the emission field, which is proportional to the strength of the source fields, also will fall off exponentially with the electron's height above the grating, as earlier asserted. As will be shown shortly, the (b = 0) case is of particular relevance to our data: in terms of the electron parameters β, γ, we have

$$\left.\frac{1}{g_0}\right]_{b=0} = \frac{1}{\sqrt{k_0^2\left(\frac{1}{\beta^2}-1\right)}} = \frac{\beta\gamma}{k_o} \qquad \text{(A1.8)}$$

Thus, the attenuation length increases with electron energy, and is linearly proportional to the radiation wavelength. The increase in attenuation length with energy has a simple physical basis. The transverse electric and magnetic fields of a relativistic charged particle are increased by a factor of γ with respect to the parallel field components, resulting in the familiar "whisk-broom" effect [Jackson, p. 555].

A1.3 Summary of the van den Berg theory

In this section I summarize the theory of the Smith-Purcell effect given by van den Berg [van den Berg, 1973]. He states the problem in terms of a scattering process. The waves described in Sec. A1.2 scatter from the infinitely conductive surface of a grating periodic in the z direction (see Fig. A1-1). The total fields, i.e., the sum of incident and reflected waves, must satisfy boundary conditions on the grating surface. The grating surface is periodic, so that the reflected field can be expressed as a Floquet expansion. As with any scattering process, the reflected wave amplitude is directly proportional to that of the incident wave.

Van den berg solves this boundary-value problem by expressing it in the form of an integral equation. His approach is precisely analogous, for example, to the standard approach for solving the potential scattering problem in non-relativistic quantum mechanics [Baym, p. 203]. He obtains his integral equation by use of a Green's function (analogous to the propagator of the quantum scattering problem). The solution of the integral equation can then be used to obtain the coefficients of the Floquet expansion for

the reflected fields (analogous to finding the amplitudes of the partial waves in the quantum scattering problem).

Van den Berg also computes the rate of energy loss by the electron to radiation, by computing the work done on the electron by the reflected fields as the electron traverses one grating period. This result is crucial to relating the results of the Smith-Purcell theory to experiment.

I will now present some formal results. Just as in the case of the problem of finding the electron's evanescent waves, the problem is expressed in terms of the Fourier transforms of the reflected field components. These Fourier transforms must satisfy the transformed Maxwell curl equations in free space,

$$\begin{aligned}\left(\nabla + ib\hat{e}_1\right)\times\vec{\eta}^r(y,z;b,\omega) &= \frac{-i\omega}{c}\vec{\varepsilon}^r(y,z;b,\omega)\\ \left(\nabla + ib\hat{e}_1\right)\times\vec{\varepsilon}^r(y,z;b,\omega) &= \frac{+i\omega}{c}\vec{\eta}^r(y,z;b,\omega)\end{aligned}. \qquad \text{(A1.9)}$$

The boundary condition on the grating surface is expressed in terms of the total fields, composed of the sum of the incident fields $\vec{\varepsilon}^i, \vec{\eta}^i$ (given in Sec. A1.2) and reflected fields $\vec{\varepsilon}^r, \vec{\eta}^r$. The grating occupies the entire *x*-*z* plane, with rulings parallel to the x-axis. Again, just as in the determination of the fields from a moving electron, the problem can be solved completely by finding two of the six field components. The field *x* components are selected. The grating is periodic in z. The grating surface is assumed to be of infinite conductivity, thus the boundary conditions on the field *x*-components $\varepsilon^r{}_1$, $\eta^r{}_1$ are

$$\begin{aligned}\left.\varepsilon^i{}_1 + \varepsilon^r{}_1\right]_{\text{Grating surface}} &= 0\\ \left.\hat{n}\cdot\nabla\left(\eta^i{}_1 + \eta^r{}_1\right)\right]_{\text{Grating surface}} &= 0\end{aligned}. \qquad \text{(A1.10)}$$

Here $\hat{n}$ is the unit vector field normal to the grating surface. These are the usual boundary conditions for field components parallel to an infinitely conductive surface.

To emphasize the fact that the remaining four electromagnetic field components are derivable from the fields' x-components, **van den Berg defines the generating functions $\Phi \equiv \varepsilon_1$, $\Psi \equiv \eta_1$.* These definitions will be used henceforth to refer to x-components of both the incident and reflected fields**. It was already mentioned that the grating is infinite in extent in the x and z directions, and periodic in z. The periodicity in z implies that the reflected fields can be written in terms of a Floquet expansion:

$$\begin{aligned} \Phi^r(y,z;b,\omega) &= \sum_{n=-\infty}^{\infty} \Phi^r{}_n(b,\omega)\exp(ia_n z + ig_n y) \\ \Psi^r(y,z;b,\omega) &= \sum_{n=-\infty}^{\infty} \Psi^r{}_n(b,\omega)\exp(ia_n z + ig_n y) \end{aligned} \tag{A1.11}$$

where the a_n, g_n are defined by

$$a_n \equiv a_0 + \frac{2\pi n}{\lambda_G}, \quad g_n \equiv \sqrt{k_o^{\,2} - b^2 - a_n^{\,2}} \quad (a_0 \equiv \frac{k_o}{\beta}\ ). \tag{A1.12}$$

λ_G denotes the grating period; also, note that the terms g_n will be either real or imaginary, and we choose the root on the positive real or positive imaginary axis. Also, remember that the electron velocity is βc.

At this point, we should write out time domain field components in terms of the Fourier integrals, to allow physical interpretation of the a_n, b, and g_n terms: the fields are

* Some might find this an unnecessary and confusing notational embellishment (as I did). To preserve as much similarity as possible between this short summary and van den Berg's presentation, I nevertheless follow his convention.

$$H^r{}_1(x,y,z,t) = \int_0^\infty d\omega \int_{-\infty}^\infty db \left(\sum_{n=-\infty}^\infty \Psi^r{}_n(b,\omega) \exp(ia_n z + ig_n y) \right) \exp(ibx - i\omega t)$$
$$E^r{}_1(x,y,z,t) = \int_0^\infty d\omega \int_{-\infty}^\infty db \left(\sum_{n=-\infty}^\infty \Phi^r{}_n(b,\omega) \exp(ia_n z + ig_n y) \right) \exp(ibx - i\omega t) \quad . \text{(A1.13)}$$

Defining $\vec{k}_n^{\,r} \equiv b\hat{e}_1 + g_n\hat{e}_2 + a_n\hat{e}_3$, the field can be expressed as

$$H^r{}_1(x,y,z,t) = \int_0^\infty d\omega \int_{-\infty}^\infty db \sum_{n=-\infty}^\infty \Psi^r{}_n(b,\omega) \exp(i\vec{k}_n^{\,r} \cdot \vec{r} - i\omega t). \qquad \text{(A1.14)}$$

The quantities $\vec{k}^r{}_n$ are thus the wave-vectors of the reflected modes. It is trivial to show that these waves satisfy the dispersion relation for free-space propagation, $|\vec{k}^r{}_n| = \omega/c$. Only modes with real-valued g_n radiate (*i.e.*, transport energy away from the grating to infinity).

The index n of a given mode in the sum of reflected modes is referred to as its *order*. As earlier mentioned, only certain orders radiate, those such that g_n is real: thus, examining definitions (A1.12), it can be immediately shown that a necessary condition for an order n to be radiative is that $n < 0$. The relation of wavelength to emission angle can be easily found for such orders: defining the angle θ_n as the angle between $\vec{k}^r{}_n$ and the z-axis, we have

$$k_o \cos\theta_n = a_n = \frac{k_o}{\beta} + \frac{2\pi n}{\lambda_G} \qquad \text{(A1.15)}$$

from which it immediately follows that

$$\lambda_n = \frac{2\pi}{k_o} = \frac{\lambda_G}{|n|}\left(\frac{1}{\beta} - \cos\theta_n\right), \qquad \text{(A1.16)}$$

which is the wavelength relation (1.4).

I will now present the integral equations that must be solved in order to find the amplitudes of the various emission orders. As I already stated, van den Berg employs a Green function* formalism to solve the boundary value problem posed in eqns. (A.9) and boundary conditions (A1.10). The appropriate Green function can be shown to be [van den Berg, 1971]

$$G(y,z,y',z';b,\omega)=\sum_{-\infty}^{\infty}\frac{i}{2g_n\lambda_G}\exp\left(ia_n(z-z')+ig_n|y-y'|\right), \qquad \text{(A1.17)}$$

in terms of which, for points above the grating, the integral expressions for the reflected field generating functions can be shown to be

$$\begin{aligned}\Psi^r(y,z;b,\omega)&=-\int_L ds'\ \Psi(y',z';b,\omega)\left(\hat{n}(y',z')\cdot\nabla' G(y,z,y',z';b,\omega)\right)\\ \Phi^r(y,z;b,\omega)&=\int_L ds'\ \left(\hat{n}(y',z')\cdot\nabla'\Phi(y',z';b,\omega)\right)G(y,z,y',z';b,\omega)\end{aligned} \qquad \text{(A1.18)}$$

where ds' denotes an infinitesimal displacement along a contour formed by the intersection of the grating surface and the y-z plane, contained in one grating period (the contour is denoted by L: see Fig. A1-2). By substitution of (A1.17) into (A1.18), it can be shown with the aid of (A1.11) that the Fourier components $\Psi^r{}_n(b,\omega)$ are given by

$$\begin{aligned}\Psi^r{}_n(b,\omega)&=-\left(i/2g_n\lambda_G\right)\int_L ds'\ \Psi(y',z';b,\omega)\left(\hat{n}\cdot\nabla'\exp\left(-ia_nz'-ig_ny'\right)\right)\\ \Phi^r{}_n(b,\omega)&=i/2g_n\lambda_G\int_L ds'\ \left(\hat{n}\cdot\nabla'\Phi(y',z';b,\omega)\right)\exp\left(-ia_nz'-ig_ny'\right)\end{aligned} \qquad \text{(A1.19)}$$

* In imitation of Jackson, I use the term "Green function" in lieu of "Green's function", the latter being both more standard and more awkward.

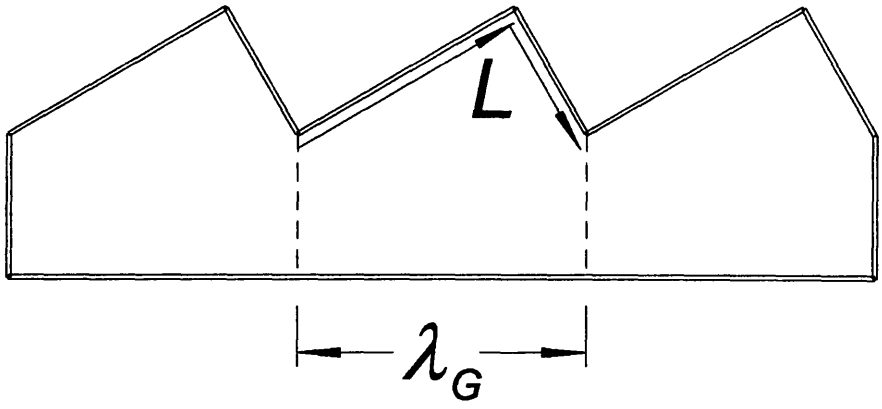

FIGURE A1-2. The integral contour L for the van den Berg integral equation.

The problem is thus reduced to finding the value of the generating functions Ψ, Φ on the grating surface L. An integral equation of the second kind can be obtained for this quantity, by letting the points of observation in (A1.18) approach L. The result is

$$\frac{1}{2}\Psi(y,z;b,\omega)+P\int_L ds'\,\Psi(y',z';b,\omega)\hat{n}(y',z')\cdot\nabla' G(y,z,y',z';b,\omega)$$
$$=\Psi^i(y,z;b,\omega)$$
$$\frac{1}{2}\hat{n}(y,z)\cdot\nabla\Phi(y,z;b,\omega)+P\int_L ds'\,\left(-\hat{n}(y,z)\cdot\nabla G(y,z,y',z';b,\omega)\right)\left(\hat{n}(y',z')\cdot\nabla'\Phi(y',z';b,\omega)\right)$$
$$=\hat{n}(y,z)\cdot\nabla\Phi^i(y,z;b,\omega) \qquad \text{(A1.20)}$$

where the P denotes a Cauchy principal value integral, *i.e.*, the integral excludes singular points from the gradient operator acting on the Green function at its singularities. Solutions to eqn. (A1.20) provided to me by Woods [Woods, private communication] are presented in Chapter 6.

Integral equations of this general form (integral equations of the second kind) arise in the description of many types of scattering processes, e.g., potential scattering in non-

relativistic quantum mechanics as mentioned earlier. One method of solution of the potential scattering problem is familiar to all: the Born approximation [Baym p. 203]. An analog of the Born approximation could be applied to solving (A1.20), by replacing the function Ψ^* in the integral with the function Ψ^i. That equation can be solved analytically for sufficiently simple grating geometries, e.g., blazed triangular gratings like those used in this work (see Sec. 5.2.4). One could proceed further along this line by means of Picard iteration [Braun p.70]: the solution obtained from the $\Psi \rightarrow \Psi^i$ integral substitution could then itself be substituted into the integral. This procedure could in principle be repeated ad infinitum.

Another approach is better-suited to our grating geometries, however, and was applied by Woods [Woods, private communication] to gratings of our geometry; the method was originally applied by van den Berg [van den Berg, 1973]. That method exploits the fact that the function Ψ on the grating surface is periodic, and so can be expressed in the form of a Fourier series. A matrix equation for the Fourier series coefficients can be found in analytic form for blazed triangular gratings. Truncation of the series then yields a matrix equation of finite dimension which can be solved numerically on a reasonably fast IBM-compatible personal computer (*i.e.*, a large mainframe machine, or even high-end workstation, is not required).

Once the values of the function Ψ on the grating surface have been determined, by whatever means, the strength coefficients Ψ^r_n for the various emission orders at the chosen frequency can be found by using (A1.19). This computation must then be repeated for each desired frequency. To compare the theory to the experiments, it is necessary to express measured quantities in terms of the computed coefficients (remember that the experiment measured a quantity proportional to the total radiation energy induced to emit

* These remarks are equally applicable to the electric field Φ, of course.

from the grating by a sequence of electron bunches). The comparison is accomplished by relating the mechanical work W done on the electron, by the reflected fields during the electron's traversal of one period, to the Poynting vectors of the emitted radiating waves. van den Berg's result is

$$W = \left(\lambda_G / 8\pi^3\right) \int_0^{\infty} d\omega \int_{-\infty}^{\infty} db \sum_{\text{real } g_n} \frac{\omega g_n}{k_o^{\,2} - b^2} \left(\Phi^r{}_n \Phi^r{}_n^{\,*} + \Psi^r{}_n \Psi^r{}_n^{\,*} \right). \qquad \text{(A1.21)}$$

This equation is the starting point for the analysis of Appendix 2.

APPENDIX 2

THE SMITH-PURCELL SPECTRAL MEASUREMENTS: RELATING THEORY AND EXPERIMENT

A2.1 Introduction

This appendix applies the general results of the previous Appendix to the specific case of the apparatus used in this work. In Sec. A2.2, I compute the fraction of a single electron's emission that is acquired by the collection system (see Sec. 5.2.3). This result is then generalized to the case of a beam of electrons in Sec. A2.3. Sec. A2.4 carefully describes how the beam profile measurements of Sec. 5.6.4 are used to compute (or at least estimate) parameters describing the electron beam phase space distribution. Finally, Sec. A2.5 incorporates the effects of the spectrometer into the results of the previous sections to yield the complete description of the measured emission power in terms of the general theory and the specific characteristics of the apparatus.

A2.2 Collecting emission from a single electron

This section quantifies the emission acquired by the collection system of Sec. 5.2.3, from a single electron propagating parallel to the grating at grazing incidence, along the z-axis (see Fig. A1-1).

The first step in the analysis is to exploit the fact that only emitted radiation with wave-vectors nearly parallel to the y-z plane will be accepted by the collection system (see Sec. 5.2.3). In quantitative terms, the experimental apparatus is restricted to collecting modes with (b / k_o) $\leq$ (lightpipe radius / OAPM focal length) ≈ 0.08. Thus $b \leq 0.08 k_o$.* This permits an immediate simplification to (A1.21), the (b^2) term in the integrands' denominators can be dropped to yield

* I assume the reader is familiar with the definitions of Appendix 1, and use them freely without citation.

$$W_{\text{collected, 1 period}} = \left(\lambda_G c/8\pi^3\right)\int_0^{\infty} d\omega \int_{-\infty}^{\infty} db \sum_{\text{real } g_n} \frac{g_n}{k_o}\left(\Phi^r{}_n \Phi^r{}_n^* + \Psi^r{}_n \Psi^r{}_n^*\right). \tag{A2.1}$$

Another simplification can be made. Equation (A1.20) shows that the reflected waves' amplitudes are directly proportional to those of the incident waves (this is a general property of scattering processes, as remarked earlier). This provides a basis for comparing the relative contributions of the $\Phi^r{}_n \Phi^r{}_n^*$ and $\Psi^r{}_n \Psi^r{}_n^*$ terms to the radiated energy W. The ratio of the square magnitudes of the field components Φ^i and Ψ^i is

$$\left|\frac{\Phi^i}{\Psi^i}\right|^2 = \left(\frac{b}{g_0 \beta}\right)^2 \tag{A2.2}$$

Using the definition of eqn. (A1.6), $g_0 \equiv i\sqrt{a_0{}^2 + b^2 - k_o{}^2}$, we can write

$$\left|\frac{\Phi^i}{\Psi^i}\right|^2 = \frac{b^2}{\frac{k_o{}^2}{\beta^2} + b^2 - k_o{}^2} = \frac{\left(\frac{b}{k_o}\beta\gamma\right)^2}{1 + \left(\frac{b}{k_o}\beta\gamma\right)^2} \tag{A2.3}$$

This relation implies that for small b, $\Psi^r{}_n \Psi^r{}_n^* >> \Phi^r{}_n \Phi^r{}_n^*$; the specific condition on b is

$$\left(\frac{b}{k_o}\right)^2 << \left(\frac{1}{\beta\gamma}\right)^2. \tag{A2.4}$$

This is a condition reasonably well-satisfied over the range of emission angles collected in this experiment. However, future experiments with this apparatus at higher energies may well need to account for the contribution of Φ to reconcile theory and experiment. We did

not require its inclusion to explain the results of this thesis, however, so that the $\Phi^r{}_n\Phi^r{}_n^*$ terms in the sum of eqn. (A2.1) are dropped: the result is

$$W_{\text{collected, 1 period}} \cong \left(\lambda_G c/8\pi^3\right)\int_0^\infty d\omega \int_{-\infty}^{\infty} db \sum_{\text{real } g_n} \frac{g_n}{k_o}\Psi^r{}_n\Psi^r{}_n^* \qquad \text{(A2.5)}$$

A final simplification can be made. The range of integration over b is restricted, because of the collection system acceptance limits. The restriction on b is ω-dependent, since the collection system limits the acceptance to $b \le 0.08k_o$ as earlier stated. I change variables in the integral to a variable $\varphi \equiv b/k_o$, and approximate the integral by use of $\int d\varphi \sum \rightarrow \delta\varphi \cdot \sum$ (i.e., I neglect the variation of the integrand over the range of integration): the result is

$$W_{\text{collected, 1 period}} \cong \left(\lambda_G c\delta\varphi/8\pi^3\right)\int_0^\infty d\omega \sum_{\text{real } g_n} g_n\Psi^r{}_n\Psi^r{}_n^*, \qquad \text{(A2.6)}$$

where $\delta\varphi \cong 2 \cdot 0.08$.

The next step in the analysis entails a change of variables in the integral of eqn. (A2.6) to emission angle coordinates; effects of the collection system can then be introduced. I use the fact that g_n is the y-component of the emitted wave-vector having magnitude k_o: since we are neglecting the x-component (of magnitude b), $g_n = k_o \sin\theta_n$ where θ_n is the emission angle associated with emission of order n (obtained from relation (A1.16)). Also, I employ the definition $k_o \equiv \omega/c$. Moreover, I will now sum over the entire interaction region, taken to be of length L_{int}. This introduces a factor equal to the number of periods ($= L_{\text{int}}/\lambda_G$). Substitution into (A2.6) yields

$$W_{\text{collected, total}} = \frac{L_{\text{int}}}{\lambda_G}\left(\lambda_G \delta\varphi / 8\pi^3\right)\int_0^{\infty} d\omega \cdot \omega \sum_{\text{real } g_n} \sin\theta_n \left(\Psi^r{}_n \Psi^r{}_n{}^*\right). \tag{A2.7}$$

Reversing the order of summation and integration (this is permitted because the sum has a finite number of terms), and then changing variables in each integral in the sum, yields

$$\mathrm{W}_{\text{collected, total}} \cong \left(L_{\text{int}} \delta\varphi / 8\pi^3\right) \sum_{\text{radiating orders } n} \int_0^{\pi} \left(-\frac{d\omega}{d\theta_n}\right) d\theta_n \cdot \omega \sin\theta_n \left(\Psi^r{}_n \Psi^r{}_n{}^*\right) \tag{A2.8}$$

Finally, I substitute for ω the wavelength relation (6.16) to cast the integrand into terms of θ_n (thus moving all quantities scaling with the grating period outside the integral):

$$W_{\text{collected, total}} \cong \frac{c^2 L_{\text{int}}}{2\pi {\lambda_G}^2} \delta\varphi \sum_{\text{radiating orders } n} \int_0^{\pi} d\theta_n \cdot \left(\frac{n^2 \sin\theta_n}{\left(\frac{1}{\beta} - \cos\theta_n\right)^3} \right) \sin\theta_n \left(\Psi^r{}_n \Psi^r{}_n{}^*\right) \tag{A2.9}$$

At this point, note that the total collected *energy* is $\propto 1/{\lambda_g}^2$. The instantaneous emitted *power* is emission-angle-dependent (see eqn. (5.4)); even so, the emission power at a given angle scales with the inverse square of the grating period. This is then the rigorous derivation of the scaling law of Sec. 1.2.4.

The *n*th term in the sum (A2.9) is the collected energy from spectral order *n*. Each integrand represents a distribution function in emission angle for the *n*th order emission emerging from the lightpipe. Before writing down the distribution functions, I remind the reader that the field Ψ on the grating surface is directly proportional to the incident field Ψ^i: this means that (via eqn. (A1.19)) the Fourier components of the reflected field $\Psi^r{}_n$ are proportional to Ψ^i as well. The y-dependence of Ψ^i on the grating surface is $\Psi^i \propto \exp(-|g_0| \cdot |y_o - y|) = \exp(-|g_0| \cdot (y_o - y))$; the equality follows because the electron

is above the grating surface (see Fig. A1-1). This means that the y_o-dependence can be factored from Ψ^i, and thus from the Floquet coefficients $\Psi^r{}_n$. This is convenient when considering the emission of a distribution of electrons in a beam. Van den Berg defines y_o-independent coefficients R_n as

$$\Psi^r{}_n \equiv R_n \cdot \exp\left(-g_0(y_o - y_{\max})\right) \tag{A2.10}$$

where y_{max} is the highest y-extent of the grating surface (Fig. A1-1). With this definition in hand, I define the emission spectral density distribution function $S_n(\theta_n)$ for the nth order emission as

$$S_n(\theta_n) \equiv \frac{c^2 L_{\text{int}}}{2\pi\lambda_G{}^2}\delta\varphi\left(n^2\sin^2\theta_n \Big/ \left(\frac{1}{\beta} - \cos\theta_n\right)^3\right)\left(R_n R_n^*\right), \tag{A2.11}$$

in terms of which (A2.9) becomes

$$W_{\text{collected, total}} = \sum_{\text{radiating orders } n} \int_0^{\pi} d\theta_n \exp\left(-2g_0(y_o - y_{\max})\right) S_n(\theta_n). \tag{A2.12}$$

This is a form suitable for generalizing to the case of emission from an electron beam.

A2.3 Collecting emission from an electron beam

Simplifying assumptions must immediately be made in describing the emission from a real electron beam. I neglect the fact that the emission spectrum from a grating of finite extent is different from that of an infinite grating, and likewise neglect the fact that emission from a grating of finite conductivity differs from that of a perfectly conducting grating* . Moreover, it would be very difficult to specifically account in the theory of van den Berg for electron motion not parallel to the z-axis. Since the electron beam used in

*This consideration is not important to the work of this thesis. However, any attempt to produce or exploit UV or x-ray Smith-Purcell emission would have to account for finite conductivity.

these experiments is well-collimated (the RMS divergence angle is of order 10 mrad), I thus neglect the effects of non-parallel propagation on the emission *spectrum* $S_n(\theta_n)$. The effect on total emitted *energy* of the non-parallel propagation is accounted for, however, in that the total emission energy is taken to be proportional to the average value of the exponential factor over the electron's trajectory:

$$W_{\text{collected, total}} = \sum_{\text{radiating orders } n} \int_0^{\pi} d\theta_n \left\langle \exp\left(-2g_0(y_o(z) - y_{\max})\right) \right\rangle_{\text{avg over z}} S_n(\theta_n) \qquad \text{(A2.13)}$$

Let me now sum over an ensemble of N electrons in a beam. The index k is used to denote the kth electron. Also, $y_k(z)$ is used to denote the height of the kth electron above the grating at position z along its trajectory (*i.e.*, the "o" subscript is dropped):

$$W_{\text{collected, beam}} = \sum_{k=1}^{N} \sum_{\text{radiating orders } n} \int_0^{\pi} d\theta_n \left\langle \exp\left(-2g_0(y_k(z) - y_{\max})\right) \right\rangle_{\text{avg over z}} S_n(\theta_n) \qquad \text{(A2.14)}$$

This can be further simplified by exchanging the order of the sum over k with the integration; likewise, the summation can be performed prior to the z-averaging: this yields

$$W_{\text{collected, beam}} = \sum_{\text{radiating orders } n} \int_0^{\pi} d\theta_n \left\langle \sum_{k=1}^{N} \exp\left(-2g_0(y_k(z) - y_{\max})\right) \right\rangle_{\text{avg over z}} S_n(\theta_n) \qquad \text{(A2.15)}$$

The sum inside the brackets is just the ensemble average over the beam, at a point z, of the exponential attenuation factor. N being large (~10^{10}), this average can be computed in terms of a distribution function $\rho(x, y, z)$. This function describes the distribution, at a point (x, z) on the grating, of the heights above the grating of the various electrons in the electron pulse, regardless of the time at which they arrive at z. Note that not all N electrons propagate over the entire grating: some hit the grating and are lost to the interaction. The distribution's normalization is thus expressed in terms of the number of electrons which reach a given z, which I define as N_z:

$$N_z = \int_{-\infty}^{\infty} dx \cdot \int_{-\infty}^{\infty} dy\, \rho(x,y,z) \tag{A2.16}$$

The distribution $\rho(x,y,z)$ is related to the function describing the time-dependent number density of electrons, $n(x,y,z,t)$, by

$$\rho(x,y,z) = \int_{-\infty}^{\infty} dt\, n(x,y,z,t) \tag{A2.17}$$

The distribution $\rho(x,y,z)$ is what was measured by the beam-viewing system described in Sec. 5.6.4 (unfortunately, only at a single value of z). In any case, the sum term of (6.33) can be replaced by

$$\sum_{k=1}^{N} \exp\left(-2g_0(y_k(z) - y_{\max})\right) \xrightarrow[\text{large } N]{} \int_{y_{\max}}^{\infty} dy \cdot \rho(x,y,z) \cdot \exp\left(-2g_0(y - y_{\max})\right) \tag{A2.18}$$

The averaging operation denoted by brackets in eqn. (A2.15) can then be carried out as an integral in x and z, over the length L_{int} and width W, respectively, of the grating. At this point, I introduce the acceptance function $\chi(x,z;\theta_n,\theta_c)$ to incorporate the effects of the collection mirror-OAPM-lightpipe system. The acceptance function weighs a given point (x,z) on the grating according to the fraction of radiation power emitted at angle θ_n from (x,z) that gets through the collection system, set at nominal acceptance angle θ_c. Thus, the average described by the bracket term in eqn. (A2.15), including the effects of the collection system, can be written as

$$\left\langle \sum_{k=1}^{N} \exp\left(-2g_0\left(y_k(z)-y_{\max}\right)\right)\right\rangle \xrightarrow[\text{large } N\text{; collection system response}]{}$$

$$\frac{1}{L_{\text{int}}W}\int_{\text{grating width}} dx \cdot \int_{\text{grating length}} dz \cdot \chi(x,z,\theta_n;\theta_c)\cdot \int_{y_{\max}}^{\infty} dy \cdot \rho(x,y,z)\cdot \exp\left(-2g_0\left(y-y_{\max}\right)\right)$$

$$\equiv C(\theta_n,\theta_c)$$

(A2.19)

Here, I call $C(\theta_n,\theta_c)$ the collection system response function at emission angle θ_n, with the nominal acceptance angle of the collection system set at θ_c. This is the response function described in Sec. 5.2.3. Finally it is possible to write down the equation describing emission issuing forth from the lightpipe with the collection system set to view emission at the nominal angle θ_c, produced from a finite beam:

$$W_{\text{collected, beam}}(\theta_c) = \sum_{\text{radiating orders } n} \int_0^{\pi} d\theta_n C(\theta_n,\theta_c) S_n(\theta_n) \qquad \text{(A2.20)}$$

At this point, I should review and emphasize the simplifying assumptions made in formulating this result. As stated earlier, I have neglected the effects of finite grating extent and finite grating conductivity, as well as perturbations to the spectral distribution caused by electrons' trajectories not being precisely parallel to the z-axis. There is yet another effect not accounted for in (A2.20). As shown by eqn. (5.5), the emission pulses are of finite duration: their frequency spectra will therefore be broadened in comparison to those of infinite duration. Unfortunately, the resolution attained in the spectral measurements of this work is inadequate to identify either this or the previously mentioned effects. Thus, eqn. (A2.20) is adequate for comparing the theory to the experimental data. To do so, however, requires at least some knowledge of the electron density distribution $\rho(x,y,z)$ and the acceptance function $\chi(x,z;\theta_n,\theta_c)$. The discussion of the collection

system model in Sec. 5.2.3 elucidates its limitations, and therefore our knowledge of χ; I will discuss below how one can estimate the values of $\rho(x,y,z)$ over the grating surface, using the limited information available.

A2.4 Estimating the density function

The beam density function $\int_{-\infty}^{\infty} dx \cdot \rho(x,y,z)$ was measured at two values of z in the experiments of this work. Using this information, one can employ a free particle phase space distribution function to estimate the values of the density function elsewhere. In the case where no external forces are imposed, and mutual Coulombic repulsion forces can be neglected, it can be easily shown that the distribution function in y and the normalized momentum* y', $f(y(z),y'(z),z)$, must satisfy the equation

$$\left(\frac{\partial}{\partial z} + y'\frac{\partial}{\partial y}\right) f(y(z),y'(z),z) = 0. \qquad \text{(A2.21)}$$

Here, the ($'$) denotes a derivative with respect to z. Equation (A2.21), along with specification of the initial condition determines f: assuming a Gaussian initial distribution in y and y', f can be easily found. Note that no effort was made to model the $(x(z),x'(z))$ distribution.

Figure A2-1 illustrates the distribution model's geometry and defines its parameters. It is easy to include a requirement that the distribution vanish for positions below the grating surface at $y = y_{max}$, thus including the effects of electron interception by the grating. The solution, given in terms of the parameters in Fig. A2-1, is (to a normalization factor to be given below)

* The normalized momentum distribution is the y-momentum distribution, normalized to the momentum z-component; it is equivalent to the distribution of electron trajectory divergence angles, with respect to the beam propagation direction axis.

$$f(y,y',z) = (\text{const}) \cdot \exp\left(\frac{-((y-y_b)-y'z)^2}{2\sigma_y{}^2} \right) \exp\left(\frac{-(y'-\alpha)^2}{2\sigma_{y'}{}^2} \right), \; y'(z-z_G) < (y-y_{\max})$$
$$= 0, \; y'(z-z_G) \geq (y-y_{\max}) \text{ or } y \leq y_{\max} \tag{A2.22}$$

The desired density function can be obtained by integrating out the y' dependence. Before stating the result, I define functions in terms of which the result can be conveniently given:

$$\varphi(y,z) \equiv \int_{-\infty}^{\infty} dx \cdot \rho(x,y,z) = \int_{-\infty}^{\infty} dy' \cdot f(y,y',z) \tag{A2.23}$$

It can be shown that φ can be written as the product of two functions: the first is the density function for free particles in the absence of any electron interception by the grating (the "free-space" density function), and a function which describes the effects of electron loss to the grating: these functions are

$$\varphi_{\text{free}}(y,z) \equiv \frac{N}{\sqrt{2\pi}\left(\sigma_y{}^2 + \sigma_{y'}{}^2 z^2\right)^{1/2}} \exp\left(\frac{-(y-y_b-\alpha z)^2}{2\left(\sigma_y{}^2 + \sigma_{y'}{}^2 z^2\right)} \right), \tag{A2.24}$$

where N is as before the total number of electrons in the bunch, and

$$\varphi_{\text{atten}}(y,z) \equiv \text{cnorm}\left(\left(\frac{\sigma_y{}^2 + \sigma_{y'}{}^2 z^2}{\sigma_y{}^2 \sigma_{y'}{}^2} \right)^{1/2} \frac{y-y_{\max}}{z-z_G} - \frac{\left(\frac{\alpha}{\sigma_{y'}{}^2} + \frac{(y-y_b)z}{\sigma_y{}^2} \right)}{\left(\frac{\sigma_y{}^2 + \sigma_{y'}{}^2 z^2}{\sigma_y{}^2 \sigma_{y'}{}^2} \right)^{1/2}} \right)^{*}. \tag{A2.25}$$

* The cnorm function is the "cumulative normalization" function, and is defined as

$$\text{cnorm}(x) = \frac{1}{\sqrt{2\pi}} \int_{-\infty}^{x} dt \cdot \exp\left(\frac{-t^2}{2} \right).$$

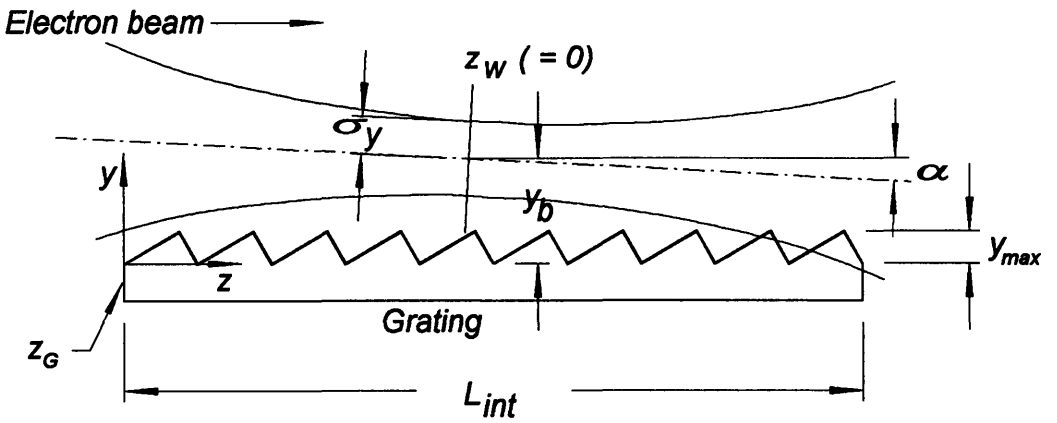

FIGURE A2-1. Distribution function model parameters. Note that the steering angle shown is greatly exaggerated in size. Also, the beam divergence shown is greatly enlarged. The z-position of the grating's upstream end is z_G; the z-position of the beam waist is z_w, defined to be the z-origin. The vertical position of the beam waist is y_b, and the steering angle (i.e., the center of the normalized momentum distribution) is α. The Gaussian beam standard deviation is σ_y, and that of the beam divergence distribution is $\sigma_{y'}$. Finally, the maximum y-extent of the grating surface is y_{max}.

In terms of these functions, φ is defined, for $z > z_G$, as

$$\varphi(y,z) = \varphi_{\text{free}}(y,z) \cdot \varphi_{\text{atten}}(y,z). \tag{A2.26}$$

φ is normalized so that $\int_{-\infty}^{\infty} dy \cdot \varphi(y,z_G) = N$, i.e., that the beam starts out at the beginning of the grating with N particles (likewise, the total number of particles at z, N_z, is $N_z = \int_{-\infty}^{\infty} dy \cdot \varphi(y,z)$).

I have already described the beam profile measurements performed in this work, the grating scan (see Sec. 5.6.3) and the acquisition of the video beam image (Sec. 5.6.4). I can now exactly define the information obtained from these measurements, in terms of

the density functions $\rho(x,y,z)$ and $\varphi(y,z)$ defined above. The video beam image provided a measurement of $\rho(x,y,z_w)$, *i.e.*, the density function at the position of the beam waist: the electron beam was focused on the imaging screen. The grating scans provided the values of $\int_y^\infty dt \cdot \varphi(t, z_G + L_{\text{int}})$, *i.e.*, the integrated density function at the downstream end of the grating (see Sec. 5.6.3).

The video beam image data, $\rho(x,y,z_w)$, could be easily integrated over x (as per eqn. (A2.23): see Fig. A2-2 for an example) to yield $\varphi(y,z_w)$. This measured profile could then be fit with a Gaussian function to provide a measure of the beam waist size σ_y. Unfortunately, the vertical beam position at the waist, y_b (see Fig. A2-1), could not be determined from this fit, because the beam had to be steered down from its normal trajectory in order to hit the phosphor screen.

Finally and at last, I can describe how the grating scan data were used to estimate the standard deviation of the vertical momentum distribution $\sigma_{y'}$, the vertical position of the beam center y_b, and the steering angle α. Knowledge of these parameters enabled me to estimate the shape of the density distribution, and use that estimate to assess its effects on the collection system response function $C(\theta_n, \theta_c)$. A nonlinear fit* of certain of the grating scan charge data was performed, to a fit function of the form

$$Q_{fit}(y) = Q_o \int_y^\infty dt \cdot \varphi(t, z_G + L_{\text{int}}), \tag{A2.27}$$

in which the parameters α, y_b, and $\sigma_{y'}$ were varied simultaneously. Great caution had to be exercised in specifying the initial guess of the parameter values. Values consistent with

* A standard Levenberg-Marquardt algorithm was used [Press *et. al.*, p. 574].

known facts about the electron beam had to be used: the beam emittance (emittance $\varepsilon \equiv \pi\sigma_y\sigma_{y'}$) had been measured on previous occasions by ATF personnel; and the steering angle was known to be of order $\alpha \sim y_b/(1\text{ meter})$. An initial value for y_b could be obtained from a cursory examination of the grating scan data: beam center was close to the grating height at which the charge was reduced by half. Moreover, one afterwards had to critically examine the answers to verify that they did not seriously disagree with these (approximately) known beam properties.

One is entitled to view the results of any nonlinear fit with some skepticism, hence my description of such results as an "estimate". The answer depends heavily on the initial guess. The result also is dependent on the extent to which the model function is appropriate to describe the data. Nevertheless, the answers in this case are far from worthless since in fact the initial guesses are not based on speculation, but rather on previous beam measurements. Moreover, the beam density distributions were typically fit rather well with a Gaussian model. In any case, it is difficult to assign precise uncertainties to the results. I estimate the uncertainty in $\sigma_{y'}$ to be at least of order tens of percent, however. Figure A2-2 displays a typical video-derived density distribution, and its associated grating scan and best-fit curve. The best fit parameter values are entirely reasonable: $\sigma_{y'}$= 10.9 mrad, α = 0.56 mrad, y_b = 2.1 mm (with respect to the nominal surveyed beam axis).

In the earlier days of the experiment (e.g., when the majority of the spectral data were obtained), only the grating scan data were available. In that case, I was reduced to performing a fit of the kind described above, but also had to vary the beam waist size σ_y. This reduces the reliability of the results. Nevertheless, the results are useful to the extent that they are relied upon to the appropriate degree. These results were used only to determine the order of magnitude of variations in the intensity of emission from various

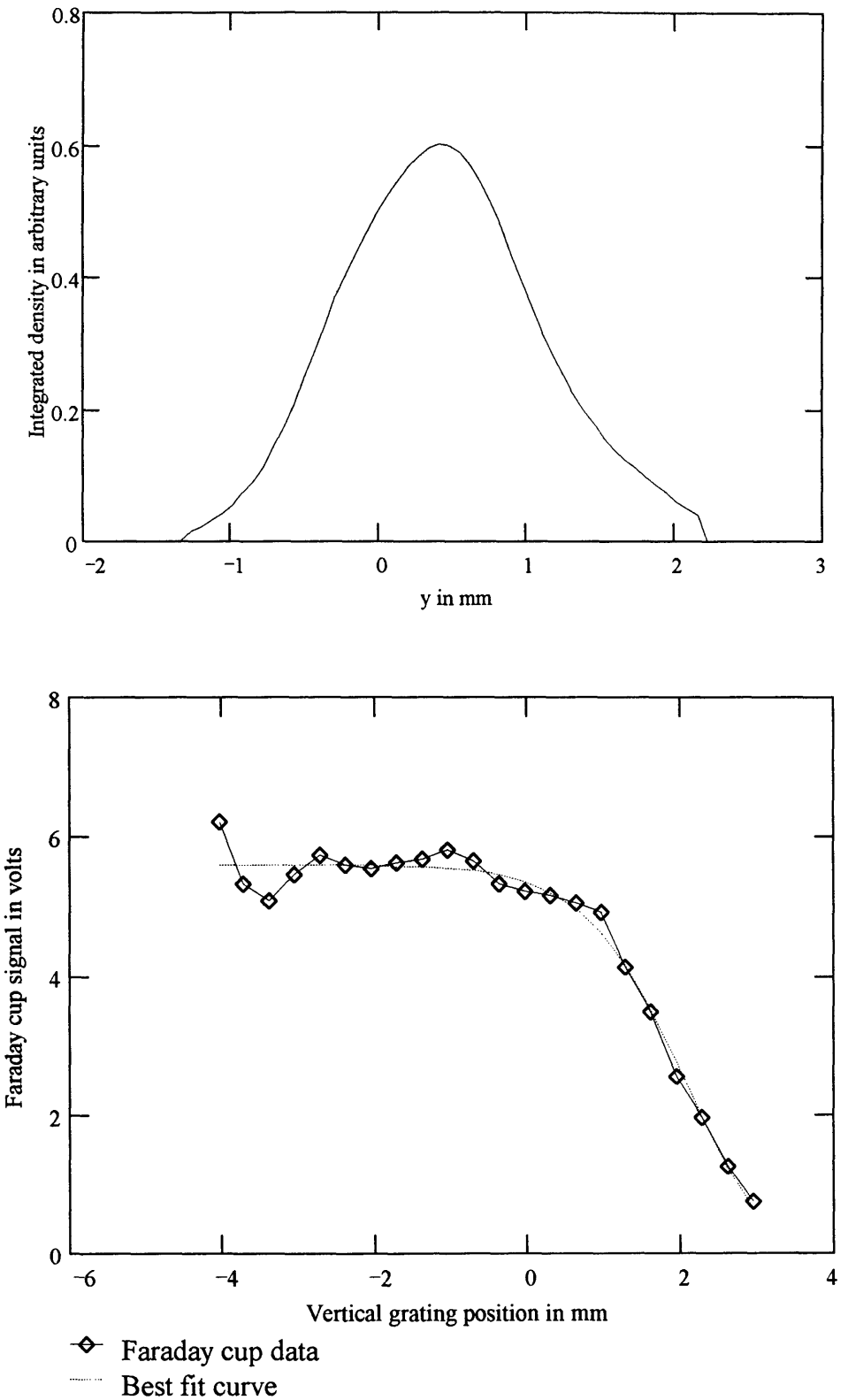

FIGURE A2-2. Measured density profiles. The top curve is the density profile $\varphi(y, z_w)$ extracted from video profile data like that of Fig. 5-13; the bottom curve is grating scan data and its best-fit curve.

points on the grating surface, for the spectroscopy measurements of Sec. 6.3.2. An estimate based on the Gaussian model using best-fit parameters indicated that the emission intensity varied only over a range of about ±2% over the length of the grating. One need not take such variations into account in computing the $C(\theta_n, \theta_c)$ profile.

A2.5 Incorporating the spectrometer

Even having proven that the detected emission is due to the Smith-Purcell effect, attaining spectral measurements with resolution better than that afforded by the collection system response curve $C(\theta_n, \theta_c)$ required use of the spectrometer (see Sec. 5.3). The spectrometer also afforded an easy way to discriminate against spectral orders *lower* than a given order of interest. However, a grating spectrometer will pass all integer multiples of the nominal accepted frequency [Kimmett p. 113], so that even when using the spectrometer, filters were required to remove *higher* Smith-Purcell emission orders.

Application of the spectrometer and an appropriate polyethylene cross-polarized diffraction filter (see Sec. 5.6.1) thus selected out the desired Smith-Purcell order of interest. The spectrum of emission emerging from the spectrometer is the convolution *in wavelength* of the spectrum emerging from the lightpipe with the spectrometer lineshape function (see Sec. 5.3 for a description of the spectrometer). Formally, this can be written as

$$W_{\text{collected, beam}}(\lambda_s, \lambda_c) = \int_0^\infty d\lambda \left(\frac{d\theta_n}{d\lambda} \right) C(\theta_n(\lambda), \theta_c(\lambda_c)) S_n(\theta_n(\lambda)) \cdot \Sigma(\lambda_s - \lambda), \quad \text{(A2.28)}$$

where the change of variables from emission angle to wavelength is explicitly shown, as is the selection of the desired order n to be viewed; $\Sigma(\lambda)$ is the spectrometer lineshape function. The Smith-Purcell wavelength relation (A1.16) determines $d\theta_n/d\lambda$, $\theta_n(\lambda)$ and $\theta_c(\lambda_c)$ as functions of wavelength. To complete the change of variables, I define

$$C_n(\lambda,\lambda_c) \equiv C\left(\theta_n(\lambda),\theta_c(\lambda_c)\right)$$
$$S_{n,\lambda}(\lambda) \equiv S_n\left(\theta_n(\lambda)\right)\cdot\frac{d\theta_n}{d\lambda} \quad ; \tag{A2.29}$$

the wavelength spectral distribution can be written

$$S_{n,\lambda}(\lambda) = \frac{L_{\text{int}}\cdot\delta\varphi\cdot c^2}{2\pi}\frac{\sqrt{1-\left(\frac{1}{\beta}-\frac{n\lambda}{\lambda_G}\right)^2}}{\lambda^3}\left(R_n R_n^*\right). \tag{A2.30}$$

In these terms, the emitted energy passed by the spectrometer can be written

$$W_{\text{collected, beam}}(\lambda_s,\lambda_c) = \int_0^\infty d\lambda\cdot S_{n,\lambda}(\lambda)C_n(\lambda,\lambda_c)\cdot\Sigma(\lambda_s-\lambda). \tag{A2.31}$$

In the spectral studies of Sec. 6.3, the range of wavelengths over which measurements were made was restricted adequately so that neither the shape nor the amplitude of the collection system response function varied significantly over the range of collection system settings λ_c used. This fact permits me to write the collection system response function in the form

$$C_n(\lambda,\lambda_c) \cong C_n(\lambda-\lambda_c), \tag{A2.32}$$

yielding the final form for the measured emission energy as a function of the spectrometer setting λ_s and the collection system setting λ_c:

$$W_{\text{collected, beam}}(\lambda_s,\lambda_c) \cong \int_0^\infty d\lambda\cdot S_{n,\lambda}(\lambda)\cdot C_n(\lambda-\lambda_c)\cdot\Sigma(\lambda_s-\lambda) \tag{A2.33}$$

This equation permits the comparison of the data of Sec. 6.3 to the van den Berg theory. Key to that comparison is the fact that the measured signal is approximately a double convolution of the spectrum with the collection system response function and the

spectrometer lineshape. One can therefore remove the effects of one or the other instrument function, by integrating (A2.33) over either λ_s or λ_c. Thus, acquiring a two-dimensional matrix of data over a range in λ_s and λ_c adequate to "cover" the spectral peak feature will yield two profiles: the convolution of the spectral line with the spectrometer lineshape, and the convolution of the spectral line with the collection system response curve. This is the approach used in the measurements of Sec. 6.3.

BIBLIOGRAPHY

[Bachheimer, 1972] J.-P. Bachheimer, *Phys. Rev. B* **6**, 2985 (1972)

[Bachheimer and Bret, 1968] J.-P. Bachheimer and J.-L. Bret, *C. R. Acad. Sci. Paris* **266**, 902 (1968)

[Batchelor *et. al*, 1988] K. Batchelor *et. al.*, *Proc. 1988 LINAC Conf.*, Williamsburg, VA

[Baym] Baym, G., *Lectures on quantum mechanics,* Benjamin-Cummings Publishing Co., 1969

[Ben-Zvi *et. al.*, 1992] I. Ben-Zvi *et. al.*, *Nucl. Inst. Meth.* **A318**, 781 (1992)

[Ben-Zvi *et. al.*, 1992 (ii)] I. Ben-Zvi *et. al.*, *Nucl. Inst. Meth.* **A318**, 201 (1992)

[Benson and Madey, 1989] S.V. Benson and J.M.J. Madey, *Phys. Rev. A* **39**, 1579 (1989)

[Bertoletti] M. Bertoletti, *Masers and lasers: an historical approach*, A.Hilger (1983)

[Billardon *et. al.*, 1983] M. Billardon *et. al.*, *Phys. Rev. Let.* **51**, 1652 (1983)

[Blastos, 1994] J.C. Blastos, M.S. thesis, Mass. Inst. of Tech. (1994)

[Bobbs *et. al.*, 1990] B.L. Bobbs *et. al.*, *Nucl. Inst. Meth.* **A296**, 574 (1990)

[Bohr, 1913] N. Bohr, *Phil. Mag.* **26**, 1 (1913)

[Bonifacio *et. al.*, 1990] R. Bonifacio *et. al.*, *Rivista del Nuovo Cimento* **13**, 1 (1990)

[Booske *et. al.*, 1988] J.H. Booske *et. al.*, *J. Appl. Phys.* **64**, 6 (1988)

[Brau] C. Brau, *Free electron lasers*, Academic Press (1990)

[Braun] M. Braun, *Differential equations and their applications (4th ed.)*, Springer-Verlag (1993)

[Burdette and Hughes, 1976] E.L. Burdette and G. Hughes, *Phys. Rev. A* **14**, 1766 (1976)

[Couprie *et. al.*, 1993] M.E. Couprie *et. al.*, *Europhys. Let.* **21**, 909 (1993)

[Cover *et. al.*, 1990] R.A. Cover *et. al.*, *Nucl. Inst. Meth.* **A296**, 603 (1990)

[Deacon *et. al.*, 1977] D.A.G. Deacon *et. al.*, *Phys. Rev. Let.* **38**, 892 (1977)

[Destler *et. al.*, 1986] W.W. Destler *et. al.*, *J. Appl. Phys.* **60**, 521 (1986)

[Dodd *et. al.*, 1992] J.W. Dodd *et. al.*, *Nucl. Inst. Meth.* **A318**, 178 (1992)

[Doucas *et. al.*, 1992] G. Doucas *et. al.*, *Phys. Rev. Let.* **69**, 1761 (1992)

[Drobyazko *et. al.*, 1989] I.B. Drobyazko *et. al.*, *Nucl. Inst. Meth.* **A282**, 424 (1989)

[Edighoffer *et. al.*, 1984] J.A. Edighoffer *et. al.*, *Phys. Rev. Let.* **52**, 344 (1984)

[Feynman] R.P. Feynman, *Lectures on Physics*, Addison-Wesley, 1965

[Friedman *et. al.*, 1988] A. Friedman *et. al.*, *Rev. Mod. Phys.* **60**, 471 (1988)

[Gordon *et. al.*, 1954] Gordon *et. al. Phys. Rev.* **95,** 282 (1954)

[Gover and Livni, 1978] A. Gover and Z. Livni, *Opt. Commun.* **26**, 375 (1978)

[Gover *et. al.*, 1984] A. Gover *et. al.*, *J. Opt. Soc. Am. B* **1,** 723 (1984)

[Haeberle *et. al.*, 1994] O. Haeberle *et. al.*, *Phys. Rev.* **E** 49, 3340 (1994)

[Hama *et. al.*, 1994] H. Hama *et. al.*, *Nucl. Inst. Meth.* **A341**, 12 (1994)

[Hertz, 1889] H.Hertz, *Annalen der Physik* **36**, 769 (1889)

[Hessel, 1964] A. Hessel, *Can. J. Phys.* **42**, 1195 (1964)

[Huang *et. al.*, 1994] Y. C. Huang *et. al.*, *Nucl. Inst. Meth.* **A341**, 431 (1994)

[Jackson] J.D. Jackson, *Classical Electrodynamics (2nd Ed.)*, John Wiley and Sons (1975)

[Jha and Wurtele, 1993] P. Jha and J. Wurtele, *Nucl. Inst. Meth.* **A331**, 447 (1993)

[Kimel and Elias, 1990] I. Kimel and R. Elias, *Nucl. Inst. Meth.* **A296**, 611 (1990)

[Kimmit] M.F. Kimmitt, *Far Infrared Techniques*, Pion Ltd. (1970)

[Kleppner *et. al.*, 1962] D. Kleppner *et. al.*, *Phys. Rev.* **126**, 603 (1962)

[Kroll and McMullin, 1978] N.M. Kroll and W.A. McMullin, *Phys. Rev. A* **17**, 300 (1978)

[Madey, 1971] John M. J. Madey, *J. Appl. Phys.* **42**, 1906 (1971)

[Marshall] T.C. Marshall, *Free-electron lasers*, MacMillan (1985)

[Maxwell, 1865] J.C. Maxwell, *Phil. Trans.* **155**, 459 (1865)

[Millikan, 1911] R.A. Millikan, *Phys. Rev.* **32**, 349 (1911)

[Motz, 1951] H. Motz, *J. Appl. Phys.* **22**, 527 (1951)

[Motz *et. al.*, 1953] H. Motz *et. al.*, *J. Appl. Phys.* **24**, 826 (1953)

[Nguyen *et. al.*, 1994] D.C. Nguyen *et. al.*, *Nucl. Inst. Meth.* **A341**, 29 (1994)

[Nodvick and Saxon, 1954] J.S. Nodvick and D.S. Saxon, *Phys. Rev.* 96, 180 (1954)

[O'Shea *et. al.*, 1994] P.G. O'Shea *et. al.*, *Nucl. Inst. Meth.* **A341**, 7 (1994)

[Ohigashi *et. al.*, 1994] N. Ohigashi *et. al.*, *Nucl. Inst. Meth.* **A341**, 426 (1994)

[Phillips, 1960] R.M. Phillips, *I.R.E. Trans. Elec. Dev.* 7, 231 (1960)

[Press *et. al.*] Press, W.H. *et. al.*, *Numerical recipes in Pascal*, Cambridge Univ. Press, 1989

[Price, 1991] E. Price, Ph.D. thesis, Dartmouth College (1991)

[Ramian *et. al.*, 1986] R. Ramian *et. al.*, *Nucl. Inst. Meth.* **A250**, 125 (1986)

[Roberson and Sprangle, 1989] C.W. Roberson and R. Sprangle, *Phys. Fluids B* **1**, 3 (1989)

[Rutherford, 1911] E. Rutherford, *Phil.Mag.* **21**, 669 (1911)

[Schafer *et. al.*, 1981] R.W. Schaefer *et. al.*, *Proc. IEEE* **69**, 432 (1981)

[Shih *et. al.*, 1990] I. Shih *et. al.*, *J. Opt. Soc. Am. B* **7**, 351 (1990)

[Sisson, 1994] D. Sisson, B.S. thesis, Mass. Inst. of Tech. (1994)

[Slater *et. al.*, 1986] J. Slater *et. al.*, *Nucl. Inst. Meth.* **A250**, 228 (1986)

[Smith and Purcell, 1953] S.J. Smith and E.M. Purcell, *Phys. Rev.* **92**, 1069 (1953)

[Stoner *et. al.*, 1990] R. Stoner *et. al.*, *IEEE Trans. Plasma Sci.* **18**, 387 (1990)

[Tecimer and Elias, 1994] M. Tecimer and L.R. Elias, *Nucl. Inst. Meth.* **A341**, ABS 126 (1994)

[Toraldo di Francia, 1960] G. Toraldo di Francia, *Nuovo Cimento* **16**, 61 (1960)

[Tran and Wurtele, 1990] T.M. Tran and J.S. Wurtele, *Phys. Reports* **195**, 1 (1990)

[van den Berg, 1971] P.M. van den Berg, *Appl. Sci. Res.* **24,** 261 (1971)

[van den Berg, 1973] P.M. van den Berg, *J. Opt. Soc. Am.* **63,** 1588 (1973)

[Vetrovec, 1990] J. Vetrovec, *Nucl. Inst. Meth.* **A296**, 563 (1990)

[Wachtel, 1979] J. Wachtel, *J. Appl. Phys.* **50**, 49 (1979)

[Walsh *et. al.*, 1994] J. Walsh *et. al.*, *Nucl. Inst. Meth.* **A341**, 277 (1994)

[Walsh *et. al.*, 1985] J. Walsh *et. al.*, *IEEE J. Quant. Elec.* **QE-21**, 920 (1985)

[Wang *et. al.*, 1992] X.J. Wang *et. al.*, *J. Appl. Phys.* **72**, 888 (1992)

[Warren and Fortgang, 1994] R.W. Warren and C.M. Fortgang, *Nucl. Inst. Meth.* **A341**, 444 (1994)

[Warren *et. al.*, 1990] R.W. Warren *et. al.*, *Nucl. Inst. Meth.* **A296**, 558 (1990)

[Wood, 1935] R.W. Wood, *Phys. Rev.* **48**, 928 (1935)

[Zhang *et. al.*, 1990] R. Zhang *et. al.*, *Nucl. Inst. Meth.* **A341**, 67 (1994)